

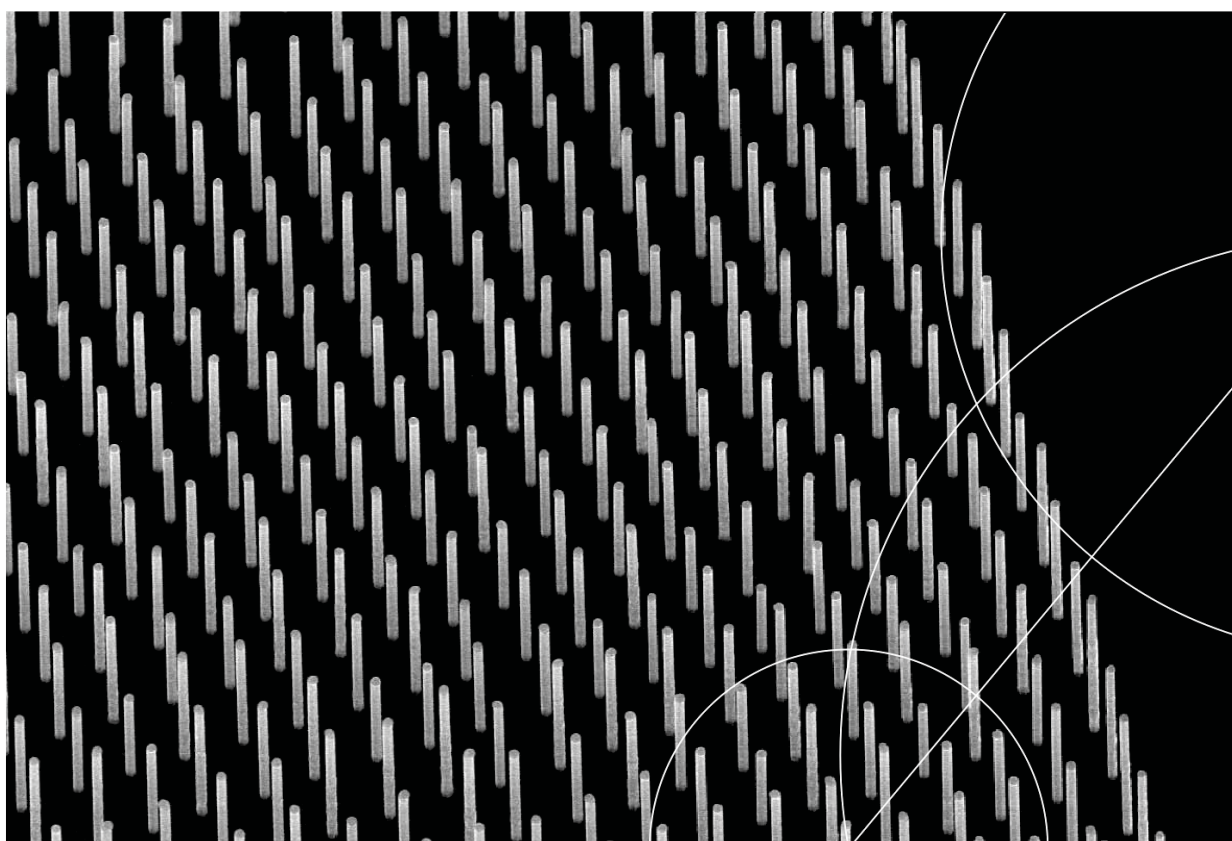


# PhD thesis

Morten Hannibal Madsen

## Indium Arsenide Nanowires

Fabrication, Characterization, and Biological Applications



Academic advisor: Jesper Nygård

Submitted: 15/11/12

# Indium Arsenide Nanowires

## Fabrication, Characterization and Biological Applications

© 2012 Morten Hannibal Madsen

Front cover: SEM image of Au-assisted InAs NWs positioned by electron beam lithography.

Back cover: Collage of a SEM image of Au-assisted InAs NWs positioned by electron beam lithography and a HAADF STEM image of an Au-assisted GaAs NW (image by Erik Johnson).

Nano-Science Center & Center for Quantum Devices  
Niels Bohr Institute  
Faculty of Science  
University of Copenhagen  
Universitetsparken 5  
2100 Copenhagen E  
Denmark

<http://qdev.nbi.ku.dk>

# Contents

<b>Abstract</b>	<b>vii</b>
<b>Dansk Resume</b>	<b>ix</b>
<b>List of Papers</b>	<b>xi</b>
<b>Abbreviations</b>	<b>xiii</b>
<b>1 Introduction</b>	<b>1</b>
1.1 Nanotechnology . . . . .	1
1.2 Nanowires . . . . .	2
1.3 Microscopy . . . . .	3
1.4 Device Fabrication . . . . .	3
1.5 Biological aspect . . . . .	4
<b>2 Synthesis of Nanowires</b>	<b>7</b>
2.1 Basic Growth Models . . . . .	7
2.1.1 Mass Continuity Growth Model . . . . .	8
2.2 Molecular Beam Epitaxy . . . . .	9
2.2.1 The MBE System Layout . . . . .	9
2.2.2 Degassing of Substrates . . . . .	11
2.2.3 Control of Growth Parameters . . . . .	11
2.2.4 Temperature of the Substrate During Growth . . . . .	12
2.2.5 Other Growth Systems . . . . .	14
2.3 Au-Assisted Nanowires . . . . .	15
2.3.1 Thin Au Film Deposition . . . . .	15
2.3.2 Enhanced Control of Au Droplets . . . . .	16
2.4 Self-Assisted Growth of Nanowires . . . . .	17
2.4.1 Randomly Positioned Self-Assisted NWs . . . . .	17
2.4.2 Selective Area Growths . . . . .	18
2.5 Vertically Aligned Carbon Nanofibers . . . . .	19

2.6	Summary . . . . .	21
<b>3</b>	<b>Characterization</b>	<b>23</b>
3.1	Scanning Electron Microscopy . . . . .	23
3.1.1	SEM of Nanowires . . . . .	24
3.1.2	In-situ Bending Analysis of InAs NWs . . . . .	25
3.2	Transmission Electron Microscopy . . . . .	26
3.2.1	Quantization of Elements . . . . .	28
3.2.2	Scanning Transmission Electron Microscopy . . . . .	29
3.3	Diffraction . . . . .	30
3.3.1	Light Scattering on a Nanowire Array . . . . .	31
3.3.2	Crystal Structure of Nanowires . . . . .	35
3.3.3	Dark Field Imaging . . . . .	37
3.4	Monochromatic X-rays Diffraction . . . . .	39
3.5	Summary . . . . .	41
<b>4</b>	<b>Au-assisted InAs Nanowire Growth</b>	<b>43</b>
4.1	Optimization of Basic Growth Parameters . . . . .	43
4.1.1	Growth Temperature . . . . .	44
4.1.2	Molecular Beam Fluxes . . . . .	45
4.2	Experimental Determination of Diffusion Lengths . . . . .	47
4.2.1	Diffusion Parameters for an Array of Nanowires . . . . .	49
4.2.2	More Diffusion Parameters and Summary . . . . .	50
4.3	Fault Free Nanowires . . . . .	52
4.4	Transport Properties of Au-doped GaAs . . . . .	55
4.4.1	Measurements of Transport Properties . . . . .	57
4.5	Summary . . . . .	59
<b>5</b>	<b>Self-Assisted Nanowire Growth</b>	<b>61</b>
5.1	Influence of the Oxide Layer . . . . .	61
5.1.1	Regrowth of the Oxide Layer . . . . .	63
5.1.2	Etching of the Oxide Layer . . . . .	64
5.1.3	Ga assisted deoxidization . . . . .	64
5.1.4	Selective Area Growth . . . . .	67
5.2	Growth Mechanism . . . . .	68
5.2.1	Crystal Structure Analysis . . . . .	68
5.2.2	Formation of Droplets . . . . .	70
5.2.3	Growth Interruptions . . . . .	72
5.2.4	Homoepitaxial Growth . . . . .	75
5.2.5	Conclusion . . . . .	77
5.3	<i>In-situ</i> Study with X-rays . . . . .	77
5.3.1	Wurtzite Formation In Self-Assisted GaAs Nanowires . . . . .	78
5.3.2	Crystal Structure of Self-assisted InAs Nanostructures . . . . .	80

## CONTENTS

---

5.4	Summary . . . . .	81
<b>6</b>	<b>Biological Experiments</b>	<b>83</b>
6.1	Nanowires for Biological Interface . . . . .	83
6.1.1	Cell Membrane Bending . . . . .	84
6.2	Time-lapse Transfection Experiments . . . . .	86
6.2.1	Experimental Methods . . . . .	86
6.2.2	Macro for Intensity Analysis . . . . .	87
6.2.3	Experimental Results . . . . .	89
6.3	Electrical Addressable Vertical InAs Nanowires . . . . .	91
6.3.1	Growth on GaAs Substrates . . . . .	91
6.3.2	Growth on SOI Substrates . . . . .	93
6.4	Capture of Circulating Tumor Cells . . . . .	95
6.4.1	Fabrication of Microfluidic Devices . . . . .	95
6.4.2	Flow Studies using Cancer Cells . . . . .	97
6.4.3	Outlook . . . . .	98
6.5	Summary . . . . .	99
<b>7</b>	<b>Summary</b>	<b>101</b>
7.1	Outlook . . . . .	102
<b>A</b>	<b>Guide to SU8 microfluidics</b>	<b>105</b>



# Abstract

This thesis is about growth of Au-assisted and self-assisted InAs nanowires (NWs). The wires are synthesized using a solid source molecular beam epitaxy (MBE) system and characterized with several techniques including scanning electron microscopy (SEM), transmission electron microscopy (TEM) and x-ray diffraction. InAs NWs can be used in a broad range of applications, including detectors, high speed electronics and low temperature transport measurements, but in this thesis focus will be put on biological experiments on living cells.

Good control of Au-assisted InAs NW growth has been achieved by a systematic study to optimize the growth conditions; first the Au deposition, then the growth temperature and finally the beam fluxes. For further control of the growth, Au droplets have been positioned with electron beam lithography and large scale arrays with a  $> 99\%$  yield have been made on 2 inch substrates. The crystal structure of the NWs has also been investigated, and a method for obtaining pure wurtzite NWs with a well controlled diameter and length is presented.

For self-assisted growth of InAs NWs a method for enhanced control of the nanowire morphology by pre-treatment of the oxide layer is presented. A series of experiments with formation of a droplet on top of the wires has been carried out and pyramidal shaped structures at the NW top with pure zinc blende crystal structure are observed.

A novel *in-situ* experiment with fabrication of NWs and simultaneous characterization using x-ray diffraction is performed with a MBE system attached to a synchrotron beam line. The evolution in crystal structure is monitored for different growth conditions and can be correlated to post growth analysis in TEM. This type of studies gives much more detailed information on formation of the crystal structure and its dependence on growth parameters.

By fabricating the NWs on silicon-on-insulator substrates we demonstrate electrically addressable NWs that are still standing vertically on the substrate and can potentially be used for intra-cellular recordings. Devices for biological experiments using vertically aligned carbon nanofibers have also been fabricated and some of these experiments are described here. By virtually stabbing the nanostructures into living cells, we report a method for fast delivery of plasmid, which can be observed with fluorescence microscopy. Also, devices for capture of circulating tumor cells (CTCs) have been fabricated. The CTC concentration is extremely low and highly effective devices for capturing the CTCs may improve the treatment of cancer patients.



# Dansk Resume

Denne afhandling behandler dyrkning af guld- og selv-katalyserede InAs nanotråde. Trådene er fremstillet i et molekylær stråle epitaksi (MBE) system og karakteriseret ved hjælp af adskillige teknikker, herunder elektron mikroskopi og røntgen spredning. InAs nanotråde kan benyttes til mange forskellige applikationer, herunder detektorer, ultra hurtig elektronik og lav temperatur transport målinger. I denne afhandling er fokus dog på biologiske målinger på levende celler.

God kontrol over dyrkning af guld-katalyserede nanotråde er opnået gennem et systematisk studie af dyrkningsbetingelserne; først ved guld pådampning, derefter dyrkningstemperatur og materiale strøm. For yderligere kontrol af dyrkningen er guld dråber blevet positioneret med elektron stråle litografi og et udbytte på over 99 % på 2 tommer substrater er opnået. Krystalstrukturen af nanotrådene er også blevet undersøgt, og en metode til at fremstille fuldstændigt defekt frie nanotråde med kontrolleret diameter og længde er beskrevet.

For selv-katalyserede InAs nanotråde er en metode for øget styring af deres morfologi beskrevet, hvor tykkelsen af oxid laget styres præcist inden dyrkning. En række eksperimenter med formation af en dråbe på toppen af nanotrådene har ført til fremstillingen af helt rene zinc blende krystaller.

Et nyt *in situ* eksperiment med fabrikation af nanotråde og samtidig karakterisering med røntgen diffraktion er blevet udført med et MBE system tilkoblet en synkrotron. Udviklingen i nanotrådenes krystalstruktur kan følges for forskellige dyrkningsbetingelser og efterfølgende sammenholdes med elektronmikroskopianalyse.

Med fabrikation af nanotråde på silicium-på-insulator substrater har vi fremstillet individuelle nanotråde med elektrisk kontakt, der potentielt set kan bruges til intra-cellulære målinger. Anordninger til biologiske eksperimenter er også blevet fremstillet med vertikale kulstof-nano-fibre og eksperimenter med disse er beskrevet. Ved bogstavelig talt at stikke nanostrukturerne ind i levende celler, har vi vist en metode til hurtig levering af plasmid. Anordninger til at fange cirkulerende kræft celler (CTC) er også blevet fremstillet. Koncentrationen af CTC er ekstrem lav og meget effektive anordninger til at fange dem kan potentielt hjælpe behandlingen af kræft patienter.



# List of Papers

- I**     *Influence of the Oxide Layer for Growth of Self-Assisted InAs Nanowires on Si(111)*  
**Madsen MH**, Aagesen M, Krogstrup P, Sørensen C and Nygård J, *Nanoscale Research Letters* **6**:516 (2011)  
I wrote the paper. I was responsible for the experiment and data analysis.
- II**     *Experimental Determination of Diffusion Lengths for Growth of InAs Nanowires*  
**Madsen MH**, Krogstrup P, Johnson E, Venkatesan S, Mühlbauer E, Scheu C, Sørensen C and Nygård J, *submitted x:xxx* (2012)  
I wrote the paper. I was responsible for the experiment and data analysis.
- III**    *In-situ X-ray Characterization of Wurtzite Formation in GaAs Nanowires*  
Krogstrup P\* , **Madsen MH\***, Hu W, Kozu M, Nakata Y, Nygård J, Takahashi M and Feidenhans'l R, *Applied Physics Letters* **100**, 093103 (2012). \* Equal contributions  
I participated in the experiment, data analysis and writing the paper.
- IV**     *Classroom Demonstration of the Reciprocal Space*  
**Madsen MH**, Høpfner L, Rasmussen N, Stolborg M, Nygård, Feidenhans'l R and Thomsen JW, *American Journal of Physics*, (in press)  
I wrote the paper. I participated in the design of the experiment and discussion of data.

- V** *In-situ Mechanical Characterization of Wurtzite InAs Nanowires*  
Erdelyi R, **Madsen MH**, Safran G, Hajnal Z, Lukacs IE, Fulop G, Csonka S, Nygård J, and Volk J, *Solid State Communications* **152**, 1829-1833 (2012)  
I fabricated the NWs and took active part in the discussion of data
- VI** *Cell Membrane Conformation at Vertical Nanowire Array Interface Revealed by Fluorescence Imaging*  
Berthing T, Bonde S, Rostgaard KR, **Madsen MH**, Sørensen CB, Nygård J, and Martinez KL, *Nanotechnology* **23**, 415102 (2012)  
I fabricated and characterized the NW arrays.
- VII** *Structural Phase Control in Self-Catalyzed Growth of GaAs Nanowires on Silicon (111)*  
Krogstrup P, Popovitz-Biro R, Johnson E, **Madsen MH**, Nygård J, and Shtrikman H, *Nano Letters* **10** (11), (2010)  
I participated in the discussions regarding the growth model.
- VIII** *Comparison of Gate Geometries for Tunable, Local Barriers in InAs Nanowires*  
Nissen PD, Jespersen TS, Grove-Rasmussen K, Marton A, Upadhyay, S, **Madsen MH**, Csonka S, and Nygård J *Journal of Applied Physics* **112**, 084323 (2012)  
I fabricated and characterized the NWs.

# Abbreviations

2DEG	2-Dimensional Electron Gas
AFM	Atomic Force Microscope
ALD	Atomic Layer Deposition
BEP	Beam Equivalent Pressure
BF	Bright Field
BOE	Buffered Oxide Etch
BSA	Bovine Serum Albumin
CBE	Chemical Beam Epitaxy
CBED	Convergent Beam Electron Diffraction
CCD	Charge-Coupled Device
CNF	Carbon Nanofiber
CTC	Circulating Tumor Cell
DF	Dark Field
DNA	Deoxyribonucleic Acid
e-beam	electron beam
EDX	Energy-Dispersive X-ray Spectroscopy
EpCAM	Epithelial Cell Adhesion Molecule
FEG	Field Emission Gun
FET	Field-Effect Transistor
FIB	Focused Ion Beam
GFP	Green Fluorescent Protein
GR	Growth Rate
HAADF	High-Angle Annular Dark-Field
HF	Hydrofluoric acid
HRTEM	High Resolution Transmission Electron Microscopy
HTD	High Temperature Degassing Station
IPA	Isopropanol
ITO	Indium tin oxide
LED	Light Emitting Diode
MBE	Molecular Beam Epitaxy
MOCVD	Metalorganic Chemical Vapour Deposition
NW	Nanowire

OM	Optical Microscope
ORNL	Oak Ridge National Laboratory
PBS	Phosphate Buffered Saline
PMMA	Poly(methyl methacrylate)
RHEED	Reflection High-Energy Electron Diffraction
RIE	Reactive Ion Etching
ROI	Region of interest
S/N	Signal-to-noise
SAED	Selected Area Electron Diffraction
SEM	Scanning Electron Microscope
SF	Stacking Fault
SOI	Silicon-On-Insulator
STEM	Scanning Transmission Electron Microscope
TEM	Transmission Electron Microscope
UCPH	University of Copenhagen
UHV	Ultra High Vacuum
UV	Ultraviolet
VACNF	Vertically Aligned Carbon Nanofiber
VLS	Vapor-Liquid-Solid
VL	Vapor-Solid
VSS	Vapor-Solid-Solid
WBDF	Weak-Beam Dark field
WZ	Wurtzite
YFP	Yellow Fluorescent Protein
ZB	Zinc Blende

# Acknowledgement

First, I would like to thank all collaborators who I have worked with during this project; without your help and invaluable work I would not have been able to complete my thesis in due time. The last three years have been extremely interesting and I have really enjoyed being part of research groups working at the frontier of new science. It is fascinating to look back at when I began my PhD and see how much the field of nanowire growth and the fundamental understanding has evolved in these years.

Jesper, my main supervisor for this project, thank you very much for hiring me in first place despite of my complete lack of knowledge on nanowires and nanotechnology in general. Your support and open mindset have been appreciated throughout the whole project, especially the freedom to get involved in projects only slightly related to my main project. No matter how busy you have been, you have never put your PhD students under undue stress.

Erik, for teaching me in the art of electron microscopy, proof-reading countless number of pages and always taken your time to explain new stuff to me. You have been as an extra supervisor and will truly be missed when you retire.

Claus, thanks for always being willing to help and for great assistance with the MBE system. Sometimes it seems like you know everything about both technical and practical stuff, your knowledge has saved me a lot of time more than once! It is remarkable you never get upset, even though a clumsy PhD student drops the sample holder in the growth chamber one month after it has been restarted after maintenance.

Peter, it has been a great pleasure and extremely inspiring to work together with you. The incredible knowledge of fundamental nanowire growth you have acquired in the last few years are amazing, and more or less all my theoretical understanding of nanowire growth comes from you. Your contributions to my work have been invaluable and are highly appreciated.

Robert, for arranging the trips to Japan for *in-situ* characterization of nanowires. In a company with two students with only little experimental experience in x-ray diffraction you had to take serious action yourself. Your own students do not believe us when we tell them you still master the instrumentation yourself.

The technical staff, and especially Nader and Inger, for taking care of the cleanroom

and TEM, respectively. It really speeds up the process of fabrication or analysis when you know someone is taking good care of the equipment.

The CLIPS group, and especially Pawel, Trine, Sara, Katrine, and Karen, it is been great to work with you and being part of the project with integrating NWs with living cells. I know how hard you have worked on fabricating useable devices out of simple arrays with NWs. It has been instructive to collaborate with someone with a different background. I have learned a lot biology and biochemistry and I hope you have learned some physics as well. I will also like to acknowledge Anders from the small biotech company InXell, whom I have spent countless hours with for fabrication of NW devices. I hope we one day will see one of our devices in use.

Tim, you are a really inspiring person to work together with and I have never met someone with such a big diversity and knowledge in fields from biology to physics and technical know-how. Every time one of our projects came to a dead end, you immediately had a solution to overcome this and keep the project running. I really enjoyed the six months in your lab and hope we can continue the collaboration. Mitch and Cathy, without your help my trip to ORNL would not have been possible. Let me also thank Dale, Ivan and the rest of the staff at CNMS for great assistance in the cleanroom.

Martin, Jeppe, and Henrik from the small company Sunflake. I have gained a lot of knowledge from our many discussions and often also assistance with the MBE system. A special thanks to Martin for encouraeing the work of self-assisted InAs NW growth, it was of great importance for me and speeded up the process of publishing my first paper.

I would also like to acknowledge the rest of the young and dynamic group I have been a member of during my PhD. Both those of you who I have worked with for specific projects (actually almost everyone!) and those of you who I have shared office with or just hanging around with. You have all participated in making it three great years, and it is fantastic to know, that no matter who is on work that day, you can always ask someone for help.

All the external partners that have spent tremendous amount of time measuring on nanowires. A special thank to Tina, Sriram and Erika for TEM analysis of NWs, Masamitu and Wen for amazing x-ray diffraction experiments, and Janos for coordinating the project with *in-situ* bending of NWs. I hope the projects will continue for a long time.

And finally, I would like to thank Maria for continuous support, inspiration, and love. I still deeply appreciate that you came all the way to Tennessee for several months so we could stay together.

Morten Hannibal Madsen  
November, 2012

# Introduction

The work in this thesis covers a wide field, from fundamental understanding of the growth process of nanowires (NWs) to fluorescence measurements on mammalian cells. A lot of the projects have been performed in collaboration with other groups all around the world. The use of equipment at other laboratories have helped to greatly improve the understanding of nanowire growth and fabrication of devices with nanowires.

The first chapter here introduces some of the topics, which will be treated in details in the later chapters.

## 1.1 Nanotechnology

Nanotechnology is just another name for research conducted at small length scales, and is independent of research area, e.g. physics, chemistry, and biochemistry. A popular definition is that at least one length scale in the system should be less than 100 nanometer (nm). In other words, if we have a box, then one side should at maximum be 100 nm, whereas the two other sides can be infinite. An overview of some length scales are shown in Fig. 1.1, and NWs are seen to have a diameter of around 100 nm and a length of several micrometer ( $\mu\text{m}$ ), putting them into the category of nanotechnology.

Products using nanotechnology are already widely distributed on the consumer market, giving us everything from stronger materials with carbon nanotubes to better insulation using nanopores. In the work presented in this thesis, we work towards integrating nanoscale physical objects with mammalian cells for better and faster drug development. With NWs being 100 times smaller than a typical mammalian cell, we aim to make measurements on individual cells *and* keep them alive for an extended period.

The limit on how small devices we are able to fabricate is pushed all the time. One major achievement was the fabrication of a single sheet of carbon atoms, known as graphene, in 2004[1], for which Andre Geim and Konstantin Novoselov were awarded the Nobel prize in 2010. It does not get thinner than this, but there is still a lot of work to do for scientist to improve the fabrication and find new ways of exploiting the superior properties of graphene.

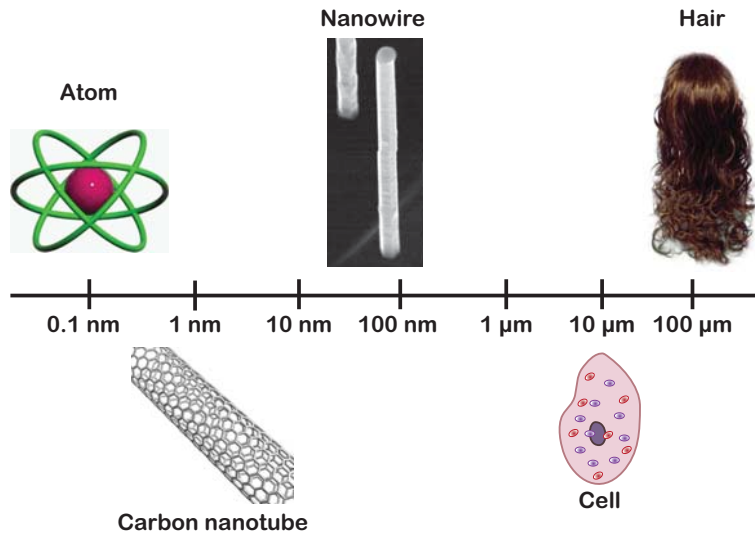


**Figure 1.1:** A nanowire is around 1000 times smaller than a human hair, but still around 1000 times larger than a single atom. Nanowires are significantly smaller than a typical mammalian cell, and we therefore aim at using the nanowires as intracellular probes.

## 1.2 Nanowires

The main focus in this thesis is on NWs, including fabrication, characterization, and device fabrication. Roughly speaking, NWs are elongated crystals with a diameter of 100 nm and a length of several micrometers. They have already found use in a vast amount of applications, e.g. in photonics [2], energy storage [3], bio sensing [4] and high speed electronics[5].

NWs can be synthesized with a lot of different materials, and is often put into groups depending on the main group numbers of the used elements. Some of the most used materials from each group includes: Group IV (Si, Ge), Group III-V (InAs, GaAs, GaN), and group II-VI (CdSe, ZnO). One can even make compounds with multiple elements (e.g. InGaAs) and change materials during growth.

Many methods are used for growth of NWs, where emphasis in this text is put on molecular beam epitaxy (MBE). Other widely used methods include chemical beam epitaxy (CBE) and metalorganic chemical vapour deposition (MOCVD). Especially MOCVD systems are widely used in the production of commercial products, i.e. thin layer deposition to fabricate light emitting diodes (LEDs). Compared to MOCVD, MBE is a slower and more expensive process, but facilitates the synthesis of higher quality devices due to lower incorporation of impurities. So when quality means everything, MBE systems are also used commercially, i.e. transistors for cell phones.

## 1.3 Microscopy

One thing is to fabricate a sample in nanometer size, another is to see it afterwards. In fact, nano-sized features are found all around in nature, without being noticed directly. One example is the feathers of a peacock, where the hue changes depending on the viewing angle. The feathers consist of nano-structures which reflect the incoming light, giving the colorful changes, compared to the normal colors by absorption.

As visible light is electromagnetic waves with a wavelength in the range 390 nm to 780 nm, an object in the nanometer regime is well below the diffraction limit for an optical microscope, and cannot be resolved. Instead scientists use a vast amount of other techniques to resolve small structures, including scanning probes, electrons, and x-rays.

A widely used scanning probe is the atomic force microscope (AFM), where a small tip is dragged (or oscillates just above) the surface one wants to image. Any small feature on the surface will make the oscillation of the tip to change characteristics. After scanning the whole surface one point at a time, a collected image can be obtained. This technique gives very high resolution on surfaces, but as one has to mechanically scan the whole surface it is a rather slow process. It is not suited for vertical NWs, as the force from the tip breaks the NWs in the imaging process.

A more suitable method for imaging vertical NWs is a scanning electron microscope (SEM), where a beam of electrons are shot at the surface, and a detector collects the re-emitted electrons. This is done for each point on the surface, and a computer is used to reconstruct the image. The scanning process is much faster than for an AFM and there is no mechanical contact during measurements.

With more energetic electrons (typically 200 keV), the electrons can pass through a thin sample, and one can get an absorption image, as used in transmission electron microscopy (TEM). Furthermore one can use a TEM for looking at the diffracted electrons, and obtain knowledge of the crystal structure. The limitation on a TEM is much related to the thickness of the specimen. Fortunately NWs have a thickness quite suited for both absorption and diffraction electron microscopy.

A last method to mention is x-ray diffraction. Here an intense beam of monochromatic x-rays are focused on the sample. A very detailed mapping of the crystal structure can be obtained using x-rays. With an MBE chamber attached directly to a synchrotron, we have shown that it is possible to do *in-situ* diffraction on NWs[III].

## 1.4 Device Fabrication

Most of the devices presented here involves one or more processing steps using lithography, either ultraviolet (UV) or electron beam (e-beam). The basic steps of photolithography (UV lithography) are:

1. Spin coat a substrate with a light sensitive resist layer.

2. Design a mask with a specific pattern, align it on top of the substrate and expose it to UV light.
3. Develop the resist. Either the exposed or non-exposed areas vanish, depending on the type of resist used.
4. The open areas can either be etched, or metal can be evaporated into the openings.
5. Last step is to remove the remaining resist with only the pattern left.

A substrate can be processed many times with lithography, and in that way a multiple layered structure can be created. The steps of e-beam lithography are similar, with the difference that instead of designing a permanent mask and expose with UV light, the electron beam from an electron microscope is used for writing one point at a time. E-beam lithography offers the best resolution and is the most flexible, but suffers from being cumbersome and expensive compared to UV lithography.

## 1.5 Biological aspect

Interfacing the NW devices with living cells requires scientist with different background to collaborate. Custom made devices and great skills in handling cells are necessary to achieve success. Great control of cells are achieved using cell culturing, where the cells are grown outside their native environment by detailed control of their conditions. One needs to nurse the cells several times a week to keep them healthy, and experiments have to be planned after the health and growth cyclus of the cells. Important steps in cell culturing include feeding the cells with protein rich media and make sure they do not overpopulate the container they are kept in.

Our preferred method of imaging the surface of NWs, SEM, fails to image living cells, as one needs to coat them with a metallic layer prior to imaging, unless an environmental SEM facility is available. Instead one can use fluorescence microscopy or confocal microscopy, where a fluorescent substance is introduced into the specimen. The basic principle of fluorescence is sketched in Fig. 1.2(a). For instance a green fluorescent protein (GFP), originally retrieved from a jelly fish, is widely used, and as an example, a green fluorescent cat is shown in Fig. 1.2(b). The GFP can be modified so it is not fluorescent until uptaken by living cells (Fig. 1.3(b)). One can also attach the GFP to a DNA string or drug, and use it as an indicator for when it has been uptaken by the cell.

With NWs we hope to improve the uptake and control of drugs and DNA on individual cells. The DNA can be attached to the NW sidewalls, and one can the use the thin NWs to penetrate the cell membrane, giving the DNA direct access to the cell.

Another approach is to use the NWs as electrodes for electrical recordings of the ion channels in the cell membrane, see Fig. 1.3. Ion channels are proteins which control a voltage gradient across the membrane by facilitating the transport of ions. These type of measurements can be performed using the patch-clamp technique, for which Erwin Neher

## 1.5. BIOLOGICAL ASPECT

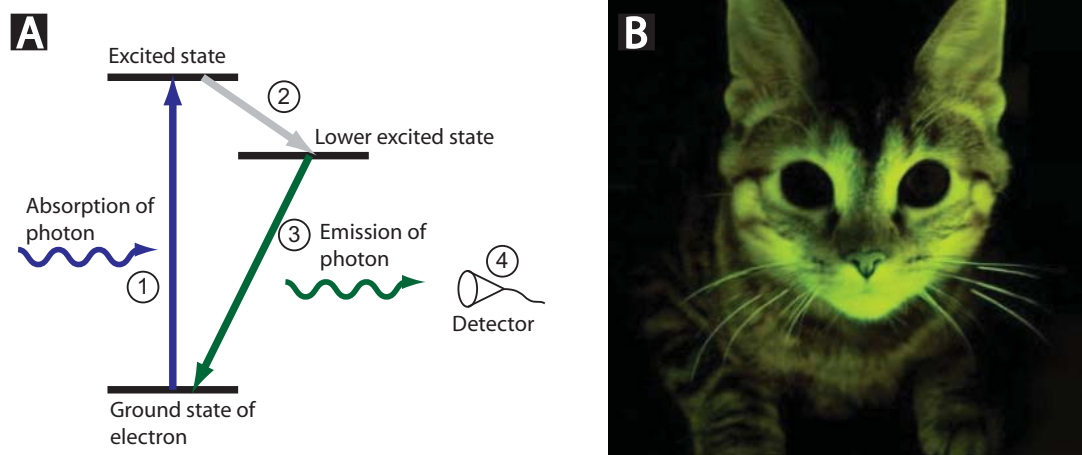


**Figure 1.2:** Fluorescence. (A) Sketch of the principle of fluorescence: 1. A photon is absorbed by an atom by exciting an electron. 2. The electron decays fast to a lower lying excited state. 3. The electron now decays back to the background with emission of a photon. The emitted photon has less energy than the original absorbed one, and a color shift is seen, i.e. blue to green. 4. A detector equipped with a band pass filter only counts the emitted electrons. (B) Green glowing cat from gene encoding. Adapted from [6].

and Bert Sakmann received the Nobel prize in 1991, where a glass micro pipette is used to penetrate the cell membrane. The rupture influences the cells health making measurements possible in only a limited amount of time. With NWs we hope to set up an automatized method for long term measurements.

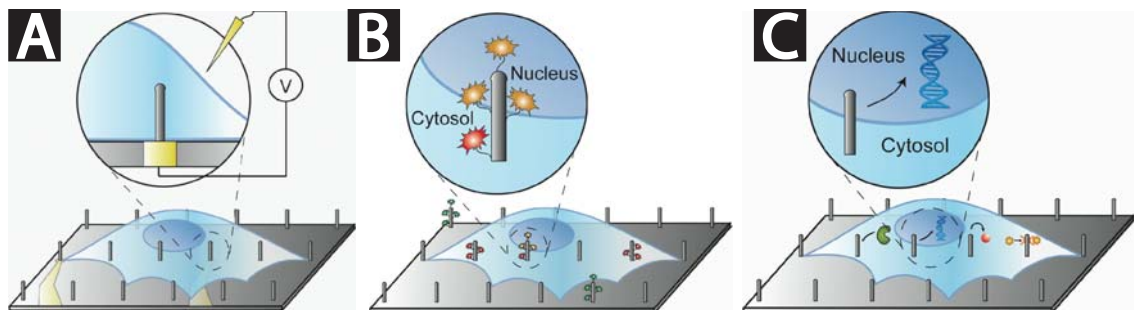


**Figure 1.3:** Possible applications of NWs interfaced with cells. (A) Electrophysiology, where the NWs are used as an intracellular electrode. (B) Fluorescence biosensor. Functionalization of the NWs with fluorophores opens up for spatially resolved analysis within a single cell. (C) Drug delivery, where the small dimensions of NWs are used for direct delivery into the cell nucleus. All figures are adapted from Ref. [7].

We have focused on using InAs NWs for the cell research projects[7, 8][VI], as these are intrinsic conductive and we have good control of the growth process. Other materials have shown to be useable as well, e.g. Si NWs[9, 10, 11] and vertically aligned carbon nanofibers (VACNFs)[12, 13]. Some results using VACNFs have been obtained as well through a collaboration with Oak Ridge National Laboratory (ORNL).



## Synthesis of Nanowires

The synthesis of NWs is of course the first step in fabrication of a NW based device. Many different methods have proven successful for growth of NWs, where MBE and MOCVD are the most used ones for III-V semiconductor NWs. Even though the first NWs were synthesized almost 50 years ago, it is really first in the last decade that research in NWs has accelerated giving an exponential increase in the number of published papers.

### 2.1 Basic Growth Models

The growth mechanism of NWs is still not fully understood even though the first theory was proposed almost 50 years ago[14], where Wagner and Ellis suggested a vapor-liquid-solid (VLS) growth model. In this model, a vapor of atoms is collected in a liquid droplet, and diffuses to the growth interface, where the atoms nucleate, and become a part of the solid crystal. Depending on the growth conditions and method, other growth models have been reported as well, including vapor-solid-solid (VSS) and vapor-solid (VS). An example is growth of Au-assisted GaAs NWs, for which VSS is proposed for CBE grown wires[15], whereas a liquid droplet is found for MBE grown NWs[16]. The basic steps of VLS Au-assisted NW growth is depicted in Fig. 2.1. The droplet remains on top of the NW and thereby elevates the growth interface. Contrary to planar growth, the growth conditions therefore change considerably during growth. Growth models based on a mass continuity approach, where one looks at the contribution from single adatoms, have been used to model experimental data, and will be discussed in the next section.

Newer growth models also describe the crystal structure formation, with the hexagonal wurtzite (WZ) and cubic zinc blende (ZB) as the most important ones for III-V NWs. In 2007, Glas *et al* used classical nucleation theory to propose that nucleation preferentially takes place at the triple phase line[17]. This theory has been refined several times with contributions from around the world[18, 19, 20, 21, 22, 23], and new experimental techniques have helped to improve the understanding of NW growth processes[24, 25][III].

So far, no growth model has been able to fully describe the process of NW growth.

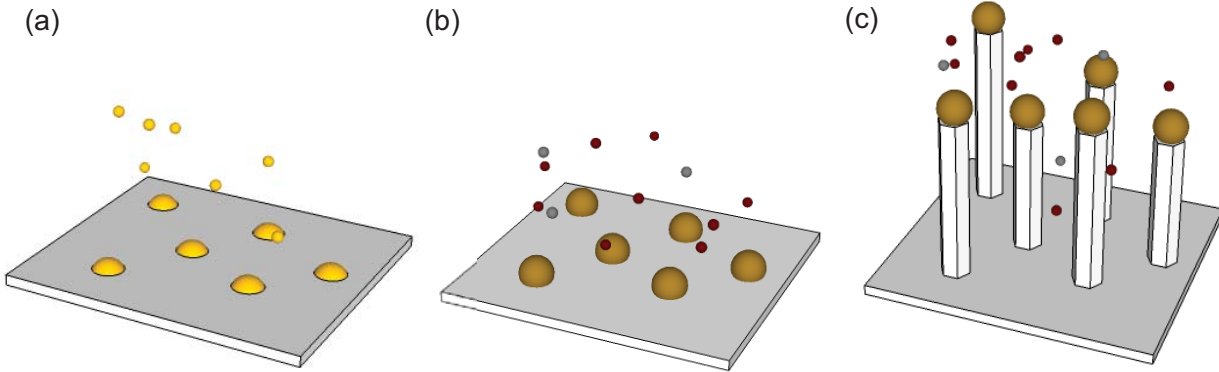


**Figure 2.1:** Basic steps in NW synthesis. (A) Gold is evaporated on the substrate to form droplets. (B) Molecular beams of elements are introduced in the growth chamber to supersaturate the droplet, and the elements begin to nucleate at the substrate/droplet interface. (C) The droplets continue to assist the growth and more layers are formed at the growth interface thereby elevating the droplet.

They can be used to give an indication of how to adjust growth parameters in order to optimize the growth conditions, but it still depends very much on the experimental setup. Improved growth models including dynamic effects can hopefully predict the growth conditions better.

### 2.1.1 Mass Continuity Growth Model

Mass continuity growth models looking at the transport of adatoms have been widely used to model NW growth[26, 27, 28, 29, 30, 31]. We have used a similar approach for modeling of Au-assisted InAs NWs[II] and self-assisted GaAs NWs[VII], as will be described in Sec. 4.2.

Adatoms contributing to the growth can be supplied from three areas: direct impingement on the droplet, diffusion to the growth interface and indirect impingement. Indirect impingement can come from secondary adsorption effects or from a background pressure in the growth chamber. However, it is reasonable to neglect secondary adsorption of group III adatoms under typical growth conditions. The contribution from diffusion comes from both adatoms impinging on the substrate (s) and on the sidewalls (w).

An important parameter in the growth models is the diffusion length of adatoms, i.e. the average effective distance adatoms travel on a surface before they evaporate, nucleate with other adatoms or are being incorporated at the solid surface. For large planar interfaces the diffusion length is a well defined quantity, but during NW growth it is more difficult to define. Instead we will refer to the effective diffusion lengths, which define the collection areas, as shown in Fig. 2.2. Only adatoms on the NW sidewalls with a distance of less than the effective diffusion length to the growth interface can effectively contribute to the growth. However, the effective substrate diffusion length should be interpreted a bit differently in the collection area approach. The adatoms will have to travel first on the substrate and then on the NW sidewalls to reach the growth interface. For a dense array,

the adatoms on the substrate will be shared evenly between the NWs, and this will lower the growth rate. We will return to modeling of MBE NW growth in Chap. 4.

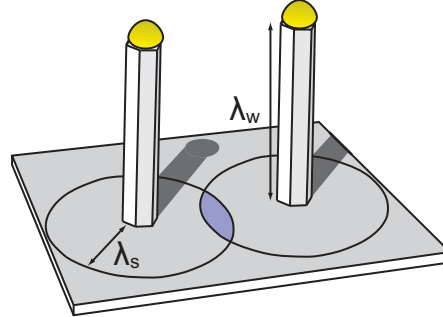


**Figure 2.2:** Sketch of effective diffusion lengths for growth of NWs. The effective collection area on the substrate is indicated by a circle with radius  $\lambda_s$  where the blue area is the overlapping collection area.  $\lambda_w$  is the effective sidewall diffusion length. Adapted from Ref. [II].

## 2.2 Molecular Beam Epitaxy

As the name suggests molecular beam epitaxy is a technique where beams of elements are used for epitaxial crystal growth. The word epitaxy comes from the greek words *epi* and *taxis*, which can be translated to *over* and *order*. In crystal growth it describes the process of forming a crystal layer with a particular orientation, depending on the underlying crystal layer, in other words, growth of an *ordered* layer *over* an existing layer.

The MBE technique was developed by IBM and Bell Labs in the 1960s and 1970s to tailor the production of semiconductors. By combining different materials, known as heteroepitaxy, MBE made it possible to engineer band gaps and obtain new devices with unique properties. Several Nobel Prizes have been awarded based on such devices grown with MBE, including Esaki (1973) for the tunnel diode (or Esaki diode), Laughlin, Störmer and Tsui (1998) for the fractional quantum Hall effect and Alferov and Kroemer (2000) for semiconductor heterostructures.

One of the remarkable achievements of MBE fabricated devices are 2-dimensional electron gases (2DEGs), which have been used to demonstrate the quantum Hall effect[32]. MBE grown 2DEGs have demonstrated electron mobilities of more than  $10^7$  cm<sup>2</sup>/Vs, and is superior to any other fabrication method.

In the following sections an general introduction to MBE growth systems will be given and specific features and procedures for our MBE system are introduced.

### 2.2.1 The MBE System Layout

NWs are grown at the Niels Bohr Institute in a Varian GEN II MBE system equipped with a solid source As source. Knudsen cells with pure materials are used for generating the molecular beams. Beside As as group V material, we have In and Ga as group III

materials, and Be (group II) and Si (group IV) as dopants. The chamber is also equipped with an Au cell for catalyzing the NW growth. The flux rates are controlled by adjusting the base temperature of each cell, except for the As source, which is also equipped with a needle valve. A shutter in front of each cell is used to block the beams when not in use, which will be referred to as the beams being turned off. A cracker on the As source is used to change the species from  $\text{As}_4$  to  $\text{As}_2$  by heating the outlet to  $800\text{ }^\circ\text{C}$ .

A substrate heater with a thermocouple device is used for controlling the temperature, and an external pyrometer is used for calibration. One can measure the beam fluxes using a pressure gauge, and the corresponding growth rates (GRs) with reflection high-energy electron diffraction (RHEED).

The growth chamber is pumped by two 8" cryo-pumps and a 400 L/s ion pump, ensuring that the system keeps ultra high vacuum (UHV). To help maintaining the low pressure, a liquid nitrogen cooled cryo-shield is surrounding the growth chamber and cells. A chamber base pressure in the range  $10^{-11}$  torr was achieved, until we experienced a minor nitrogen leak from the cryo-shield, bringing the pressure to the upper  $10^{-10}$  torr.

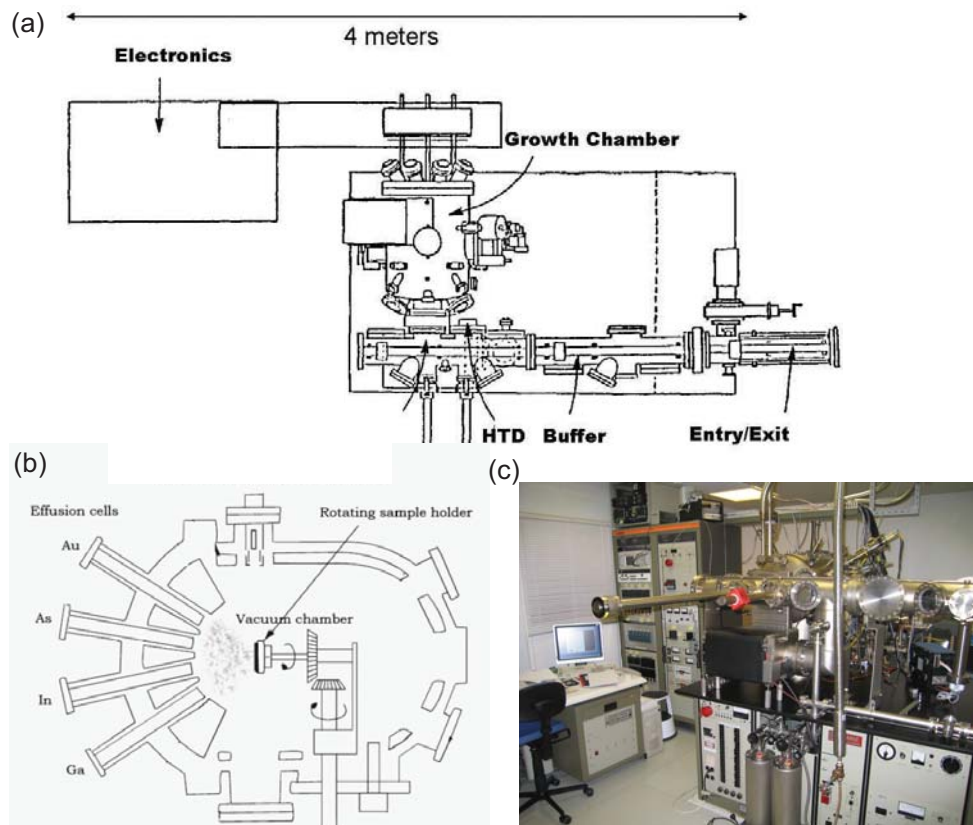


**Figure 2.3:** MBE growth system. (a) Sketch of the MBE system at the Niels Bohr Institute. Substrates are introduced at the Entry/Exit chamber, degassed in the buffer chamber, and then transferred to the growth chamber. (b) Detailed sketch of the growth chamber, with all the effusion cells pointing at the substrate. (c) Picture of the MBE growth system. Adapted from [33].

### 2.2.2 Degassing of Substrates

Contamination is detrimental to the fabrication of high quality devices. It is therefore necessary to take several steps before the substrates are introduced into the growth chamber. Typically the loading and degassing process takes 3 days for a trolley fully loaded with substrates.

All growths are made on epi-ready substrates and loaded directly from the box, as any cleaning attempts seem to do more harm than good. The substrates are clamped on to molybdenum holders, where the backside has been cut out, so the backside of the substrate is exposed. Up to ten substrate holders are now loaded on a trolley and pumped down in the entry/exit chamber. The handling of substrates is performed under class 10 clean room conditions in a laminar flow bench to minimize contamination.

The trolley with substrates is baked for 2 hours at 200 °C, before being introduced to the buffer chamber. Afterwards each substrate is baked individually at a high temperature degassing station (HTD) for 1 hour at a temperature well below significant desorption of the specific substrate, i.e. InAs at 250 °C, GaAs at 400 °C, and Si at 500 °C. A mass spectrometer is attached to the buffer chamber for monitoring of the degassing process.

In the first step of our growth recipe, additional degassing is made inside the growth chamber. By applying an As backing pressure it is possible to degas As-containing samples at much higher temperatures without significant desorption. Typically InAs substrates were degassed for 8 min at 550 °C.

### 2.2.3 Control of Growth Parameters

Beam fluxes can be measured using a pressure gauge inside the growth chamber. It can be positioned at the location of the substrate is during growth. The measured pressure depends very much on the given system, and a more precise method is to measure the bulk equivalent growth rate by using RHEED oscillations. To measure the, say, GaAs GR, a GaAs(100) substrate is loaded, and the substrate is heated to 580 °C with an As<sub>2</sub> backing pressure. A clear diffraction pattern is found by rotating the substrate and adjusting the electron beam and with a photomultiplier the intensity of a single diffraction spot is monitored. The Ga shutter is now opened, and the intensity of the diffraction spot begins to oscillate, with a maximum each time a full monolayer has been grown. One can now find the GR by looking at the time between maxima, and eventually correlate with the atomic layer spacing for the given material. GR measurements of InAs are shown in Fig. 2.4 where a fit of the type  $GR = \alpha \exp(\beta/T)$  have been added, where  $\alpha$  and  $\beta$  are fitting constants.

The substrate temperature is controlled by a heater about 10 mm behind the substrate while a thermocouple device that is located in the center of the heater gives feedback to the power supply. The temperature can also be measured using a pyrometer (IRCON) through one of the windows into the growth chamber. The substrate temperature is a very critical parameter for NW growth, and a 10 °C difference can be enough to go from success to failure. Unfortunately, a lot of parameters affect the measured temperature, including the type of sample holder, the type of substrates and how they are polished[34]. We

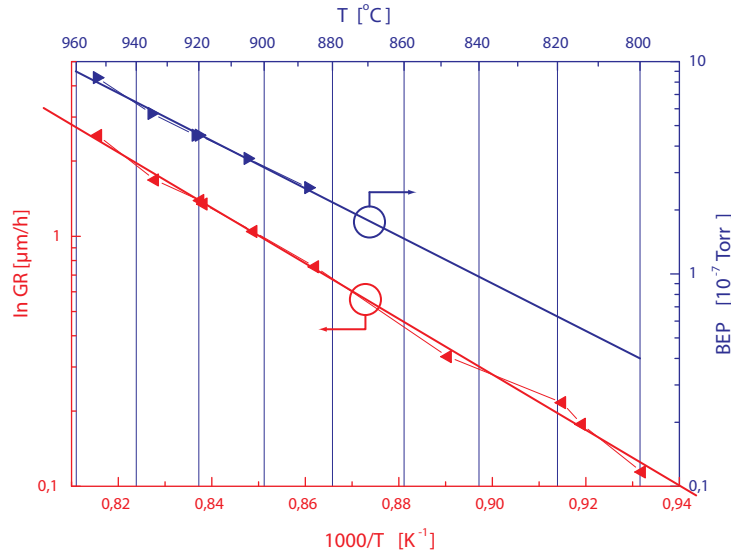


**Figure 2.4:** Growth rate calibration for InAs. The  $x$ -axis refers to the temperature of the effusion cell. Data obtained by Claus B. Sørensen and SunFlake.

have three different types of substrate holders, and at elevated temperatures the difference between them is up to  $40^{\circ}\text{C}$ . The backside polishing of the substrates influences both the radiation absorption and the reading by the thermocouple device[35]. A non-polished rough backside will give rise to increased internal scattering in the substrate, and thereby a higher effective absorption. A blank polished backside of the substrate lets more radiation pass directly through the substrate, especially at higher temperatures, and this will influence the pyrometer reading. We have not found a systematic way of adapting the growth temperature from one type of substrate to another. Instead we made a few test growth when we had to use new substrates.

A last thing to mention is that we made the pyrometer readings before opening the shutters, except when As backing pressure was needed, to avoid reflection from hot effusion cells. At certain angles such reflection could give an increase in the pyrometer reading of up to  $50^{\circ}\text{C}$ .

## 2.2.4 Temperature of the Substrate During Growth

During the experiments with Ga-assisted deoxidization which will be described in Sec. 5.1.3, we observed a temperature gradient across the substrate. This was in first place confirmed by manually scanning around the substrate and making localized measurements using a pyrometer, where a temperature increase was observed closer to the edge. However, the pyrometer measures on a rather large area (circular shaped with a diameter of around 2 cm) not much smaller than a 2 inch substrate and thus a precise value cannot be obtained. Instead we have modeled the temperature using the finite-element analysis program COMSOL Multiphysics. Some of the simulations from this section have been published in

Ref. I.

A three dimensional model of the substrate and sample holder was designed and physical properties from the basic 'heat transfer' package in COMSOL Multiphysics was added to all surfaces and volumes. Heat transfer in solids was added for all components based on the intrinsic material properties and radiation emission was added to the front side of the substrate and holder. A constant heat source was applied to the backside of the model, with the assumption that all energy is absorbed by the sample holder and only 2/3 by the substrate. This assumption is justified by the finite thickness ( $500\ \mu\text{m}$ ) of the substrate and a polished backside. A rough backside of the substrate would lead to increased internal scattering and thereby a higher absorption[35], and also heavily doped substrates are expected to have a higher absorption arising from the increased amount of free-carriers[36]. It shall be noted that for steady-state simulations the effect of assuming full absorption of the substrate only has a small effect on the temperature gradient.

The model is divided into a mesh of triangles, where the number of triangles defines the precision of the simulation. For optimization of the calculation time, a fine mesh is used for the substrate and a more coarse one applied to the substrate holder, as shown in Fig. 2.5(a). For the used mesh, a simulation to find the steady-state temperature of the model took around 15 sec.

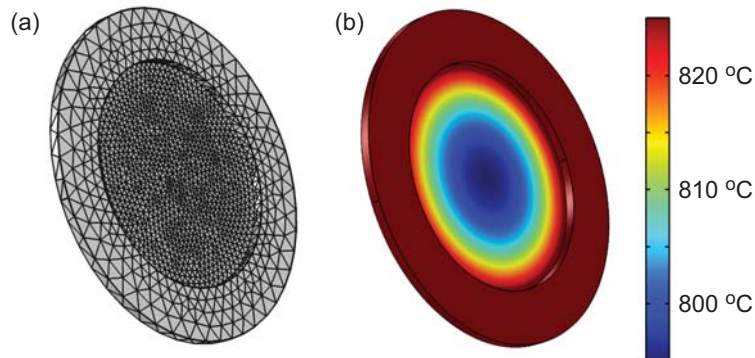


**Figure 2.5:** Finite element model and simulation of a 2 inch silicon substrate clamped in a molybdenum sample holder. (a) Model divided into a mesh of triangles. (b) Temperature profile for substrate and holder with an almost  $30\ \text{°C}$  difference from the center to the edge of the substrate.

The last parameters one needs for the modeling are the total emissivity of the materials. For undoped silicon these are very temperature dependent ranging from  $\epsilon_{\text{Si}} = 0.2$  at  $400\ \text{°C}$  to around  $\epsilon_{\text{Si}} = 0.7$  at  $600\ \text{°C}$ [37]. For molybdenum the total emissivity is more constant and it only changes from  $\epsilon_{\text{Mo}} = 0.09$  at the growth temperature to  $\epsilon_{\text{Mo}} = 0.12$  at the elevated Ga-assisted deoxidization temperature[38]. A simulation of the variation in temperature at  $800\ \text{°C}$  for a 2 inch Si substrate is shown in Fig. 2.5(b). An almost  $30\ \text{°C}$  temperature gradient is found from the center of the substrate to the edge, and with an experimental evidence of the partial Ga-assisted deoxidization, as shown in Fig. 5.4. At the growth temperature, around  $460\ \text{°C}$ , the total emissivity of undoped silicon is much closer to that of molybdenum, and the temperature gradient is less than  $3\ \text{°C}$ .

Using the framework described above, several situations are modeled, including a quarter of a 2 inch substrate and a misplaced substrate, both shown in Fig. 2.6. As expected, the quarter piece has a smaller temperature gradient than a full substrate for steady state simulations. For a misplaced substrate an almost 100 °C temperature difference is found from one side of the substrate to the other.

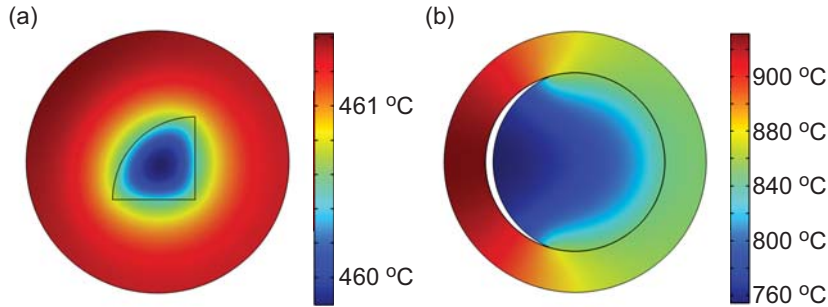


**Figure 2.6:** Temperature profile of silicon substrates. (a) Quarter of a 2 inch substrate at growth temperature. (b) Misplaced substrate at the temperature for Ga-assisted deoxidization.

The temperature gradient is roughly given by the difference in total emissivity and absorption efficiency. For GaAs substrates temperature profiles have experimentally been found to go both ways, i.e. warmest or coldest in the center, depending on the given conditions[34]. To get a more uniform temperature profile for the substrate, a backside diffuser plate made out of either molybdenum or another silicon substrate can be used. A drawback of this approach is that the efficiency of the heater decreases. Another approach would be to design a dual element heater, where the center and edge could be controlled independently[34]. This would require a calibration for each type of substrate at each temperature, but could in principal always ensure a homogenous temperature distribution.

### 2.2.5 Other Growth Systems

Epitaxial growth has been demonstrated with several other types of systems, e.g. MOCVD and CBE. In contrast to MBE, the processes in an MOCVD system do not take place in UHV, but in a controlled gas atmosphere. Organometallic precursors, with organic compounds encapsulating the required chemical elements, are transported to the substrate. There they decompose via pyrolysis, leaving the adatoms on the substrate surface. The adatoms can now diffuse around until they are epitaxially incorporated on the substrate. The precursor concentration is controlled by mass flow controllers for each specimen. Due to the much higher pressure in MOCVD growths compared to MBE, the loading and degassing process is much faster, speeding up the total growth time.

Roughly speaking CBE is a hybrid between MBE and MOCVD, with molecular beams of reactive gases in UHV. More than one species can be let in through the same injector, making it easier to achieve uniform growth on large substrates. One can also take advantage

of *in-situ* characterization such as RHEED, but carbon incorporation might be a problem compared to MBE, which tends to reduce the resistivity of the NWs[39, 40].

## 2.3 Au-Assisted Nanowires

Gold has been shown to be superior in assisting NW growth and is by far the most used material. Gold can facilitate growth for a wide range of materials at much different growth conditions, whereas other materials, such as Mn[41] and Cu[42], have not been demonstrated to have the same degree of control. Messing *et al* suggest that a combination of the good ability to form alloys with precursors, inertness to oxygen and high diffusivity to explain the good properties of gold[43]. A recent study using density functional theory calculations puts focus on the gold surface, which acts catalytically in dissociating As<sub>2</sub> molecules from the vapor phase, and forms a stable surface alloy with Ga atoms[44].

The drawback of having gold inside the growth chamber is that gold is known to incorporate as non-recombination centers and ruin the opto-electronic properties of semiconductors. The effect of the presence of gold in NW growth is much debated. A recent study shows a much lower quantum efficiency for Au-assisted InAs NWs compared to self-assisted NWs[45], however, the dimensions are not identical for the two types of NWs, and surface effects might play a role. Using aberration-corrected scanning transmission electron microscopy (STEM) Bar-Sadan *et al* have directly shown the incorporation of Au atoms in GaAs crystal with a doping concentration in the range  $10^{17-18} \text{ cm}^{-3}$  [46]. Au incorporation has also been reported for Si NWs, but at the same time not found to influence the minority carrier transport length[47].

An extensive study from Lund University found no major difference in NW growth depending on the gold deposition method[48]. They deposited gold using 6 methods, and except for a change in incubation time and annealing sensitivity, no changes in NW growth were observed. All growths were made using MOCVD, and the processing steps prior to growth, e.g. for e-beam lithography, might influence the MBE grown NWs more, as contamination is a bigger issue here.

### 2.3.1 Thin Au Film Deposition

The MBE system is equipped with an Au-effusion cell inside the growth chamber, making it possible to evaporate gold immediately prior to growth, and after all the degassing steps. Gold evaporated at an elevated temperature where gold droplets are formed spontaneously has been shown to form droplets with a more uniform size distribution compared to heating of an initially thin film.

The evaporation rate from the gold effusion cell is not absolutely calibrated, but is used relatively by controlling the deposition time, with similar results each time. The procedure was to heat the cell up to 1350 °C with a rate of 80 °C/min and let it settle for 2 min. The shutter was now opened for a short period of time ranging from 3 sec to 100 sec, but

most often 5 sec was used for growth of InAs NWs, giving a density of around  $1 \text{ NW}/\mu\text{m}^2$ . A very rough estimate is that 5 sec corresponds to 0.5 ML.

After deposition the temperature was kept elevated, typically at  $550 \text{ }^\circ\text{C}$  for InAs, for 8 min to give the gold time to coalesce into droplets. The annealing temperature was critical to control the density and size distributions of gold droplets. With tuning of the gold deposition, we could achieve InAs NWs with diameters from less than 20 nm to more than 100 nm.

### 2.3.2 Enhanced Control of Au Droplets

Gold colloids can be used to gain control of the size distribution of the droplets. Liquid solutions with uniform, suspended Au particles at a given size are commercially available. To prevent the particles from aggregating in the solution, their surface has been modified with a positive charge. To get the colloids to stick on the substrate surface, which is also positively charged, one needs to spin coat it with poly-L-lysine or apply a few droplets of hydrofluoric acid (HF). Once the colloids are in contact with the surface, they stick extremely well, and survive cleaning with acetone and isopropanol (IPA). The density and sizes of NWs can easily be controlled with colloids, but they are still spread out randomly[48].

For enhanced control of the position we used e-beam lithography[49]. The basic principle is the same as for UV lithography, except that the exposure is made with electrons. Both a Raith e-line system (Fig. 2.7(A)) and a dedicated e-beam writer (JEOL-JBX9300FS) was used for the exposures. As the e-line system was located at the Niels Bohr Institute, this was the system most used. An exposure of a full 2" inch wafer took a full weekend with the e-line system, whereas it could be made in about 2 hours with the JEOL system.

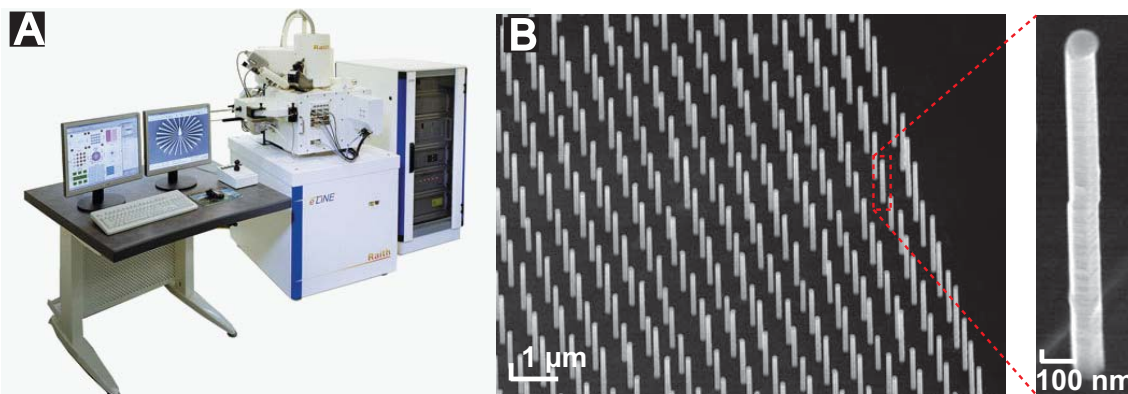


**Figure 2.7:** Electron beam lithography. (A) Photograph of a Raith e-line system, that has been the most used system for e-beam lithography for the work presented in this thesis. (B) InAs NWs grown from e-beam positioned droplets of Au. Adapted from [IV].

A typical protocol for fabricating e-beam lithography defined arrays is to dehydrate an InAs(111)B substrate for 5 min on a  $180 \text{ }^\circ\text{C}$  hotplate and then spin coat it with 2-layer resist, 6 % co-polymer and 2 % Poly(methyl methacrylate) (PMMA), at 4000 rpm. The

substrate is then transferred to the e-line system and exposed. A dot exposure configuration was used, with a beam dwell time of approximately 0.05 ms, equivalent to a dose of  $\approx 0.06$  pC, for each point. A write field of  $200 \mu\text{m} \times 200 \mu\text{m}$  was found suitable for the dot exposure, and problems with stitching was minimal. Subsequently, the substrate was developed in MBIK:IPA (1:3) developer for 45 sec and plasma ashed for 15 sec. We gave it a 10 sec dip in buffered HF and quickly loaded it into the metal evaporator. Both a thermal and e-gun evaporator were used, without any significant difference for the NW growth. A layer of around 12 nm Au was evaporated with a rate of approximately  $1 \text{ \AA}/\text{s}$ . Heated acetone (around  $60 \text{ }^\circ\text{C}$ ) was used for fast and uniform liftoff. We cleaned the substrate with acetone, methanol and IPA, and blow dried it using nitrogen.

Right before loading the substrate into the growth chamber, it was plasma etched for 45 sec and dipped in 5 % HF for 10 sec. Buffered HF was not used, as we would like the HF to dissolve any resist residues. The same growth procedure as described above was used, with the exception, that the gold was annealed at  $550 \text{ }^\circ\text{C}$  for 2 min. Longer annealing time seemed to considerably reduce the yield of NWs. A typical growth is shown in Fig. 2.7(B).

## 2.4 Self-Assisted Growth of Nanowires

Recently a new method of fabricating NWs without a foreign catalyst has been introduced for both MOCVD[50, 51, 52, 53, 54, 55, 56, 57, 58] and MBE[59, 60, 61, 62, 63, 64][VII]. Of special interest for this thesis are the papers on self-assisted InAs NWs on Si(111) substrates using MBE which have all been published within the last two years[65, 66, 67, 68, 69][I].

The advantage of omitting the gold is that one avoids contamination of both the MBE system and the individual NWs. Gold is known to be detrimental to the opto-electronic properties of semiconductors and an MBE dedicated for high electron mobility devices should therefore avoid it. Also, recent studies have shown that gold is incorporated in the NWs during growth[46, 47].

Another advantage is that growth is conducted on silicon substrates, which are much cheaper than InAs substrates, and exotic sandwich structures, such as silicon-on-insulator (SOI) can be bought from large scale manufacturers. What counts against the self-assisted growth scheme is a lower yield and a reduced control of the crystal structure.

### 2.4.1 Randomly Positioned Self-Assisted NWs

Growth of InAs NWs can be obtained directly on Si(111) substrates either on oxide free or a thin oxide layer[I]. The influence of the oxide layer is investigated in Sec. 5.1 and a general description of the growth is given here.

One way of obtaining InAs NWs on silicon is to reduce the native oxide layer by HF. By slowly lowering the substrate into a 1 % HF solution we made a gradient in the oxide layer thickness. With a dip time ranging from 0 sec to 60 sec, an approximate final thickness of the oxide layer was in the range  $15 \text{ \AA}$  to  $5 \text{ \AA}$ , as will be described in Sec. 5.1.2. The gradient made it easy to have some areas with good growth conditions, but rather difficult

to compare the exact same pre-conditions for growth. After the HF dip, the substrate was quickly loaded into the E/E chamber to avoid re-growth of the native layer.

The substrate was degassed at 500 °C for 1 hour on the HTD and for another 8 minutes at 630 °C in the growth chamber. The substrate temperature was then lowered to 450 °C with As flux on, and after a few minutes for stabilization, the growth was initiated by opening the In shutter. A very high V/III ratio was used for the growth, with typical BEPs of  $1 \cdot 10^{-5}$  torr and  $4 \cdot 10^{-8}$  torr, for As<sub>4</sub> and In, respectively. The corresponding In bulk growth rate was 100 nm/hr.

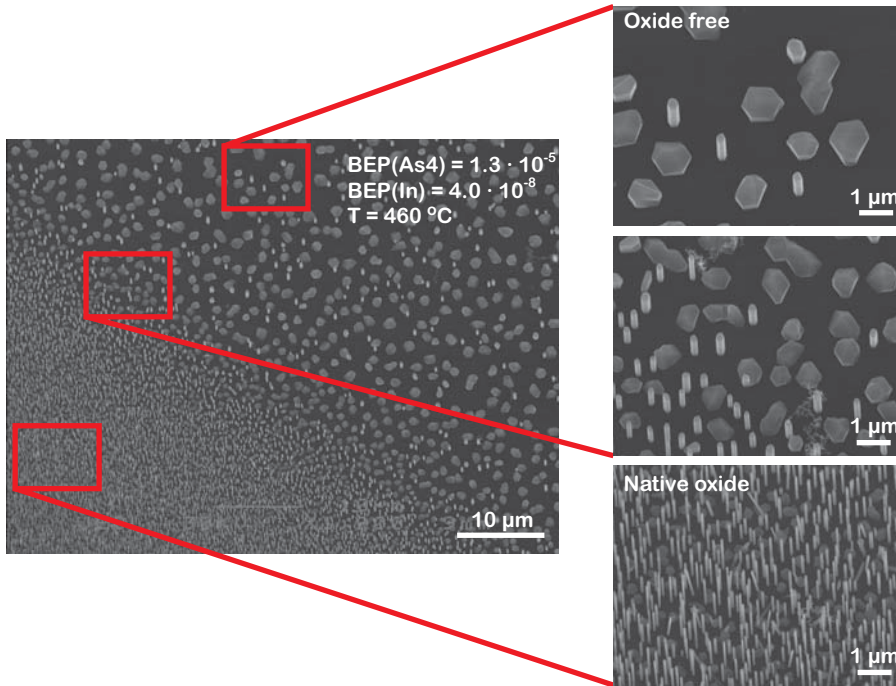


**Figure 2.8:** Self-assisted InAs NWs on Si(111). A running droplet of HF was used to make the very sharp transition of oxide free and native oxide layer.

## 2.4.2 Selective Area Growths

Exploiting a slightly different setup it is also possible to position the self-assisted NWs[53, 55, 58, 66, 70, 71, 72]. Instead of evaporating metal, one covers the whole substrate with a thick oxide layer, say 30 nm, and etches holes in it. In this selective area growth method, the position of the NWs are determined from where the adatoms can get epitaxial contact to the substrate.

The pre-treatment steps for defining holes in the oxide layer follow the procedure as for the positioned gold droplets until the evaporation of metal. Instead the substrate is etched with buffered HF for 25 sec. Before loading the sample into the MBE system it is plasma etched for 5 min and etched with 1 % HF for 60 sec.

## 2.5. VERTICALLY ALIGNED CARBON NANOFIBERS

For selective area growth the best growth results are found when all oxide is removed from the holes, and the substrates are loaded before any re-oxidization takes place. Any residues from the resist or other contamination from the pre-processing ruins the growth, and we therefore used a long plasma etching step to increase the yield of the selective area grown NWs.

Substrates have been prepared both at Univ. of Copenhagen (UCPH) using a Raith e-line system and wet etching of the holes, and at ORNL using a dedicated electron lithography system (JEOL JBX-9300) and subsequently dry etching by reactive ion etching (Oxford 100 RIE). Holes with a diameter down to 20 nm could be fabricated at ORNL, whereas the smallest holes etched at UCPH were around 100 nm. The fabrication at both places could be optimized further for obtaining smaller holes, but this was not found to be necessary in order to facilitate NW growth.

## 2.5 Vertically Aligned Carbon Nanofibers

In a collaboration with Oak Ridge National Laboratory (ORNL) we have worked on fabrication of vertically aligned carbon nanofibers (VACNFs). Carbon nanofibers (CNFs) consist of curved graphene layers stacked on top of each other with an angle  $\alpha$ [73]. The case of  $\alpha = 0$  corresponds to multiwalled carbon nanotubes, as sketched in Fig. 2.9. The length of CNFs can exceed 1 mm and their diameters are in the range a few nm to several hundred nm. Depending on the growth conditions, the graphene layers can have the form of either a cone or a cup, giving rise to a herringbone or bamboo morphology, respectively. It has been found that a plasma can be used to direct the growth direction of CNFs, and it is therefore possible to grow them perpendicular to the substrate, i.e., vertical aligned.

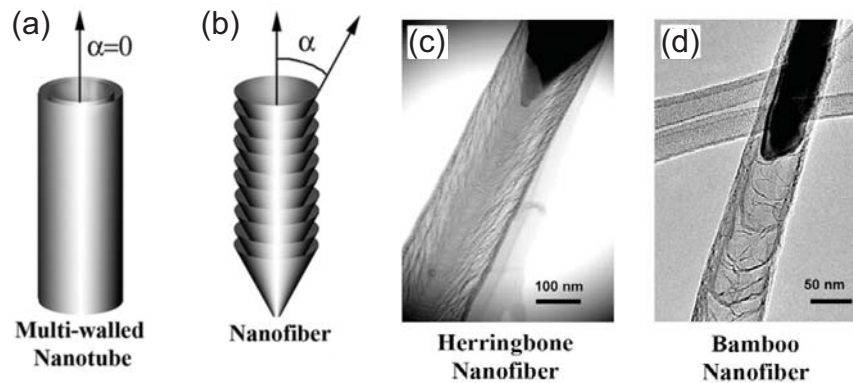


**Figure 2.9:** Structure of CNFs. (a,b) Schematic of carbon nanotubes and CNFs. The angle between the graphene layers are denoted  $\alpha$ . (c) STEM image of a CNF with herringbone structure. (d) TEM of a CNF with bamboo structure. Figure adapted from [73].

The first growth of VACNFs was reported in 1998[74], and shortly after also individual seeded VACNFs[75, 76]. A brief description of the growth process for VACNFs is given here, and an in-depth review can be found in Ref. [77]. A home-made DC plasma-enhanced

chemical vapor deposition (PECVD) system, see Fig. 2.10, was used for the synthesis of VACNFs at ORNL.

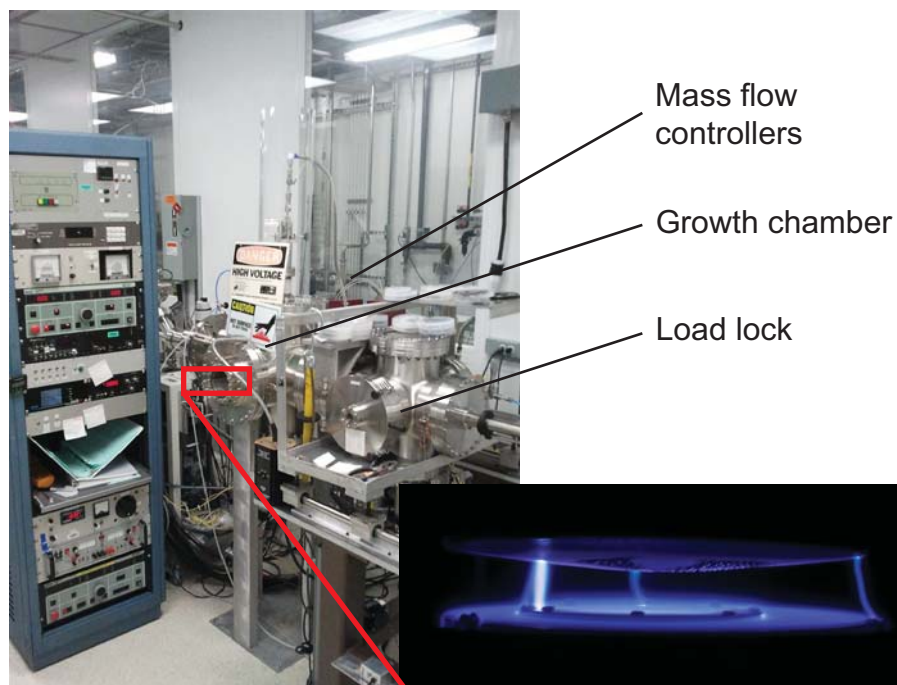


**Figure 2.10:** A DC plasma-enhanced chemical vapor deposition system. The substrate is transferred from the load lock to the growth chamber with a rod. The inset shows a look inside the growth chamber during the synthesis. Sometimes an electrical discharge arches, which might damage the substrate surfaces.

A conductive substrate is necessary for obtaining the plasma during growth, and typically doped Si(100) was used. Nickel is used as the preferred catalyst for the growth. As with Au-assisted NWs, one can use either a thin film or lithography defined areas. Single VACNFs can be achieved by either e-beam or step reduction lithography, and bunches of VACNFs by normal UV lithography. For the growth shown in Fig. 2.11, 15 nm of Ni was evaporated into 5  $\mu\text{m}$  openings with a pitch of 15-25  $\mu\text{m}$ .

The substrate was annealed at 650  $^{\circ}\text{C}$  for around 10 min before a mixture of  $\text{C}_2\text{H}_2$  and  $\text{NH}_3$  was introduced into the growth chamber at a 3 torr pressure. The acetylene supplies carbon for the growth and the ammonia prevents a continuous carbon film to form on the droplet. The growth was initiated shortly after by turning the plasma on and operating it at 450 V and 300 mA. The growth took typically 10 min, and the temperature and other parameters were maintained during growth. Some of the Ni is incorporated into the CNF during growth, and the droplet is therefore reduced with the growth time. If one maintains the growth for too long time, the Ni droplet will vanish completely and no longer serve as a protection cap for the ammonia, and eventually the VACNF will etch back and vanish.

More complicated devices with individual contact to the VACNFs were also fabricated. Here an undoped Si(100) substrate with a thick oxide layer on (> 1000 nm) was sputter coated with 10 nm of Ti and 100 nm of W to fabricate a conductive layer. It was also

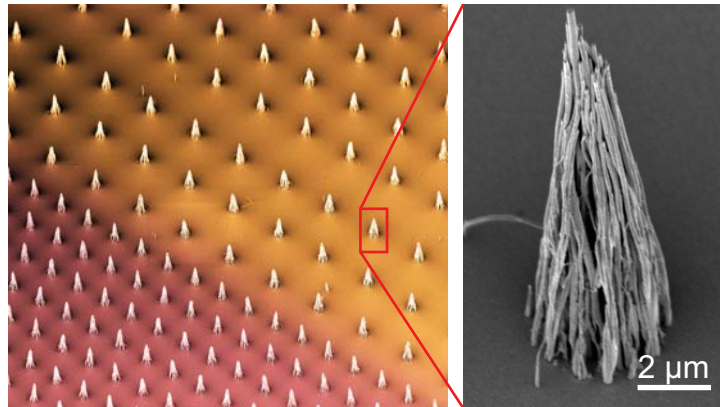


**Figure 2.11:** SEM images of VACNFs. The position of the bunches of VACNFs are defined using UV lithography.

necessary to evaporate 10 nm of Ti and 10 nm of Si to facilitate growth. During growth the conductive layer also served as the cathode for the DC plasma. Following the growth procedure described above and subsequently etch leads out by UV lithography and reactive ion etching (RIE), one could fabricate individual electrically addressable VACNFs.

In Chapter 6 the application of VACNFs to study of biological systems is described.

## 2.6 Summary

The basic concept of NW growth has been outlined with emphasis on molecular beam epitaxy and the layout of the system at the Niels Bohr Institute. Some parameters for growth of InAs NWs are given and a guide for fabricating large arrays of positioned NWs has been outlined. Both Au- and self-assisted InAs NWs have been fabricated and a more thorough study of the growth parameters can be found in Chapters 4 and 5. Also a brief introduction on how to fabricate vertically aligned carbon nanofibers has been given.



## Characterization

Electron microscopy is the most used technique for imaging NWs, where SEM is primarily used for the looking at the outer morphology and TEM for the crystal structure. Modern SEM and TEM microscopes offer a lot more possibilities for advanced analysis, including the analytical quantification of the elements with an energy dispersive x-ray module. A wide variety of microscopes have been used for the analysis of our NWs in collaboration with many groups all around the world.

X-ray diffraction experiments have also been conducted at synchrotrons for superior mapping of the facets and crystal structure of the NWs.

### 3.1 Scanning Electron Microscopy

The basic principle of a SEM is to focus a beam of electrons onto a small area on the sample and look at the re-emitted or reflected electrons, see sketch in Fig. 3.1(a).

The device for generating an electron beam is called an electron gun, which consists of a filament surrounded by a Wehnelt cylinder and an anode. A potential difference between the filament and Wehnelt cylinder (negative) and the anode (positive) accelerates the electrons, typically in the range 1 keV to 30 keV. Three types of filaments are commonly used, a tungsten wire, a lanthanum hexaboride crystal ( $\text{LaB}_6$ ), and a field emission gun (FEG) made out of a tungsten crystal. The tungsten wire works much like an incandescent lightbulb, where a high voltage across the wire facilitates the emission of electrons. The  $\text{LaB}_6$  filament works in the same way, but it has a lower work function, and is therefore more efficient. It also has a smaller energy distribution and is typically stable over a longer time. For a FEG a large electric field is applied close to the tip, enabling the electrons to tunnel out of the filament. FEG filaments have the smallest energy distribution and therefore offers the highest resolution. On the other side, they are also the most expensive and requires higher vacuum to operate.

The electron beam is aligned and focused down through the column by electromagnetic lenses. The magnetic field bends the electron path in the same way as a convex lens

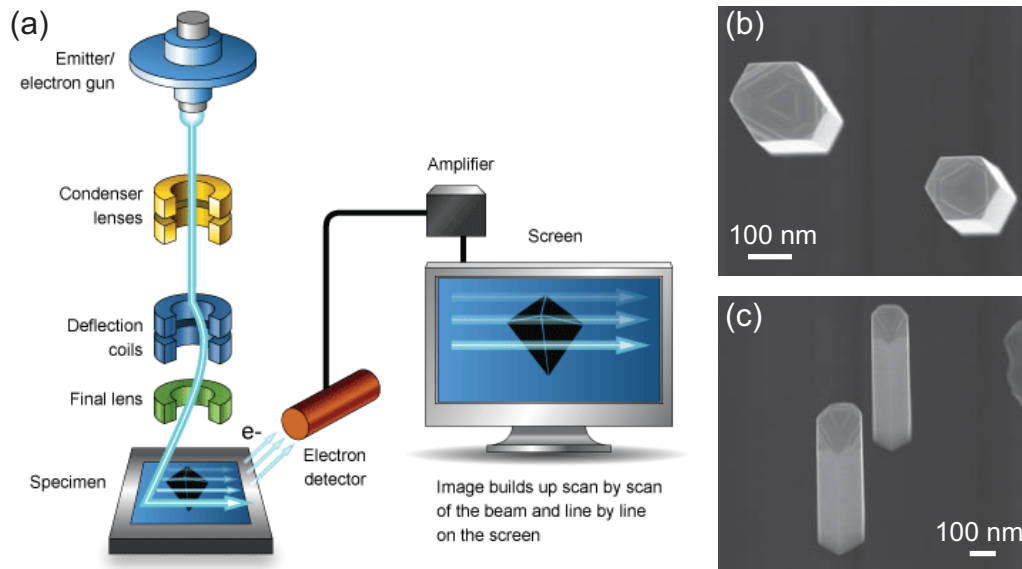


**Figure 3.1:** SEM imaging. (a) SEM layout and function. A focused beam of electrons is scanned across a surface. A photomultiplier detector collects the generated electrons and a computer put the individual points together to the final image. Adapted from [78]. (b) Top view of self-assisted InAs NWs. Their hexagonal shape can clearly be identified. (c) Side view (tilting angle  $15^\circ$ ) of the same NWs as shown in (b). The side facets can be observed.

affects light rays and focuses the beam. A major limitation in electron microscopy is that only focusing lenses are available, in other words, there exist no concave electromagnetic lens. This makes it a hard job to correct for aberration effects and, especially for TEMs, effectively define the resolution of the microscopes.

The first electromagnetic lens is called the condenser lens, and is effectively controlling the spot size of the beam. Next a set of coils is used to control the scanning of the beam and finally a lens is used for focusing the beam on the sample.

When the beam of electrons hits the sample, secondary electrons are generated from inelastic scattering. These electrons are collected by a detector positioned to the side of the sample and the signal is sent to a computer, which collects data for each point, and constructs the final image. Often it is necessary to coat poorly conducting samples with a thin metal layer, e.g. Au or Pt, to have heavy atoms the electrons can scatter on and to minimize surface charging.

### 3.1.1 SEM of Nanowires

An SEM does typically has a magnification range from 25 to around 500.000 times and a resolution of a few nm. For NWs we often used 10.000 times magnification as this allowed us to measure both the height and diameter with acceptable accuracy within a  $10 \mu\text{m} \times 15 \mu\text{m}$  imaging field. At higher magnification one can resolve the facets of the NWs and clearly see the hexagonal shape, as shown in Fig. 3.1(b,c).

The height of structures can also be measured using SEM by tilting the sample. One

### 3.1. SCANNING ELECTRON MICROSCOPY

now sees the projection of the structure and the real height can be found by the relation  $L_{\text{real}} = L_{\text{proj}} / \tan \theta$ , where  $\theta$  is the tilting angle. The often used tilting angles of  $\theta = 15^\circ$  and  $\theta = 30^\circ$  give a correcting factor of 3.73 and 1.73, respectively.

With an EDX system attached to the SEM one can make a quantification of the elements in the sample. A MERLIN SEM at ORNL was used for these studies. It was a great tool for a fast analysis of NWs and VACNFs to see if the growth had been affected by some major contamination. More detailed analysis could have been carried out, but in general we used the analytical module on a TEM instead, as better resolution can be achieved here, which will be described in Sec. 3.2.1.

The basic principle of EDX is that the high energy incoming electrons interact with atoms in the sample and excite electrons in the atomic shells. When the holes in the atomic shells are filled again with electrons from outer lying shells, the energy difference will be emitted as x-rays at characteristic wavelengths. An energy dispersive detector picks up these signals and after some accumulation time, a full spectrum giving the elemental composition of the sample is found. Each element has a unique spectrum with more than one characteristic peak, i.e. from the Lyman and Balmer series, but two peaks from different spectra may overlap. This is for instance a challenge with the L-lines for As and Ga.

#### 3.1.2 In-situ Bending Analysis of InAs NWs

In collaboration with the Research Centre for Natural Sciences in Budapest, the Young's modulus of InAs NWs has been measured on individual NWs[V]. A SEM equipped with two nanomanipulators was used for the double *in-situ* characterization. One was equipped with an AFM tip for a static bending experiment, see Fig. 3.2(A), and the other one equipped with a tungsten tip for dynamic resonance excitations, see Fig. 3.2(B,C). The bending experiments were performed by János Volk's group in Budapest, Hungary.

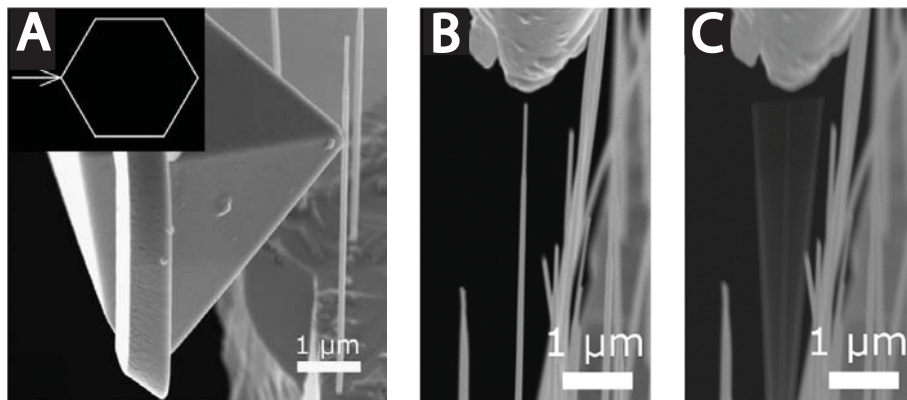


**Figure 3.2:** *In-situ* characterization of the mechanical properties of InAs NWs. (A) An AFM tip is used for bending a single NW. (B,C) A tungsten tip is used to find the resonance of the same NW with dynamic excitation. SEM image with the high frequency electric field turned (B) off, and (C) on. Adapted from [V].

The experiment was the first to use both the static bending and the dynamic resonance excitation techniques on a single NW, and we found a value of Young's modulus of  $44 \pm 14$  GPa for the mechanical bending experiment, and a value of  $35 \pm 4$  GPa for the resonance experiment, where  $\pm$  indicates the standard deviation of the measurements. These values are more than a factor of two lower than the bulk value of InAs in the [111]-direction ( $E_{111} = 97$  GPa), and also significantly lower than other reports on InAs NWs[79, 80]. This is attributed to a thin diameter of the NWs in the study and a pure WZ crystal structure. Even though theoretical calculations predict no difference in Young's modulus depending on ZB or WZ crystal structure[81], the almost defect free NWs might be the explanation for the lower value. In Ref. [80] the investigated NWs had plenty of stacking faults, and in the study by Lexholm *et al* they observe a decrease in Young's modulus for thinner NWs and at the same time claim that thinner NWs exhibit more WZ structure.

It shall be noted that the mechanical properties of ZnO NWs are studied by many groups, but the experiments give results in a broad range for Young's modulus, and a conclusive result is still lacking (see references in [V]). We plan to continue the measurements on InAs NWs in the near future to study the low value of the bending modulus in more detail.

## 3.2 Transmission Electron Microscopy

A TEM is used for looking at individual NWs and especially for investigating their crystal structure. The components, i.e. electron gun and lenses, are similar to those in a SEM, but the layout of a TEM is much related to an optical microscope (OM) with the change that one uses electrons instead of light rays. A sketch comparing the two types of microscopes is shown in Fig. 3.3.

The condenser lens is used for focusing the beam onto the sample. For a thin sample part of the beam will pass through, and the objective lens collect all beams originating from the same point on the sample to one point, and with the projector lens it can be directly observed on a viewing screen or a CCD camera. This is illustrated with the black lines in Fig. 3.4. In a TEM one can also choose to project the back focal plane, where all electrons diffracted in the same direction independently of origin on the sample, is collected into a single point, as shown with the red lines in Fig. 3.4. Such an image is known as a diffraction pattern and will be describe in the next section.

The resolution of a microscope is approximately given by

$$d \approx \frac{\lambda}{2NA}, \quad (3.1)$$

where  $\lambda$  is the wavelength of the incoming particles used for imaging and NA is the numerical aperture. In a TEM the electron beam is also generated using an electron gun, but accelerated to much higher energies than in a SEM, with a typical range of 80-300 keV. At these energies it is necessary to correct for relativistic effects, and the wavelength of

### 3.2. TRANSMISSION ELECTRON MICROSCOPY

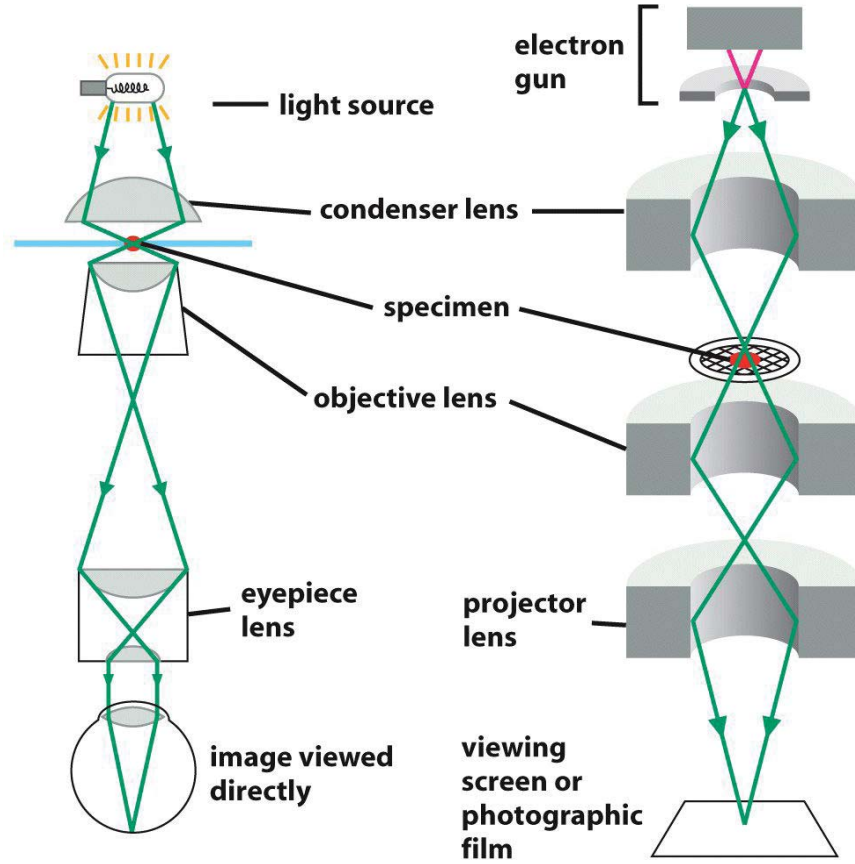


**Figure 3.3:** Comparison between an optical microscope (left) and a TEM (right). Light rays are interchanged with electrons and glass lenses with electromagnetic lenses. Adapted from [82]

electrons can be found by[83]

$$\lambda_e \approx \frac{h}{\sqrt{2m_0E(1 + \frac{E}{2m_0c^2})}}, \quad (3.2)$$

where  $m_0$  is the electron rest mass,  $h$  is Planck's constant and  $E$  is the energy of the electron. For 200 keV electrons this gives a wavelength of 0.025 Å, which in principle should improve the resolution with more than a factor of 100.000 compared to OM. However, aberration effects are much bigger, which seriously affect the NA, limiting the resolution of the best TEMs to 'only' around 0.5 Å.

The sample should be sufficiently thin for the electrons to pass through, and often the sample preparation is a major issue in TEM imaging. On the other side the sample should not be too thin as the diffraction will then be too weak. Fortunately the diameters of NWs are in just the right range, 10 nm to 200 nm, and the only challenge is to transfer them to a carbon grid. We have used a mechanical transfer method, where the carbon grid is scratched directly on the substrate, which breaks the NWs at the bottom. If one is

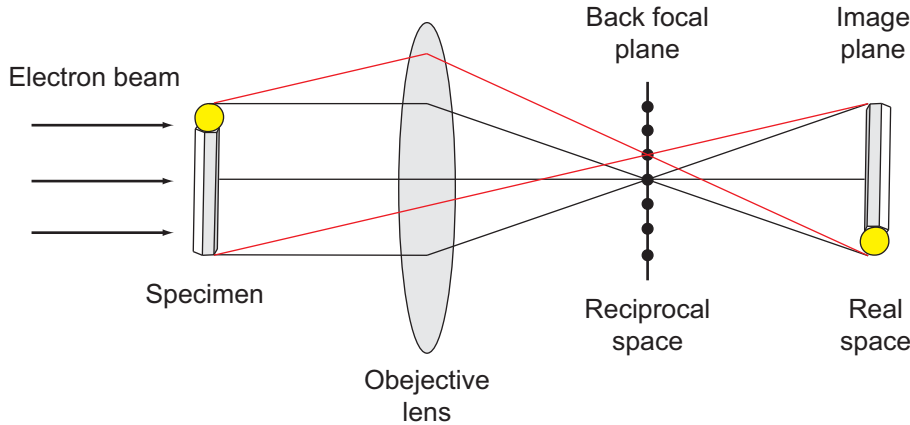


**Figure 3.4:** Sketch of electron rays when obtaining an image and diffraction image. Electrons originating from the same point on the sample are collected at the same point in the image plane (black lines), whereas electrons diffracted in the same direction independent of origin is collected at the same spot in the back focal plane (red lines).

interested in the substrate-nanowire interface, the focused ion beam (FIB) technique can be used, where a piece of the substrate is cut out using energetic ions.

### 3.2.1 Quantization of Elements

Like in a SEM, energy-dispersive X-ray spectroscopy can be used for an elemental analysis of the sample. By focusing the beam down to a small spot size it is possible to obtain quantitative data from a specific points on the NW. The TEM at the Niels Bohr Institute, a Philips CM20, was upgraded with an EDX detector in the summer 2011. We have shown that it is possible to detect even small segments (around 20 nm) of InGaAs in InAs NWs using this setup, as shown in Fig. 3.5.

To calibrate the EDX measurements the Cliff-Lorimer technique can be used[83], under the assumption that a thin foil specimen is investigated, that is, there is no significant absorption or fluorescence of the x-rays on their way out of the sample. For NWs this should be a safe approximation, and the Cliff Lorimer factor  $k_{AB}$  can be found using the ratio,

$$\frac{C_A}{C_B} = k_{AB} \frac{I_A}{I_B} \quad (3.3)$$

where  $I$  is the intensity of an element and  $C$  the elemental percentage of an element. When more than two elements are present a Cliff Lorimer factor should be calculated for each ratio using Eq. 3.3 and correlated using the fact that the molecular fraction of all elements should sum to unity, i.e.

$$C_A + C_B + \dots + C_N = 1. \quad (3.4)$$

Software for EDX analysis uses theoretical values of the Cliff Lorimer factors, and are able to do more or less all the analysis with a single click. This is extremely useful to find the area of interest and for on-the-fly analysis. For a detailed analysis it gives more

### 3.2. TRANSMISSION ELECTRON MICROSCOPY

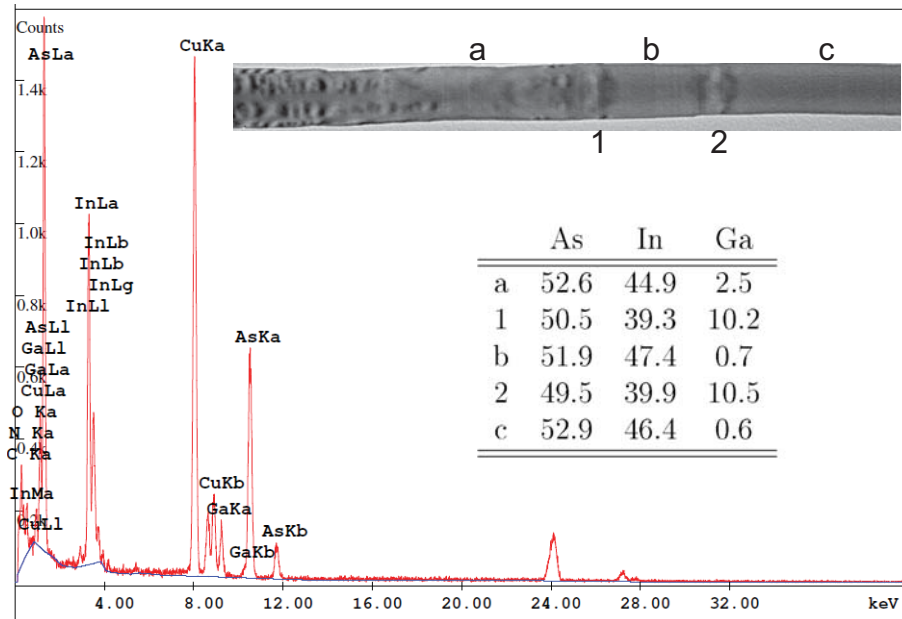


**Figure 3.5:** EDX spectrum of the second InGaAs barrier in an InAs NW with two barriers. Inset shows TEM brightfield image of the NW with the numbers (1,2) indicating the position of the barriers, and the letters (a,b,c) positions away from the barriers where EDX data have been obtained.

accurate results to do the quantification by hand. Here one needs a background correction and a reference sample, ideally with the exact same shape, with a well known elemental composition. For InAs NWs with  $\text{In}_{1-x}\text{Ga}_x\text{As}$  barriers, where  $x$  is the Ga mole fraction, we used the InAs segment near the tip as the reference sample, as this part is expected to not contain any Ga, neither from the axial growth or from radial overgrowth[84]. By depositing pure GaAs NWs on the same TEM grid it is possible to also find a precise value of the  $k_{\text{Ga,As}}$  Cliff Lorimer factor. At the sacrifice of some precision, one can in a ternary system use Eq. 3.4 to find the last element. A last thing to note, is that, it is important to estimate the Cliff Loremer factors for each sample and for each run at the microscope, as daily fluctuations will give rise to uncertainties. The table inset in Fig. 3.5 shows the quantification obtained with a Philips CM-20 TEM and using the algorithm provided by the EDAX software.

#### 3.2.2 Scanning Transmission Electron Microscopy

A scanning transmission electron microscope (STEM) is typically a TEM where the electron beam is focused to a very small spot size and then scanned over the sample. The technique is well suited for compositional analysis, as both EDX data and an image can be obtained simultaneously.

Furthermore, using a high-angle annular dark-field (HAADF) detector, a  $Z$ -contrast image can be obtained, where the contrast is directly related to the atomic number. For high angles the electrons scatter on the nucleus, known as Rutherford scattering, and a

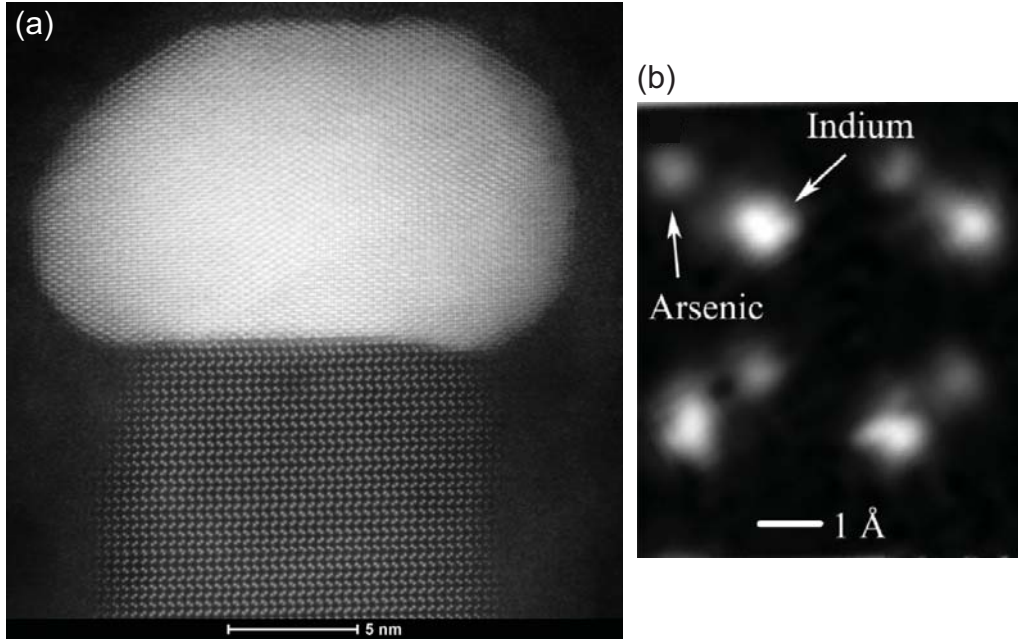


**Figure 3.6:** HAADF STEM images of NWs. (a) Thin GaAs NW. With intensity analysis of each dumbbell As and Ga atomic columns can be distinguished. Image by Erik Johnson. (b) High magnification image of an InAs NW where the atoms can be seen to be paired in dumbbells. The columns of In and As atoms can easily be resolved due to their large mass difference. Figure adapted from [85].

heavy nucleus will therefore scatter more electrons. For thin samples the image intensity can be approximated by an power function of the form  $I \sim Z^\nu$ , where the exponential factor  $\nu$  equals 2 for Rutherford scattering. However, the electron cloud always screens the potential of the coulomb potential of the bare nucleus. No exact value of  $\nu$  exist, but it is of the order  $\nu \approx 1.7$ [86]. HAADF is therefore difficult to use as an exact quantification method, but is well suited for relative studies of elements in the same specimen. The composition of heterostructures has previously been investigated by EDX for MBE grown NWs[85] and for MOCVD grown NWs [84, 87, 88]. The barriers are directly visible in the image and several single point EDX measurements or EDX line scans have been used for element analysis. In Ref. [II] HAADF STEM is used for measuring the length of heterostructure segments in NWs.

With detailed computer analysis of images like the one shown in Fig. 3.6(a), the intensity difference between the GaAs dumbbells can be resolved, and it is possible to tell the termination of the growth direction. For InAs NWs, Fig. 3.6(b), the intensity difference in the dumbbells can be resolved much more easily, due to a large mass difference.

### 3.3 Diffraction

The crystal structure of a sample can be analyzed using the diffraction pattern, which, among others, can be obtained using TEM or monochromatic light. In a TEM the electrons

### 3.3. DIFFRACTION

are scattered on the columns of atoms and in a x-ray experiment on the atomic planes. To understand how diffraction patterns arise one needs to be familiar with the reciprocal space. To aid teaching we have developed an experiment for demonstration of 2D diffraction which can be conducted in a class room. An introduction to diffraction will be given here based on this experiment and a more thorough description can be found in Ref. [IV].

#### 3.3.1 Light Scattering on a Nanowire Array

*Part of the text adapted from Ref. [IV].*

The wavelength of the incoming waves, i.e. monochromatic x-rays, is typically matched to the structure of interest. In this experiment we use a single non-tunable laser as the monochromatic wave source and instead custom make an array of NWs to fulfill the diffraction conditions. The ratio of the NW pitch to the laser wavelength ( $\sim 3 \mu\text{m}/0.532 \mu\text{m} \simeq 6$ ), is directly comparable to the ratio of a typical crystal lattice spacing to synchrotron generated x-rays ( $\sim 3 \text{ \AA}/0.5 \text{ \AA} \simeq 6$ ). An example of the diffraction experiment is shown in Fig. 3.7 together with SEM images of the sample.

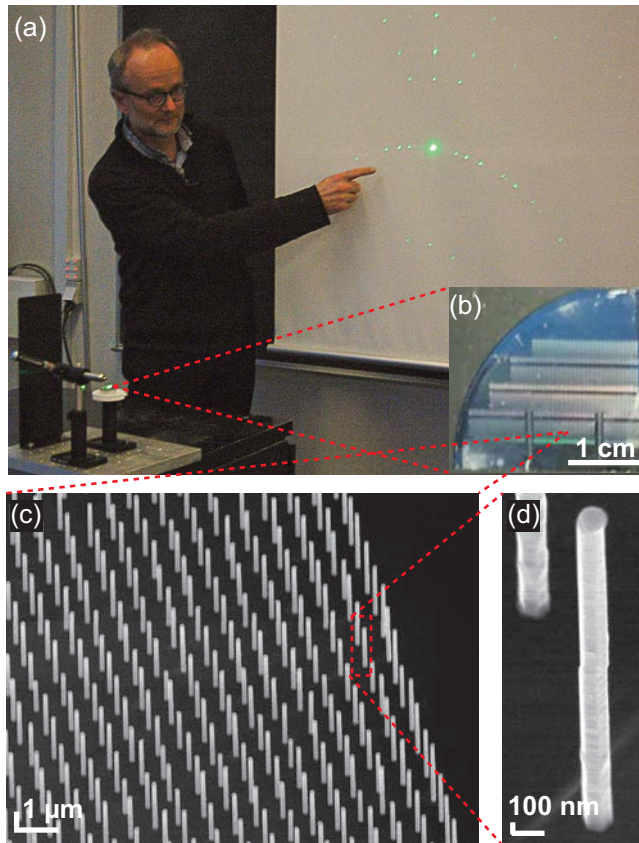


**Figure 3.7:** Class room demonstration of the reciprocal space by light scattering on an array of NWs. (a) Simple setup of the demonstration experiment. (b) Optical image of the substrate (quarter of a 2 inch wafer) with ordered arrays of NWs. The different densities can be distinguished by their color. (c,d) SEM images of the NW array. Adapted from Ref. [IV].

Diffraction arises from interference of light when scattered on transparent planes. Scattering on atoms can be regarded as scattering on planes, see Fig. 3.8(a), and is described by Bragg's law,

$$2d \sin \theta = n\lambda, \quad (3.5)$$

where  $\lambda$  is the wavelength of the incoming wave,  $n$  is an integer,  $d$  is the lattice spacing and  $\theta$  is the angle between the incoming wave and scattering planes. From Eq. (3.5) it is seen that Bragg's law is only satisfied for  $\lambda \leq 2d$ .

One can also use the Laue condition [89],

$$\Delta \vec{k} = \vec{G}, \quad (3.6)$$

to describe scattering from planes using vector formalism. Here the scattering vector  $\Delta \vec{k}$  is defined as the difference between the diffracted and incoming wavevector,  $\vec{k}' - \vec{k}$ , and  $\vec{G}$  is a reciprocal lattice vector given by

$$\vec{G} = h\vec{b}_1 + k\vec{b}_2 + l\vec{b}_3, \quad (3.7)$$

where  $\vec{b}_1$ ,  $\vec{b}_2$  and  $\vec{b}_3$  are unit vectors of the reciprocal space, and  $h$ ,  $k$  and  $l$  are integers known as Miller indices[90].

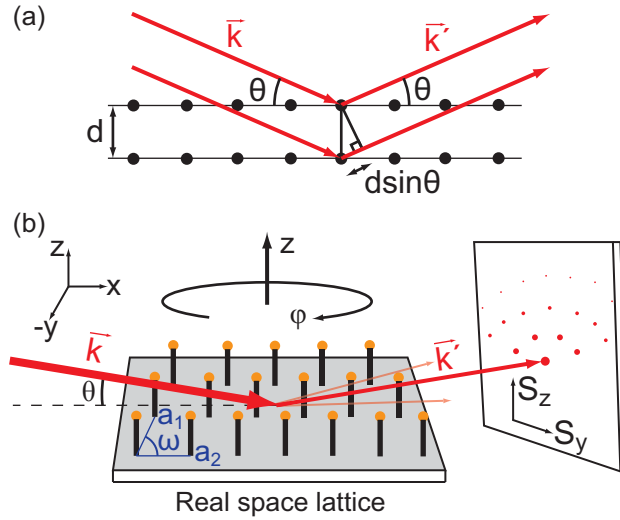


**Figure 3.8:** Diffraction. (a) Sketch of Bragg's law of diffraction. (b) Diffraction on 2D NW array. Adapted from Ref. [IV].

For an interpretation of the Laue condition, one can look at an algebraic statement of the scattering wave vector, as in Ref. [89]. For elastic scattering, where no energy is transferred to the crystal, the magnitude of the scattering wave vector can be written as,

$$|\Delta \vec{k}| = 2|\vec{k}| \sin \theta. \quad (3.8)$$

By substituting the Bragg condition  $2d \sin \theta = \lambda$  and  $|\vec{k}| = 2\pi/\lambda$  into Eq. 3.8 one obtains  $|\Delta \vec{k}| = 2\pi/d$ . It is seen that the scattering wave vector is a representation of real space

### 3.3. DIFFRACTION

parameters with a characteristic scaling factor of  $2\pi$ . One should note that the typical length scale in the reciprocal space is  $2\pi$  over the typical scale in real space.

The exact position of the diffraction spots can be calculated using the Laue condition Eq. (3.6) and geometric interpretations of the total system. A sketch of the diffraction is shown in Fig. 3.8(b), where all quantities are geometrically defined. Monochromatic light is coming in from the left, represented by the incoming wave vector  $\vec{k}$ . In our case it is a laser source, but it could in principle be any monochromatic waves, e.g. synchrotron generated x-rays when the lattice spacing is on the atomic scale. The incoming light scatters on the nanowires, which are positioned in a 2D array spanned by the real plane lattice vectors  $\vec{a}_1$  and  $\vec{a}_2$ . The diffracted beams that fulfill the Bragg conditions will give rise to diffraction spots observed on a screen a distance  $L$  from the crystal. The positions of diffraction spots are calculated as a horizontal  $S_y$  and a vertical  $S_z$  distance from origo on the screen, where origo is set to be right between the 0th order diffraction spot, also called the specular spot, and a not visible spot from a beam passing directly through the sample without any reflection or scattering.

For orthogonal lattice vectors, i.e.  $\omega = 90^\circ$ , the horizontal deflection on the screen is given by

$$S_y = L \cdot \frac{\frac{h}{d_1} \sin \phi + \frac{k}{d_2} \cos \phi}{\frac{1}{\lambda} \cos \theta + \frac{h}{d_1} \cos \phi - \frac{k}{d_2} \sin \phi}, \quad (3.9)$$

and the vertical deflection on the screen is,

$$S_z = L \cdot \frac{k'_z}{\frac{1}{\lambda} \cos \theta + \frac{h}{d_1} \cos \phi - \frac{k}{d_2} \sin \phi}. \quad (3.10)$$

An in-depth study was conducted on a rectangular array of InAs NWs with a pitch of  $3 \mu\text{m}$  and  $4 \mu\text{m}$ , see Fig. 3.9. A HeNe-laser beam was scattered at the sample and the diffraction pattern observed for a full  $360^\circ$  rotation. At all angles the diffraction points could be unambiguously labeled using Miller indices, and their positions fitted using Eqs. 3.9 and 3.10. The results are shown in Fig. 3.9(e). The structure factor of the artificial crystal could be determined with an accuracy of less than 1%, by comparing the calculated to the experimental position of the diffraction spots.

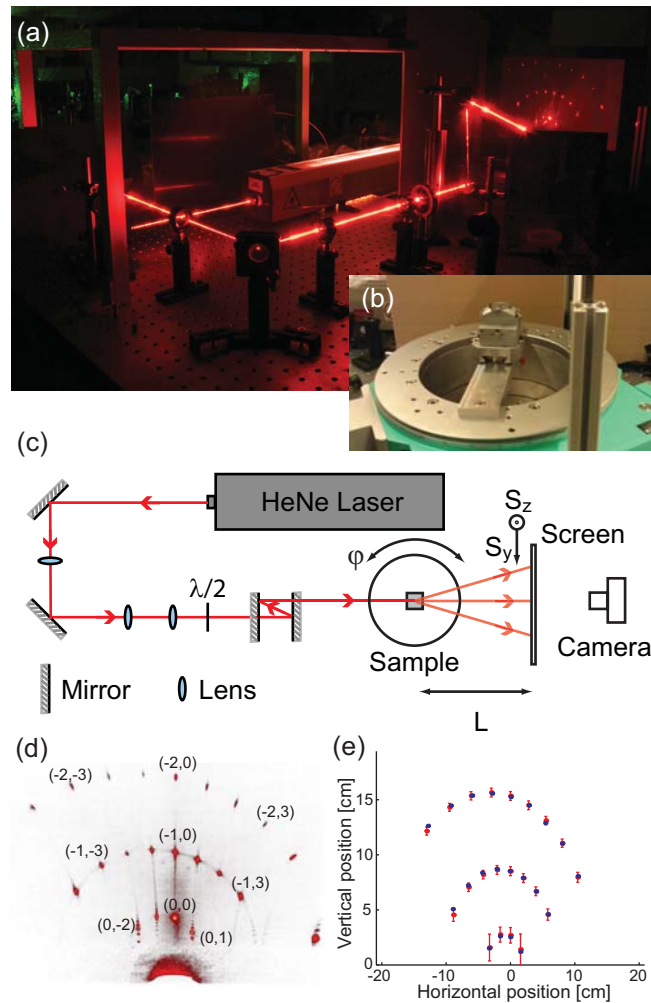


**Figure 3.9:** Experimental determination of the diffraction spots. (a) Image showing the full setup and the aligning of the laser on the sample and the diffraction pattern. (b) Sample mounted on a two-axis goniometer on top of a  $360^\circ$  turn table. In (c) a sketch of the setup is shown. The light is collimated using the first lens, and a small beam adopted using the next two lenses put in a telescope configuration. The two mirrors next to the sample, is elevating the beam, and pointing it down at the sample with an angle  $\theta = 15.6^\circ$ , close to Brewster's angle for InAs. (d) Optical image of the diffraction spots on the screen. All spots can be unambiguously quantified and labeled using Miller indices. (e) Experimental and theoretical position of the diffraction spots. Adapted from Ref. [IV].

### 3.3.2 Crystal Structure of Nanowires

The crystal structure of III-V NWs when grown in the  $[111]$ -direction usually has the WZ or ZB structures, though higher periodicity structures have also been reported[91]. In stacking combination of the atomic layers, WZ can be described by an ABAB... periodicity, whereas ZB follows an ABCABC... periodicity. In Fig. 3.10 models of a ZB and WZ crystal have been simulated using the freeware program VESTA[92]. The crystals are viewed along the  $[111]$  or  $[0001]$  axis, respectively, and some of the most common planes for TEM diffraction have been indicated.

A rotational twin in the ZB crystal structure, ABCA-CBAC, rotates the crystal  $60^\circ$  around the  $[111]$  growth axis. In the terminology this should be differentiated from a stacking fault (SF) as the stacking sequence before and after is not identical[93]. On the other hand, a single ZB layer in a WZ crystal, ABA-C-ACA, can be referred to as a SF, as the crystal here is indistinguishable before and after the unfamiliar layer.

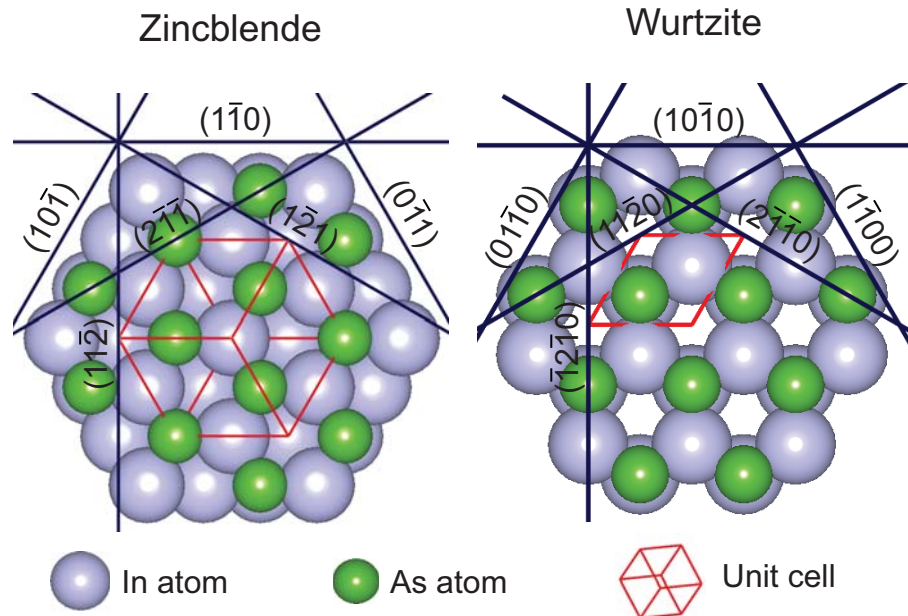


**Figure 3.10:** Models of the cubic ZB and hexagonal WZ crystal structures viewed along the NW growth direction, that is, the  $(111)$  and  $(0001)$  direction, respectively. Some of the most important planes used for TEM imaging has been indicated.

The ZB crystal structure consists of two interpenetrating face-centered cubic (fcc) lattices of group III and group V elements shifted  $(\frac{1}{4}, \frac{1}{4}, \frac{1}{4})$ . It is also known as the diamond structure, but with two different elements alternating at each site. For many III-V semiconductors, ZB is the only observed crystal for bulk materials, as it has the smallest energy.

In NWs where the surface energy also plays a role for crystal formation, the WZ crystal structure is also observed. Very thin InAs NWs exhibit pure WZ structure as the surface effects are now dominant, but thicker NWs with WZ structure can also be obtained by tuning of growth parameters. The WZ structure consists of two hcp lattices shifted  $(0, 0, \frac{3}{8})$ .

Often one applies the 4-index notation ( $hkil$ ), where  $i = -(h + k)$ , for indexing hexagonal crystals. This notation makes it easier to identify families of crystal planes, for instance, it is not obvious that the planes  $(110)$  and  $(2\bar{1}0)$  are related, whereas it becomes clear when using the 4-index notation for the same planes:  $(11\bar{2}0)$  and  $(2\bar{1}\bar{1}0)$ , as also shown in Fig. 3.10. In general, the 4-index notation is used when referring to the hexagonal WZ structure, and the 3-index notation for the ZB structure.

Common diffraction patterns along the main zone axis are shown in Fig. 3.11. As can be seen, the ZB and WZ diffraction patterns are identical for a beam direction along the  $[11\bar{2}]$  and  $[\bar{1}\bar{1}00]$  directions, respectively. To determine the crystal structure one therefore needs to tilt the sample  $30^\circ$ , so the incoming beam is along either the  $[\bar{1}10]$  or  $[11\bar{2}0]$  direction. More common diffraction patterns can be found in Refs. [94, 83].

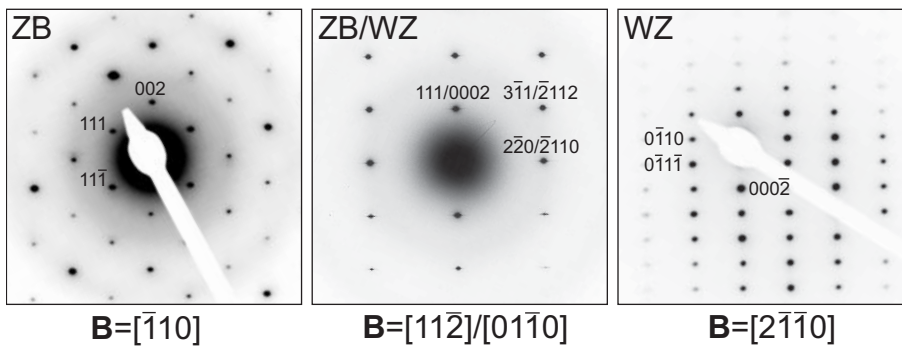


**Figure 3.11:** Common diffraction patterns from InAs NWs. For an incoming beam along the  $[11\bar{2}]$  direction for ZB crystals the diffraction pattern is identical to that from WZ crystals along the  $[\bar{1}\bar{1}00]$  direction. Thus, for crystal structure analysis of NW we image along the  $[\bar{1}10]$  or  $[11\bar{2}0]$  axis. More diffraction patterns for ZB and WZ crystal structures can be found in Refs. [94, 83].

The operation of a TEM is an art in itself and it takes many hours of practice to obtain good images and diffraction patterns. With a double tilt sample holder it is in principle always possible to rotate the sample onto the zone axis. However, when imaging a grid with many NWs deposited, it is preferable to find a NW which already lies close to the zone axis, and then use the tilting functions for fine tuning. Another trick when imaging NWs is to make a rough alignment in BF mode by tilting the sample back and forth, and look if some NWs turn black, as this indicates they scatter most of the beam. However, sooner or later one will need to perform a precise alignment of the sample, and here the diffraction pattern is a great help. For a thick, but not too thick, sample (say 100 nm) Kikuchi lines can be used as guides. They arise from multiple internal scattering and do not turn on and off like the diffraction spots. It is therefore much easier to rotate the sample in relation to a Kikuchi line than diffraction spots which vanish all the time.

When the NW has been aligned along a zone axis, i.e. one is looking directly down the columns of atoms, the rows of atoms can be imaged directly in a high-resolution TEM (HR-TEM) or STEM (Fig. 3.6).

Most often diffraction images are obtained using the selected area electron diffraction (SAED) technique. In SAED a parallel beam is incident on the sample and the size

of the diffraction area is controlled by an aperture over the sample. Evaluation of the crystal structure in small areas can be conducted with convergent beam electron diffraction (CBED). Here a cone shaped beam is incident on the sample with a very small spot size, down to around 10 nm on our TEM. Instead of the usual spot diffraction pattern, a pattern with disks is obtained.

### 3.3.3 Dark Field Imaging

Dark field (DF) imaging is also known from OM, where the unscattered light is excluded from the image. The sample will appear bright and the background dark, as there is nothing to scatter to the light here. In electron DF imaging one looks at a real space image using diffracted electrons from only one direction. In an experiment this is set up by sliding in an aperture in the back focal plane only selecting one diffraction spot. As the spot is located off-axis the image will suffer from low intensity and aberration effects. A better approach is therefore to tilt the incoming beam, so the selected diffraction spot is in the center of the diffraction image and then the image on-axis.

By using a special method of DF called weak-beam dark field (WBDF), where the sample is tilted away from the zone axis, we have deduced the orientation of sidefacets on self-assisted InAs NWs. It is more tricky than it sounds to find the orientation, as only a projection of the NW is seen in normal TEM. However, in WBDF thickness fringes becomes visible, and one can find the flat facets. The drawback of WBDF imaging is the lower intensity of the image, and it is therefore necessary to either increase the beam intensity or extend the capture time.

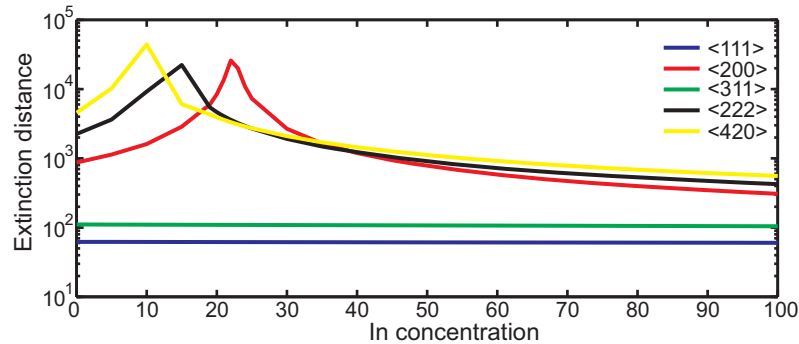


Figure 3.12: Calculations of the extinction distances for the InGaAs system.

In WBDF microscopy the sample is tilted away from the zone axis. A popular configuration is the  $\mathbf{g}(\mathbf{3}\bar{\mathbf{g}})$  configuration[83], where the beam is tilted so the  $\mathbf{3}\bar{\mathbf{g}}$  diffraction spot appears bright, and then the  $\mathbf{g}$  spot is used for the DF image.

The intensity of the diffracted beam in a perfect crystal is given by

$$|\phi_g|^2 = \left(\frac{\pi t}{\xi_g}\right)^2 \frac{\sin^2(\pi t s_{\text{eff}})}{(\pi t s_{\text{eff}})^2} \quad (3.11)$$

where  $s_{\text{eff}}$  is the effective excitation error,  $\xi$  is the extinction distance and  $t$  is the thickness of the specimen. The excitation error is a measure of the deviation from the exact Bragg condition and can be estimated from the position of the Kikuchi lines according to the diffraction pattern. The effective excitation error is defined as

$$s_{\text{eff}} = \sqrt{s^2 + \frac{1}{\xi_g^2}}. \quad (3.12)$$

The extinction distance is the periodicity for which the intensity oscillates with depth in the sample. It can be calculated by

$$\xi_g^2 = \frac{\pi V_c \cos \theta_B}{\lambda F_g} \quad (3.13)$$

where  $V_c$  is the volume of a unit cell,  $\lambda$  is wavelength of the electrons, and  $F_g$  is the structure factor  $F(\theta_B)$  for the  $\mathbf{g}$  reflection. The structure factor is calculated using the software JEMS, which contains crystallographic tables for the atomic scattering factor. Data for a ZB InGaAs crystal in a 200 keV system is shown in Fig. 3.12. A drastic increase in the extinction distance is found for an In concentration around 20 % for some of the reflections. In principle it should be possible to detect barriers looking at the thickness fringes, but the grown NWs all had a Ga concentration of less than 40 %, and in this region the extinction distance is almost constant.

A WBDF image is shown in Fig. 3.13(a) and the corresponding diffraction image obtained on-axis, i.e. before tilting the sample. The diffraction patterns show ZB and twinned ZB structures viewed from the [110] direction. Two possibly scenarios exist to obtain such an image: (1) A NW with {110} facets is lying on a facet, Fig. 3.13(c), or (2) the NW has {112} facets and lying on an edge, i.e. if it is partly buried in the TEM grid. These two cases are indistinguishable in BF TEM, so for determination of the side facets orientation, WBDF was used. The sample was tilted away from the zone axis and hence the excitation error  $s$  was increased, such that the number of thickness oscillations increases. In Fig. 3.13(a) the thickness fringes can be seen dimly at the edge. For further analysis the derivative of the intensity was found for an area across the NW as shown in Fig. 3.13(b). Now 8 and 9 fringes can be resolved on either side of the NW. The distance between the fringes can be found from Eq. 3.11 and noting that a maximum occurs with a periodicity of  $ts_{\text{eff}} = 1$ . The excitation error was deduced from the Kikuchi lines and diffraction pattern, giving  $t = 26$  nm between two intensity peak maxima. The number of fringes (9) multiplied by the distance between them, gives a total thickness of 234 nm for the NW. Under the assumption that the NW is lying on a flat as sketched in Fig. 3.13(c), the thickness is correlated to the width by a factor of  $\cos(30^\circ)$ , that is, for a measured width of 293 nm, the height is found to 255 nm. From the placement of the fringes and the good agreement with the NW height, we can deduce that the image was obtained in scenario (1) where the NW lies on a side wall, and therefore that self-assisted InAs NWs exhibit {110} side facets. This is in agreement with SEM studies, where it has been found that the NW side facets are in epitaxial relationship with {110} cleavage planes on the substrate.

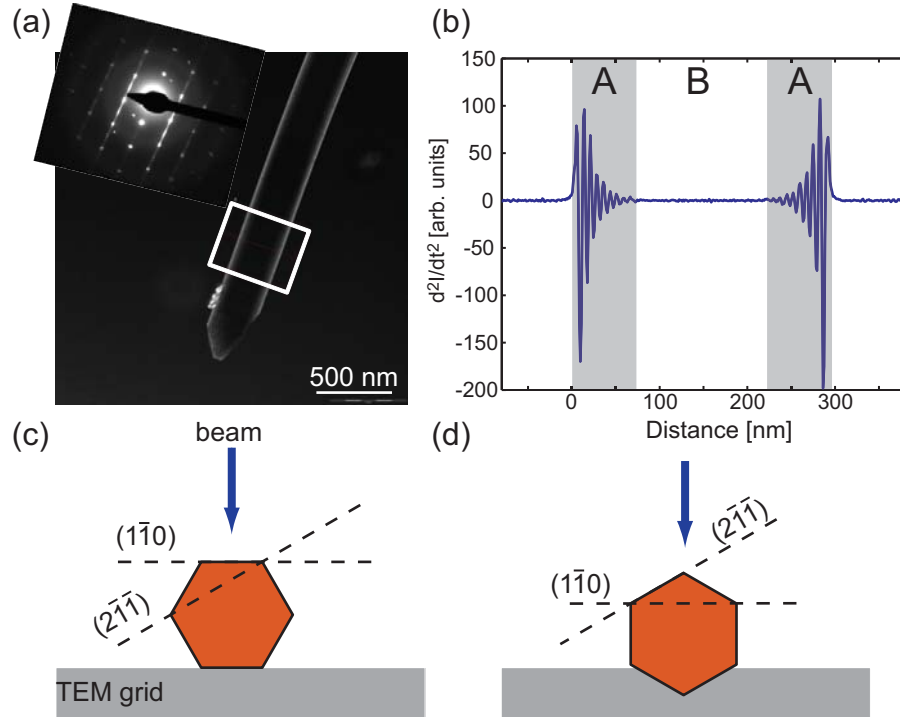


**Figure 3.13:** WBDF image of a self-assisted InAs NW. Inset shows the on-axis diffraction pattern, ZB in the  $[110]$  direction. (b) Second derivative of the intensity across the NW for the area marked with a white box in (a). The width of the section with intensity fringes are almost equal to the sections without fringes, i.e.  $2A \approx B$ . The corresponding sample thickness between maxima of two intensity peaks are found to 26 nm for the given configuration of the TEM. (c) Sketch of NW with  $\{110\}$  facets and (d)  $\{112\}$  facets giving rise to the diffraction pattern shown in (a). From the thickness fringes it can be seen that the NWs belong to the type with  $\{110\}$  facets.

### 3.4 Monochromatic X-rays Diffraction

High flux monochromatic x-rays are generated by a synchrotron, in which electrons are accelerated to relativistic speeds and kept there in a storage ring. The energy of the accelerated electrons scales with the size of the storage ring, and experiment are conducted at large scale facilities, for instance, the SPring8 synchrotron in Japan shown in Fig. 3.14(a). When travelling in a circular path electrons will emit energy by radiation due to acceleration. This was used for first generation light synchrotrons. Nowadays more advanced insertion devices, such as a wiggler, is used to 'shake' the electrons at certain places in the storage ring, to generate a high quality x-ray beam. The quality of the radiation is termed *brilliance*, and is defined as<sup>[95]</sup>

$$\text{brilliance} = \frac{\text{Photons/sec}}{(\text{mrad})^2(\text{source area in mm}^2)(0.1 \% \text{ bandwidth})}. \quad (3.14)$$

A high flux monochromatic beam focused to a small spot over a very large distance is seen to give the highest brilliance. The beam is focused in beam lines of up to 1 km, see

left part of Fig. 3.14(a), to achieve this. We have conducted experiments at the BM11XU beamline at the worlds largest synchrotron SPring8 in Japan. The beam size was around  $0.5 \times 0.5 \text{ mm}^2$  during our experiments, but could be reduced with around a factor of 100, enabling measurements on single NWs. Furthermore an MBE chamber was attached to the beamline, facilitating *in-situ* growth experiments, as will be described in Sec. 5.3.

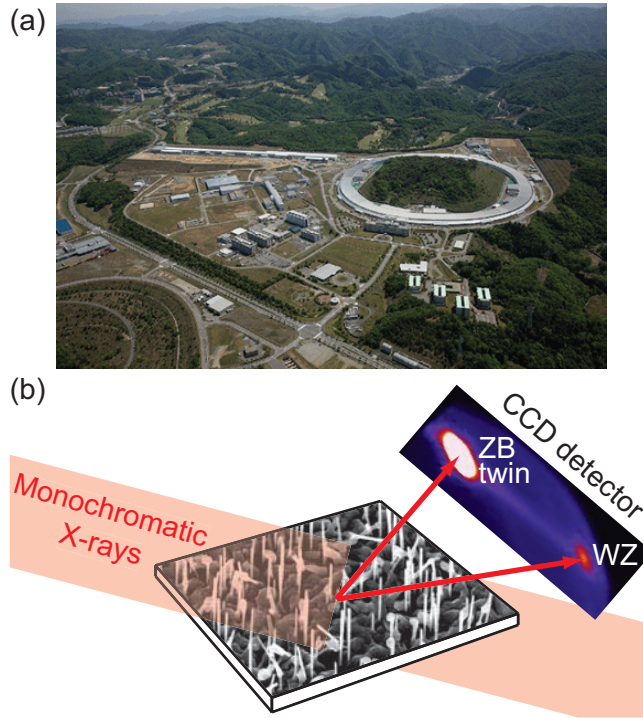


**Figure 3.14:** Facility and setup for X-ray diffraction. (a) Image of the worlds largest synchrotron SPring8 in Japan. Adapted from [www.spring8.or.jp](http://www.spring8.or.jp). (b) Sketch of a diffraction experiment on NWs. The intensity of the diffraction peaks imaged by the CCD detector scales with the amount of the given crystal structure. Adapted from [III].

The alignment of the sample is a critical step for obtaining good diffraction data. The crystal the NWs are grown on is used for this alignment process as it is much bigger and only exhibit the ZB crystal structure. Homoepitaxial InAs NWs is a greater challenge here, as the ZB background from the InAs substrate is much greater than the ZB signal from the NWs, but one can still look at the WZ structure in the NWs. Heteroepitaxial grown NWs, i.e. InAs on Si, are easier to align, as the Bragg peaks from the InAs and Si are non-overlapping due to different lattice constants.

The software spec was used for controlling the system and obtaining data. The first step in the alignment is to find the center of the sample, and then find some of the well known diffraction Bragg peaks. When alignment is made, one moves around in the reciprocal space using the  $(hkl)$  coordinates, instead of moving the angles of the detectors manually.

One method for evaluating the crystal structure of a sample is to perform scans along the crystal truncation rods. Since the in-plane lattices are identical for all possible stacking

### 3.5. SUMMARY

sequences in NWs, we can use the crystal rod scans to map all Bragg points, and obtain knowledge of the crystal composition. A set of 300 images was obtained along the  $[01l]$  rod for the out-of-plane reciprocal space coordinate  $l$ . For dataanalysis a Matlab script was written to analyze a small region of interest (ROI) in the center of the detector. The integrated intensity of this area is plotted as a function of  $l$  in Fig. 3.15. Each peak in the graph indicates a given type of crystal structure. In the shown measurement we found both ZB, twinned ZB, and WZ, the exact amount of each is difficult to determine due to a large background signal, especially for small angles, i.e. low  $l$  values.

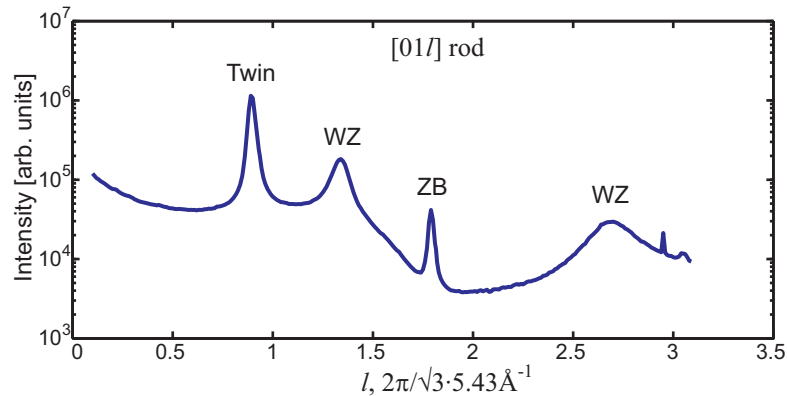


**Figure 3.15:** Scan along the  $[01l]$  crystal truncation rod of self-assisted InAs NWs obtained at SPring8. WZ and ZB Bragg peaks have been identified.

For the *in-situ* growth measurements we let the detector stay at one position, and followed the evolution the intensity of a Bragg peak with time. The integrated intensity of the Bragg peak could now be directly related the total amount of the crystal.

## 3.5 Summary

Electron microscopy is the most used method for characterization of NWs. SEM is well suited for analyzing the outer morphology of the NWs and obtain information of the height, diameter, and density. Information of the shape and side facets can also to some degree be obtained by SEM. For higher resolution TEM is used, where high energy electrons are sent through the sample, enabling atomic resolution. By looking at the diffraction pattern the inner morphology of the NWs can be determined. Using the weak-beam dark-field technique we have shown a method for estimating the side facet orientation of the NWs. Furthermore the elemental composition can be analyzed with an EDX detector, where characteristic x-rays generated in the sample is used for quantification. As an example, InGaAs barriers in InAs NWs have been investigated in different microscopes. Finally, we have shown how to use monochromatic x-ray diffraction for analysis of NWs.



## Au-assisted InAs Nanowire Growth

In this chapter we look at Au-assisted NW growth on InAs(111)B substrates. Gold is by far the most common material for inducing growth of semiconductor NWs, but other materials have been used for InAs with comparable results [96, 97, 98]. For Au-assisted growth pure ZB and WZ InAs NWs have been fabricated, depending on the growth temperature and V/III ratios[99, 100].

The basic properties and procedures for applying Au have already been discussed in Sec. 2.3, and we will instead focus on optimization of the growth process. The aims of the systematic studies were to fabricate perfect arrays of e-beam defined NWs for interfacing with mammalian cells (see Chap. 6) and produce defect free NWs for quantum transport measurements. Both goals were achieved and resulted furthermore in an interesting study of experimental determination of effective diffusion lengths.

### 4.1 Optimization of Basic Growth Parameters

For a systematic study of the basic growth parameters, we began by optimizing the deposition of gold. Roughly speaking, the size of the gold droplet gives the diameter of the NW, if one stays in a regime without radial growth. For *in-situ* Au deposition one can control the sizes of the droplets by the evaporation time, the annealing temperature and the annealing time, as described in Sec. 2.3.1. The crystal structure of the NWs is also heavily influenced by the droplet diameter with pure WZ crystal structure for thin NWs (Fig. 4.1(a)) and super-twinned ZB for thick NWs[18, 101] (Fig. 4.1(b)).

To our knowledge, super-twinned NWs have not previously been reported for MBE grown pure InAs NWs. However, the results are not surprising, as several groups have shown it for MOCVD grown wires[18, 101], and we attribute it to the underlying dynamics of the growth mechanism, and not a specific growth method. On the other hand, it shall be noted that super-twinning is only observed for positioned arrays of NWs in our MBE system, where the pre-processing requires many chemical steps and thereby a greater risk of contamination. MOCVD systems are run at higher chamber pressures and also have

residues from decomposition of the precursors, making it more likely with contamination of the sample. Also, for InP NWs the twinning has been shown to be controlled by incorporating Zn as impurities[18].

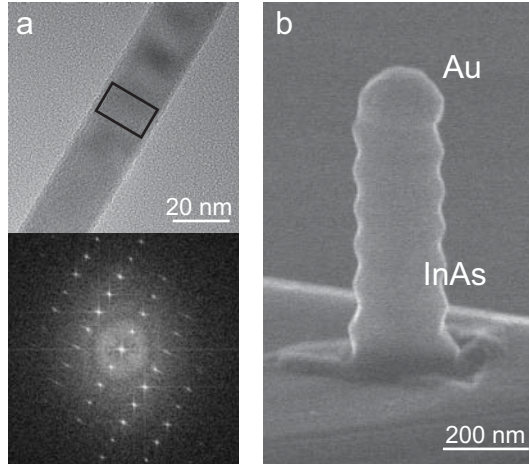


**Figure 4.1:** Electron microscope images of InAs NWs. (a) HR-TEM image of a thin InAs NW. Image by Erik Johnson. The inset shows the fast fourier transform of the boxed area having pure WZ structure. (b) Cross-sectional SEM image of a thick NW with a super-twinned ZB lattice.

### 4.1.1 Growth Temperature

The temperature window in which growth is possible is very narrow, and in order to grow vertical high-aspect NWs, one has to find the growth temperature within a  $\sim 20$  °C gap. To avoid reflections from the sources the temperature was measured just before the growth start using a pyrometer.

SEM was used for characterization and an area of  $100 \mu\text{m}^2$  was analyzed for each growth to find the densities. A few degrees temperature gradient is observed across the substrate, and the analysis is therefore only based on NWs from the center part of the substrate.

As seen from Fig. 4.2 where a thin gold film (5 sec) have been evaporated *in-situ*, the density of NWs is within a factor of 2 for different growth temperatures and beam fluxes. However the morphology of the NWs changes dramatically depending on the growth temperature. For temperatures below 420 °C, many wires are growing in a non-perpendicular direction with respect to the substrate, which can be explained by multiple order twinning at the growth interface in the beginning of the growth[102]. For temperatures above 445 °C the NWs are found to have considerably radial overgrowth. For even higher temperature, some of the wires show a bulge formation, which is due to too much material collected at the droplet[III]. Based on these results we kept a constant growth temperature of 425 °C, which is in good agreement with other reports of MBE grown InAs NWs [26, 103]. For all used beam fluxes, this growth temperature was found to give vertical NWs and optimal growth rate.

#### 4.1. OPTIMIZATION OF BASIC GROWTH PARAMETERS

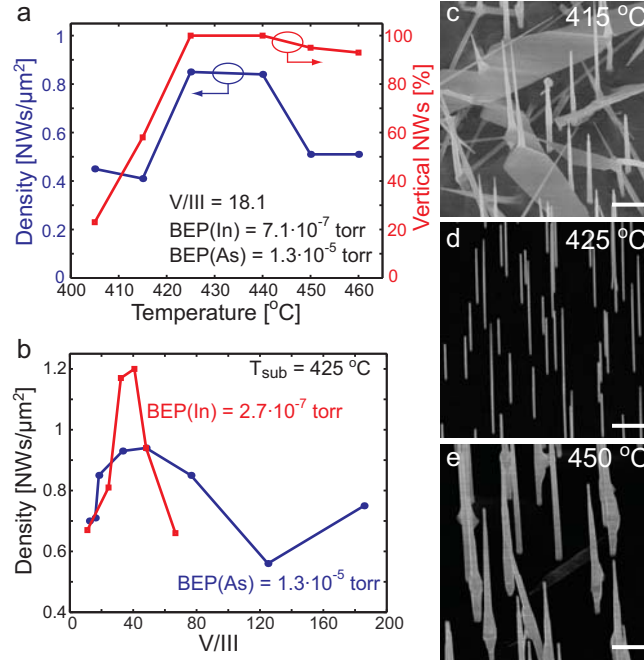


**Figure 4.2:** Study of densities of InAs NWs. (a) Influence of the substrate temperature for the density and amount of vertical nanowires. At low temperature a large amount of the NWs is standing non-vertical with respect to the substrate. For high temperatures almost all NWs are found to stand vertical with respect to the substrate, but the density is lower than for 425  $^{\circ}\text{C}$ . The optimal growth conditions are only found in a very small window around 425  $^{\circ}\text{C}$  and this value was used as the growth temperature for all subsequently growths. (b) Density as a function of the V/III ratio for both constant As flux (blue) and In flux (red). All densities are found by counting the NWs in a 100  $\mu\text{m}^2$  area in the center of the substrate. (c-e) SEM images for growth at different temperatures. The growth at 425  $^{\circ}\text{C}$  gives the most regular NWs with least side growth. Tilt angle is 15 $^{\circ}$  and scale bars are 1  $\mu\text{m}$ . Adapted from [II].

#### 4.1.2 Molecular Beam Fluxes

The dimensions, i.e. width and length, of the NWs were investigated as a function of the group III and V fluxes, see Fig. 4.3. The In beam flux can only be controlled by adjusting the cell temperature, whereas the As can also be adjusted using a needle valve. All lengths and diameters were measured from SEM images using ImageJ, and the results are given as the mean of all obtained values with error bars indicating the standard deviation.

The axial GR is taken as an average of the final length to the total growth time (30 min for all growths, except for the growth with BEP(In) =  $7.1 \cdot 10^{-5}$  torr, where it is only 20 min). The GR is not constant, but the mean GR can still be used to compare the growth conditions. To estimate the radial growth rate, a low flux growth, where we expect no radial growth, is taken as the reference, and the increase in diameter is obtained with regard to this. We have found a 'native' NW diameter of  $(55 \pm 10)$  nm for our standard method of applying gold. For the lowest As flux the mean diameter is smaller, but we attribute this to changes in the initial nucleation favoring only the small droplets to nucleate.

For both In and As the axial GR is seen to scale linearly with the beam fluxes for the

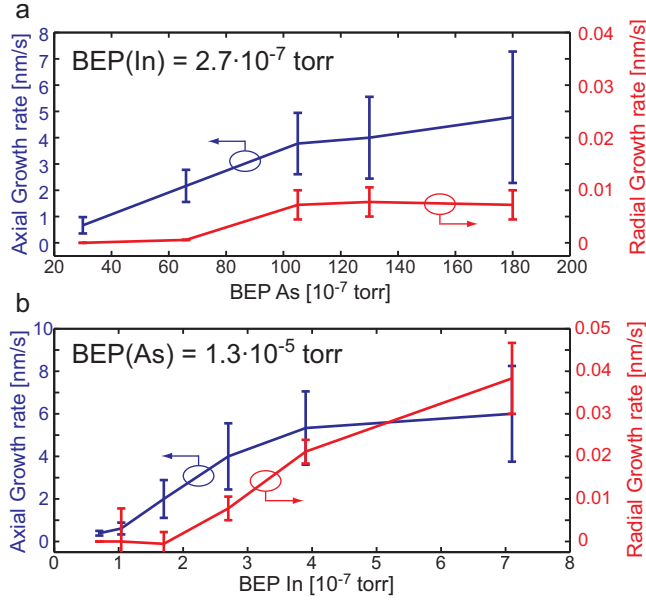


**Figure 4.3:** Growth rates of InAs NWs depending on beam equivalent pressures (BEPs). (a) For a constant  $\text{BEP}(\text{In}) = 2.7 \cdot 10^{-7}$  torr the growth rate is almost independent of As flux when  $\text{BEP}(\text{As}_2) > 1.0 \cdot 10^{-5}$  torr, indicating a group III limited growth. (b) For a constant  $\text{BEP}(\text{As}_2) = 1.3 \cdot 10^{-5}$  torr the axial growth rate scales with the In flux in the region  $1 - 4 \cdot 10^{-7}$  torr, and the growth is therefore assumed to be group III limited. Error bars indicate the standard deviation and minimum 30 NWs from each growth have been analyzed. Adapted from Ref. [II].

lowest fluxes, and then saturate for the highest fluxes. For fluxes of  $\text{BEP}(\text{As}_2) = 1.8 \cdot 10^{-5}$  torr and  $\text{BEP}(\text{In}) = 2.7 \cdot 10^{-7}$  torr (bulk equivalent growth rate of 700 nm/hr) the length of some of the wires exceeds  $20 \mu\text{m}$ , giving an average growth rate of 11 nm/s, almost 3 times higher than other reported GRs of InAs NWs using MBE[104].

For a constant In-flux, Fig. 4.3(a), a highly As-rich environment is reached for a BEP above  $1.0 \cdot 10^{-5}$  torr, in which the NW morphology only changes little by increasing the As-flux further. As the growth rate is still lower than obtained for higher In-fluxes, we contribute this to an In limited growth regime. For the growth series with constant As-flux, Fig. 4.3(b), the saturation in NW length for increased In-flux can be explained by the increased radial growth rate. In other words, the diffusion of In to the droplet reaches an almost steady level, and the In is instead incorporated directly at the sidewall. For all grown NWs the average axial growth is at least 200 times larger than the radial, but for other growth temperatures and longer growth times, this ratio will decrease.

NWs without overgrowth are most easily obtained by low flux conditions, but at the cost of a low axial GR. We have found an optimal spot using  $\text{BEP}(\text{As}) = 1.3 \cdot 10^{-5}$  torr and  $\text{BEP}(\text{In}) = 1.7 \cdot 10^{-7}$  torr (bulk equivalent GR of 400 nm/hr), giving plenty of NWs in each batch with a length exceeding  $5 \mu\text{m}$  and with minimal overgrowth. Under certain circumstances the overgrowth might actually be beneficial to obtain thick NWs with a pure crystal structure[105], and it will be discussed in Sec. 4.3.

For NWs grown with  $\text{BEP}(\text{As}) = 1.3 \cdot 10^{-5}$  torr and  $\text{BEP}(\text{In}) = 1.7 \cdot 10^{-7}$  torr (bulk equiv-

alent GR of 400 nm/hr), the crystal structure is found to be WZ with around 70 stacking faults per  $\mu\text{m}$ . The side facets are determined to be the  $\{1\bar{1}00\}$  family using weak-beam dark field microscopy (see Sec. 3.3.3), which is in agreement with other studies of NWs grown at a similar temperature [100, 106, 40].

## 4.2 Experimental Determination of Diffusion Lengths

*This section is partly adapted from Ref. [II]*

By tailoring the growth and position of InAs NWs, experimental values for the effective diffusion lengths of adatoms on both the substrate and NW sidewalls have been deduced. Data are fitted using a mass continuity growth model for group III elements, based on a simple kinetic but informative treatment without use of thermodynamic parameters, as introduced in Sec. 2.1.1. Shared substrate diffusion areas and shadowing effects are included in the model, which both tends to decrease the effective flux.

Thermodynamic effects, such as nucleation barrier and desorption from the droplet, are not included in the growth model. Instead we use incorporation coefficients as correction factors for the thermodynamic effects [31]. Three effective incorporation coefficients,  $k_s$ ,  $k_w$ , and  $k_d$ , for the substrate, sidewall, and droplet, respectively, are introduced. The  $k_s$  and  $k_w$  factors give the probability for an adatom landing on the substrate or sidewall within the collection zone to get incorporated at the liquid-solid NW growth interface, while  $k_d$  relates to the net flux into the droplet from the vapor phase. Smaller effective diffusion lengths will not give the same result as including the incorporation coefficients, as the shared collection area only depends on the diffusion lengths. In an experiment the difference is reflected in how nearby NWs share material based on the diffusion lengths, whereas the effective incorporation coefficients are constant with respect to the pitch.

The diffusion to the NW growth interface of adatoms impinging on the substrate decreases with growth time due to longer diffusion length and a rough planar growth on the substrate. When the NW length increases, the adatoms will have to travel longer before they arrive to the NW growth interface. One would then expect a contribution from the substrate until a length equal to  $\lambda_{\text{III},w}$  is reached. At the same time, a rough planar growth will tend to decrease the diffusion length of adatoms, as they will have more available sites for incorporation in planar growth. At the initialization of the growth we have a planar surface, and with time, the roughness increases. In connection with the NW length we expect the contribution from the substrate only to contribute to the NW growth for NWs significantly shorter than  $\lambda_{\text{III},w}$ . For simplicity we only use the NW length  $L(t)$  at time  $t$  as the parameter to correct for the reduced diffusion. The substrate diffusion length is then,  $\lambda_{\text{III},s}(t) = \lambda_{\text{III},s}(L(t)) = \lambda_{\text{III},s}(1 - \alpha L(t))$ , where  $\alpha$  is a fitting parameter. For a model without planar growth we would expect  $\alpha = 1/\lambda_{\text{III},w}$  and for increased surface roughness during growth  $\alpha > 1/\lambda_{\text{III},w}$ .

A calculation of the influence of a shared collection area and more details of the mass continuity growth model can be found in Refs. [II] and [XII]. We find the NW growth rate,

$J_{\text{NW}}$ , in a group III limited regime is given by

$$J_{\text{NW}} = \frac{dL(t)}{dt} = J_p \frac{k_s \pi \lambda_{\text{III},s}^2(t) + k_w dL(t) \tan \phi + k_d \frac{\pi d^2}{4}}{\frac{\pi d^2}{4}}. \quad (4.1)$$

where  $d$  is the diameter of the NW,  $\phi$  the angle of the incoming beam and  $J_p$  is the bulk equivalent planar growth rate measured using RHEED. Eq. 4.1 is valid when the diffusion length on the sidewalls is longer than the length of the NW. When the length of the NW gets larger than the sidewall diffusion length,  $L(t)$  is interchanged with  $\lambda_{\text{III},w}$  in the second term of Eq. 4.1. The differential equation can be solved analytically using the condition  $L(0) = 0$ . However, here we choose to solve it numerically and include the effects from shadowing, time dependent diffusion lengths and incorporation coefficients at each iteration.

The effect of shadowing is calculated for NWs positioned in a regular array with pitch  $p$ , in contrast to Ref. [107] where the shadowing is calculated based on a statistical probability approach. The shadowing affects both the flux of adatoms impinging on the NW sidewalls and on the substrate as shown in Fig. 4.4. The distances to neighbor NWs are indicated in the schematic in the inset. Distances marked with blue lines are used for the shadowing calculations, whereas the red line indicates NWs that are omitted, as they are on the same line of sight as other NWs.

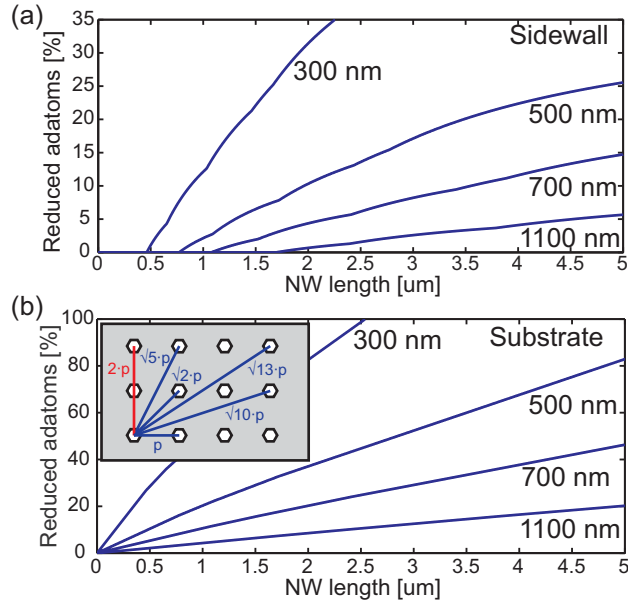


**Figure 4.4:** Simulated effects of shadowing on (a) sidewalls and (b) substrate for NWs positioned in a quadratic grid as a function of length for pitches in the range 300 nm to 1100 nm. The inset is a schematic of NWs in an array and the distances to their neighbors are indicated. NWs on the same line of sight as other NWs are excluded from the calculations, as indicated with a red line. The angle of the incoming beam is set to  $33^\circ$  and the NW diameters are set to 80 nm. Adapted from Ref. [II].

### 4.2.1 Diffusion Parameters for an Array of Nanowires

In one experiment to estimate the diffusion lengths on the substrate and sidewalls, e-beam positioned NWs were grown with a pitch ranging from 400 nm to 7  $\mu\text{m}$  in blocks of around  $50 \times 50$  NWs. Details of the e-beam lithography process can be found in Sec. 2.3.2. The NWs were grown with a  $\text{BEP}(\text{As}_2)=1.4 \cdot 10^{-5}$  torr and  $\text{BEP}(\text{In})=2.1 \cdot 10^{-7}$  torr (bulk equivalent growth rate of 500 nm/hr), and from the flux optimization experiments described in Sec. 4.1.2, we therefore expect the growth to be in As-rich conditions, where the GR is limited by the group III material.

Both NWs in the center, which are completely surrounded by other wires, and NWs at the edge of the grid, which only have neighbors to half the sides, were used for the analysis, and the results are shown in Fig. 4.5(a,b). The error bars indicate the standard deviation and at least 30 NWs were used for pitches smaller than 2  $\mu\text{m}$ , and 10 NWs for larger pitches.

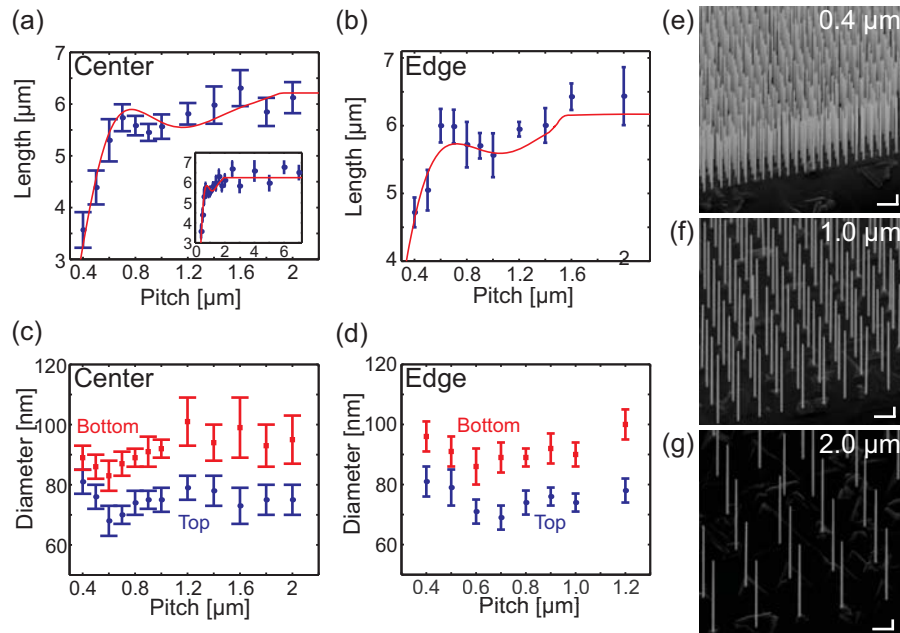


**Figure 4.5:** InAs NWs grown in positioned arrays. (a,b) Experimental data of the mean length of the NWs for the center and edge of each grid with NWs. Error bars indicate the standard deviation. The solid line is a fit to the data using a mass transport growth model. (c,d) Diameter of NWs from both the center and the edge of a lithography defined array. The NWs have a slight tapering and the diameter is stated for both the bottom and top. (e-g) SEM images of arrays. Tilting angle is  $30^\circ$  and scale bars 1  $\mu\text{m}$ . Adapted from Ref. [II].

The diameters of the NWs are shown in Fig. 4.5(c,d) for both the bottom and just below the gold droplet. The NWs exploits a little tapering, with a linearly decreasing diameter throughout the length, but no sign of syringe or barrel-like shapes[107]. The tip diameters for each pitch have been used for the simulations and the radial growth has been accounted for by the incorporation factors.

The adatom diffusion growth model is used to fit the final length of the NWs depending on the pitch and the measured diameter. Data are simultaneously fitted to the NWs at the edge and in the center of the array, with the differences being the influences of shared substrate diffusion and shadow effects. Many parameters are in play, and for simplicity we keep the droplet incorporation factor  $k_d$  constant at unity, i.e. all adatoms directly impinging on the droplet are incorporated. We find it reasonable to assume that a group III adatom impinging on a liquid droplet will stick with a higher probability than on the sidewalls, which we later estimate to  $k_w = 0.70$ . The best fits to the data shown in Fig. 4.5 were found for a sidewall diffusion length  $\lambda_w = 3.0 \mu\text{m}$ , and an effective maximum substrate diffusion length of  $\lambda_s = 0.80 \mu\text{m}$  with  $\alpha = 1$ , that is, the contribution from the substrate diffusion is decreasing until a NW length of  $1 \mu\text{m}$ . The incorporation factors for In are found to be  $k_s = 0.05$  and  $k_w = 0.70$  for the substrate and sidewalls, respectively.

As can be seen in Fig. 4.5 the length of the NWs increases when the pitch is increased until 700 nm, hereafter it decreases slightly with a local minimum at 1000 nm, and then goes up to a steady maximum level at around  $2 \mu\text{m}$  pitch. For NWs near the edge a similar trend is observed, here with a local minimum at 900 nm. The diameter also depends on the pitch with a local minimum at a pitch of 600 nm. Using the Student's  $t$ -test, the local maximum in NW length at a 700 nm pitch is considered to be statistically significant.

For MOCVD grown NWs a peak in the length has been reported as synergetic growth[108], where nearby catalyst particles decompose the metal-organic compounds. This cannot explain the observation here, as the mean length is larger for low-density wires, i.e. a pitch over  $2 \mu\text{m}$ . Plissard *et al* also observe similar results for InSb grown NWs using MOCVD, and contribute it to local variation in the V/III ratio[109]. Again, this cannot be the full explanation in our case, as we get the longest wires for pitches over  $2 \mu\text{m}$ .

The local maximum and then local minimum before reaching an even higher mean length must be due to more than one effect. The two most contributing effects are the shared substrate diffusion and variation in diameters, with the latter having the largest impact. The origin of the size variations in diameters can be caused by a locally different V/III ratio due to shadowing or shared substrate diffusion.

The unavoidable planar bulk growths between the NWs are also influenced by the pitch, both from diffusion to the NWs and shadowing of adatoms (group III *and* V). A rough planar growth will tend to decrease the diffusion length of substrate adatoms, as they will have more available sites for incorporation. One can in principle take bulk morphology into account by having a diffusion length that depends on the pitch and growth time. However, we have chosen a substrate diffusion length that only depends on the NW length and geometrically derived shared collection areas as a simplification to the complex dynamics of NW growth.

### 4.2.2 More Diffusion Parameters and Summary

Heterostructured InAs NWs with 11 InGaAs NWs have been used for a comparable study of diffusion lengths. HAADF STEM was subsequently used for measuring the length of each segment, and the mass continuity growth model to fit data to these lengths. Details

## 4.2. EXPERIMENTAL DETERMINATION OF DIFFUSION LENGTHS

of the growth and analysis can be found in Ref. [II]. The fitting parameters for both experiments have been summarized in Tab. 4.1 and comparable values are estimated.

Fit	$\lambda_w^{\text{In}}$	$\lambda_s^{\text{In}}$	$k_s$	$k_w$	$k_d$	$\alpha$
Array, Center	$3.0\mu\text{m}$	$0.8\mu\text{m}$	0.05	0.70	1	1
Array, Edge	$3.0\mu\text{m}$	$0.8\mu\text{m}$	0.05	0.70	1	1
Single NW, InAs segments	$3.0\mu\text{m}$	$0.6\mu\text{m}$	0.05	0.65	1	0.5
Single NW, InGaAs segments	$1.8\mu\text{m}$	$0.6\mu\text{m}$	0.05	0.65	1	0.5

**Table 4.1:** Diffusion parameters used for graphs in Figs. 4.5 and heterostructured NWs as presented in Ref. [II]. All parameters are found for at growth temperature of 425 °C and bulk equivalent growth rates of 500 nm/hr and 300 nm/hr for In and Ga, respectively.

Using the listed parameters we have investigated the importance of the contributions to the GR for adatoms from the substrate, sidewalls and droplet, as shown in Fig. 4.6. For short NWs the main contribution comes from substrate diffusion and for NWs with a length exceeding 700 nm, the sidewall diffusion gives the largest contribution to the GR. The contribution from the direct impingement on the droplet only plays a secondary role for all lengths. The impact of  $k_d$ , which we have defined to unity in the modelling, is therefore only of minor importance for the analysis.

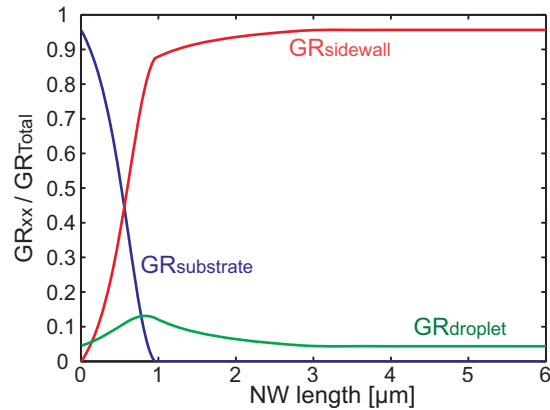


**Figure 4.6:** The contributions from adatoms impinging on the substrate, sidewalls and droplet as a function of NW length. The contribution from the substrate is the most important in the beginning of the growth and contribution from the sidewalls when the length exceeds 700 nm. The direct impingement on the droplet is at no times found to be the most important parameter.

The effective NW sidewall diffusion length of  $\lambda_w = 3.0 \mu\text{m}$  is a factor of 2 higher than reported by other groups[26], but many other effects are taken into account in this study. The incorporation coefficients of  $k_s = 0.05$  and  $k_w = 0.70$ , are somewhat different than reported in Ref. [31]. This can mainly be explained by the reduced contribution from the substrate and a limited diffusion on the sidewalls in our model. We would like to stress again the difference between diffusion lengths and incorporation factors and the need to take both into account. The diffusion lengths are mainly estimated from comparing NWs

(or lengths of InAs and InGaAs segments) to each other, whereas the incorporation factors are introduced to fit the lengths to the experimental data.

To obtain independent growth where the morphology of the NWs is not affected by neighbours, a minimum pitch of  $1.6 \mu\text{m}$  is necessary to avoid the influence of shared substrate diffusion. When shadowing effects are also taken into account the minimum pitch for independent growth is  $2.0 \mu\text{m}$ .

The dynamics of NW growth is very complex as all growth parameters influence each other. The deduced values from the controlled growth experiments are important not only for the understanding of the NW growth mechanisms but also for optimizing growth experiments. The method can easily be applied to other growth conditions or other types of NWs grown in MBE systems.

### 4.3 Fault Free Nanowires

A systematic study by Thelander *et al* has shown that a mixture of WZ and ZB crystal structure has up to 2 orders of magnitude larger resistance resistivity than single-phase NWs[110], and a similar conclusion was reached by Schroer and Petta[111]. The effects of single stacking faults are still not investigated in details, but until then, it is highly desirable to work with NWs without any defects in large segments for high-quality transport measurements. An example is the realization of a Cooper pair splitter in a NW[112], which is the subject of a joint project called Source of Entangled Electrons in Nano Devices (SE2ND) supported by the EU FP7. Univ. of Copenhagen participates and is among other things responsible for fabricating fault free InAs NWs.

Defect free InAs NWs have been fabricated by several groups using both MBE[105, 40, 106] and MOCVD[98, 99, 100, 113]. A thorough review on crystal phase optimization can be found in Ref. [93].

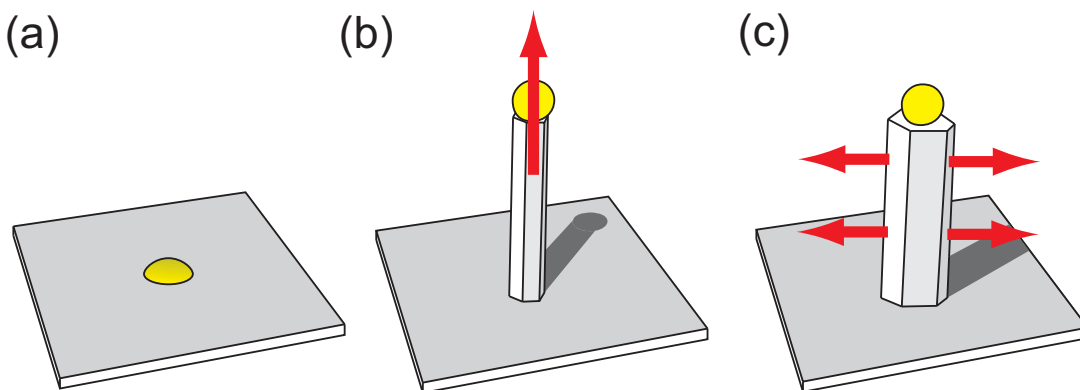


**Figure 4.7:** Two step growth method for synthesis of fault free InAs NWs. (a) 15-25 nm gold droplets are deposited on an InAs substrate. (b) NWs are grown for about 20 min to a length of around  $5 \mu\text{m}$ . (c) The axial growth is stopped by lowering the growth temperature and a radial growth is initiated, increasing the diameter of the NW.

### 4.3. FAULT FREE NANOWIRES

---

In this study, a two step growth method is used to achieve the high quality NWs as suggested by Shtrikman *et al*[105]. The two step growth method is depicted in Fig. 4.7, where first a thin Au film is deposited and annealed, giving droplets with a size of around 20 nm. Then axial NW growth is initiated giving NWs with a diameter similar to the deposited droplet, and finally the thin NWs are capped with a thicker InAs layer. Due to the high surface-to-volume ratio of the thin NWs, these form a pure WZ crystal structure. The growth in the second step adapts the crystal layer from the thin NW, and we achieve thick NWs with a pure WZ crystal structure. To initiate the growth of the capping layer, the growth temperature is dropped 100 °C, stopping the Au-assisted NW growth in the axial direction, and increasing the growth rate in the radial direction.

The NWs were analyzed following our normal protocol, first by SEM for investigating the outer morphology and then TEM for determination of the crystal structure. Detection of single SFs can be seen directly with high resolution TEM, where the individual atomic layers are resolved, see Fig. 4.8(c). HR TEM is a cumbersome and slow technique for analyzing a large batch of NWs and we therefore found another way of detecting SFs at a lower magnification. When tilted slightly off-axis the fault planes appear as dark lines in a bright field image, and could be resolved individually at a 58kx magnification, see Fig. 4.8(d). By collecting several images a full NW could be imaged with high enough resolution for detecting SFs, as shown in Fig. 4.8(e). A more practical approach was to find a single NW on the TEM grid, and then tilt the sample holder until a SF could be observed. As the NWs sometimes bend on the TEM grid, it was necessary to do the tilting and imaging at several positions on the same NW.

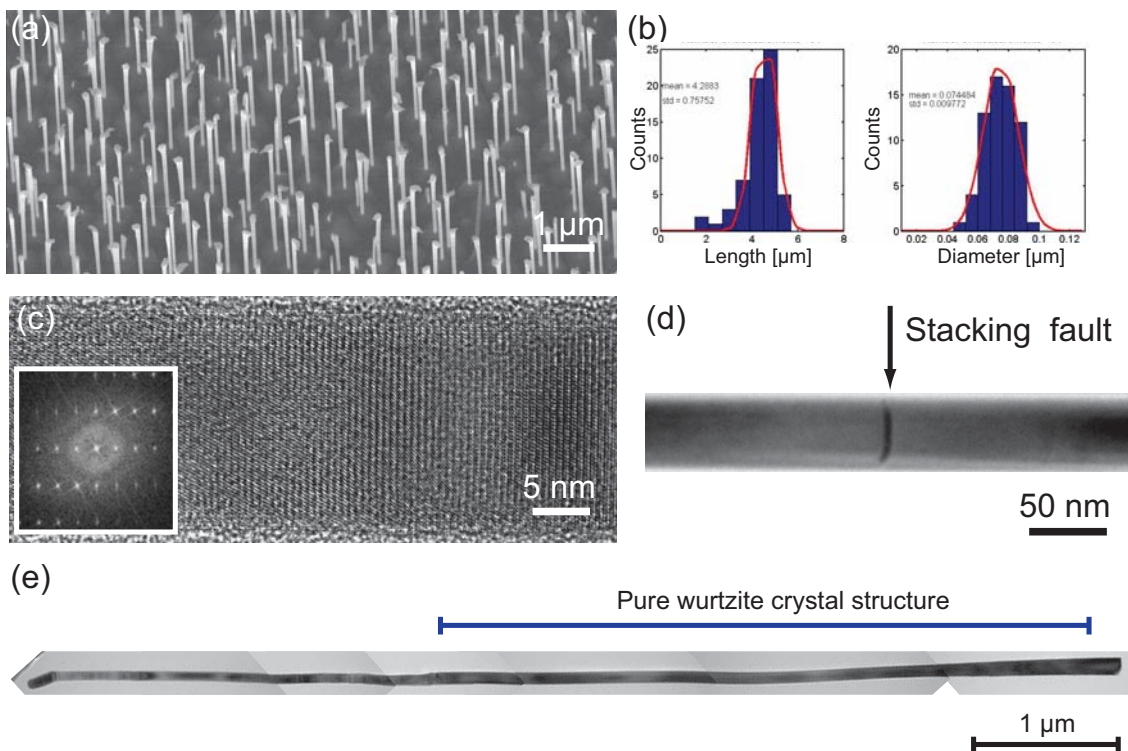


**Figure 4.8:** Electron microscopy analysis of InAs NWs grown using the two step growth method. (a) SEM image of NBI813 and (b) mean length and diameter of the shown NWs. (c) High resolution TEM image of an InAs NW before the shell growth. Inset shows the fast Fourier transform of the displayed crystal planes, and shows a pure WZ crystal structure. (d) Bright field TEM image tilted slightly away from the zone axis. The segment has one stacking fault. (e) Collected TEM images of a NW from the batch NBI828. The bottom part of the NW is completely free of stacking faults.

#### 4.4. TRANSPORT PROPERTIES OF AU-DOPED GAAS

Long segments of up to 4  $\mu\text{m}$  without any SFs were synthesized using the two step growth process. As a general trend the bottom half of the NWs have pure WZ structure and a few SFs are present in the top half. The tip of the NWs is easily recognized by the gold cap, as can be seen in Fig. 4.8(a), and ensures that the NWs can be contacted electrically by lithography in the fault free section. Selected growths are listed in Tab. 4.2, showing that typical NW lengths are 5  $\mu\text{m}$  and the diameters have been tuned between 20 and 90 nm, while wires up to 200-300 nm would be within the possible range. Another method for growth of defect free NWs has been shown by Shtrikman *et al*, where (011) substrates are used[40]. The wires still grow in the [111] direction and are therefore tilted with respect to the substrate. Apparently these growth conditions with increased flux on the NW sidewalls are ideal for obtaining defect free crystals.

Growth batch	Special growth	Length	Diameter	Crystal defects
NBI 652	Only core growth	$1.7 \pm 0.7 \mu\text{m}$	$21 \pm 3 \text{ nm}$	SF free
NBI 813		$4.3 \pm 0.8 \mu\text{m}$	$74 \pm 10 \text{ nm}$	<1 SF/ $\mu\text{m}$ in bottom part
NBI 814		$3.4 \pm 0.5 \mu\text{m}$	$72 \pm 8 \text{ nm}$	$\sim 1\text{-}2$ SF/ $\mu\text{m}$ in bottom part
NBI 823		$3.6 \pm 0.4 \mu\text{m}$	$60 \pm 9 \text{ nm}$	<1 SF/ $\mu\text{m}$ in bottom part
NBI 826		$5.0 \pm 0.7 \mu\text{m}$	$48 \pm 6 \text{ nm}$	$\sim 1\text{-}3$ SF/ $\mu\text{m}$ in bottom part
NBI 862		$5.9 \pm 0.7 \mu\text{m}$	$65 \pm 6 \text{ nm}$	<1 SF/ $\mu\text{m}$ in bottom part
NBI 828	p-doped (Be)	$3.8 \pm 0.6 \mu\text{m}$	$48 \pm 8 \text{ nm}$	<1 SF/ $\mu\text{m}$ in bottom part

**Table 4.2:** Growth of InAs NWs with long defect free segments.

## 4.4 Transport Properties of Au-doped GaAs

Au has been found to incorporate in NWs as discussed in Sec. 2.3 and influence the optoelectronic properties[45], though these results are still debated. We have investigated the influence of Au in bulk GaAs for transport measurements by applying Au during growth in the MBE system, which differs from previously studies, where Au have been applied after the growth[114]. A 3  $\mu\text{m}$  GaAs layer was grown on a GaAs(100) substrate with a rate of 1.0  $\mu\text{m/hr}$ , an intended Si doping concentration of  $10^{15} \text{ cm}^{-3}$  and a varying Au co-doping concentration. This type of growth is only possible in systems with an Au source inside the growth chamber. A series of growths with Au and Au-free reference samples were made, and are listed in Tab. 4.3. Si introduced as a dopant in GaAs substitutes a Ga atom, and supplies an extra electron per site, making the sample an *n*-type semiconductor. The gold flux at  $T_{\text{Au}} = 807 \text{ }^\circ\text{C}$  was from the vapor pressure estimated to be equivalent to the Si doping concentration.

This study was made in collaboration with Peter Krogstrup and Claus B. Sørensen, and with assistance to the low temperature measurements from Rune Hviid, Morten Hels, and Thomas Andersen.

Hall bars were fabricated using UV lithography for all the samples listed in Tab. 4.3 to determine the transport properties. A basic Hall bar configuration is shown in Fig. 4.9

Batch	$T_{\text{Growth}}$	Dopant		Measurements at 77 K			
		$T_{\text{Si}}$	$T_{\text{Au}}$	$\mu$ [ $\text{m}^2/\text{Vs}$ ]	$n$ [ $\text{m}^{-2}$ ]	$E_{dd}$ [meV]	$E_{sd}$ [meV]
NBI 607	580 °C	995 °C	none	$5.6 \cdot 10^4$	$2.1 \cdot 10^{15}$	12	2.5
NBI 608	580 °C	995 °C	none	$5.3 \cdot 10^4$	$2.1 \cdot 10^{15}$	-	2.5
NBI 624	580 °C	995 °C	807 °C	$5.6 \cdot 10^4$	$2.2 \cdot 10^{15}$	13	2.6
NBI 714	597 °C	995 °C	900 °C	$5.2 \cdot 10^4$	$2.6 \cdot 10^{15}$	11	2.9
NBI 721	580 °C	994 °C	none	$4.7 \cdot 10^4$	$1.3 \cdot 10^{15}$	17	3.1
NBI 722	580 °C	994 °C	900 °C	$4.0 \cdot 10^4$	$2.2 \cdot 10^{15}$	12	2.2

**Table 4.3:** Bulk Si-doped GaAs growths with Au-codoping for test of the influence of Au for the transport properties. Data for mobility  $\mu$ , carrier density  $n$ , and activation energy are found from Hall bar measurements.

where the current is running in the  $x$ -direction and a magnetic field  $B$  is applied perpendicular to the current in the  $z$ -direction. The longitudinal voltage drop,  $V_{xx}$ , is measured between the contacts  $V_1$  and  $V_3$ , and the Hall voltage,  $V_H$ , between  $V_1$  and  $V_2$ .

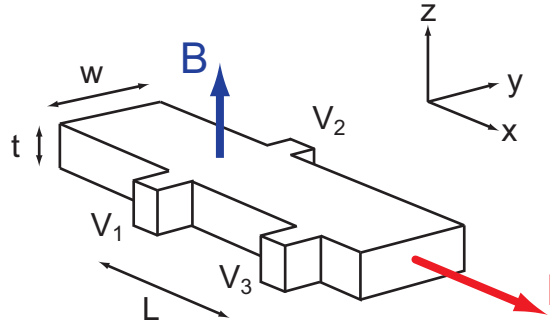


**Figure 4.9:** Sketch of a Hall bar. A current is running through the sample in the  $x$ -direction and a magnetic field is applied perpendicular to the sample, i.e. the  $z$ -direction. Voltages are measured between  $V_1/V_2$  and  $V_1/V_3$ .

In the framework of the Drude model, where the behavior of electrons in solids are treated classically, the carrier density  $n$  and mobility  $\mu$  can be calculated from the measured voltages[115]. In steady state, there is no net Lorentz force, i.e. the force arising from the magnetic field  $\vec{B}$  is balanced with that from the electric field  $\vec{E}$ ,

$$\vec{F}_L = -e(\vec{E} + \vec{v}_d \times \vec{B}) = 0, \quad (4.2)$$

where  $\vec{v}_d$  is the mean velocity (drift velocity) of the carriers[115]. As the magnetic field is applied perpendicular to the travel direction of the carriers, Eq. 4.2 reduces to  $E_y = v_x B_z$ . In a constant electric field the voltage drop is given by  $V_H = E_y w$ , where  $w$  is the width of the Hall bar as indicated in Fig. 4.9. The current density in the  $x$ -direction is given by  $J_x = -en v_x$ , and by also using that the current is given by  $I = J_x A$ , where the cross

section  $A = wt$  is introduced, one can find the Hall voltage,

$$V_H = -\frac{IB_z}{ent}. \quad (4.3)$$

It is evident that one can estimate the volume carrier density  $n$  from measuring the Hall voltage, if the current and thickness  $t$  of the Hall bar is known. For samples where the thickness is not known, one can use the area carrier density instead:  $n_s = nt$ . Similarly one can calculate the square resistance instead of resistivity  $\rho$ , given by  $R_s = \rho/t$ . The resistivity or square resistance can be calculated from measuring the voltage drop along the Hall bar,  $V_{xx}$ , and using the dimensions of the Hall bar. Using the Drude model the mobility can now be found by

$$\mu = \frac{1}{\rho ne} = \frac{1}{R_s n_s e}. \quad (4.4)$$

The mobility characterizes how fast an electron (or hole) can travel through a semiconductor when an electric field is applied.

#### 4.4.1 Measurements of Transport Properties

The Hall bars are diced out and bonded to a 14-pin chip carrier at which two Hall bars can be bonded simultaneously. The devices were cooled in a closed cycle cryocooler with a base temperature of around 10 K and equipped with an electromagnet with a maximum field of 0.45 T. The data acquisition was controlled by a LabView program and a Keithley 705 switch matrix, making it possible to obtain all data with a single voltmeter (HP3478A). It took around 2 hours to complete one data series with cooling from room temperature to  $\sim 10$  K.

Data for mobility  $\mu$  and carrier density  $n$  found from Hall bar measurements can be found in Fig. 4.10. The solid lines in the figure are from the reference samples and the dashed lines indicate samples with Au co-doping. Values of  $\mu$  and  $n$  are also listed in Tab. 4.3 at 77 K, which is an often used reference temperature, as it is the boiling point of nitrogen.

The mobility is comparable for samples with and without Au co-doping, and the lower value of NBI722 is not enough to make unambiguous conclusions. When looking at the carrier density all samples with Au co-doping have a higher value at 77 K than samples without Au. The shape of the curve for NBI722 is slightly different, but it might be due to the fact that the scan was performed from 10 K and to room temperature, instead of the usual procedure of going the other way.

Other effects might play a role as well and make the comparison between the samples more difficult. After the first three growths the heating system to the Ga source was modified and a minor nitrogen leak was detected in the growth chamber. The leak or other contamination can be the explanation for the lower carrier density found for the Au-free sample NBI721.

For better visualization of the data we show an Arrhenius plot of  $\ln(n)$  versus  $1/T$  in Fig. 4.11. We can estimate the donor activation energies  $E_{xx}$  from the carrier densities by

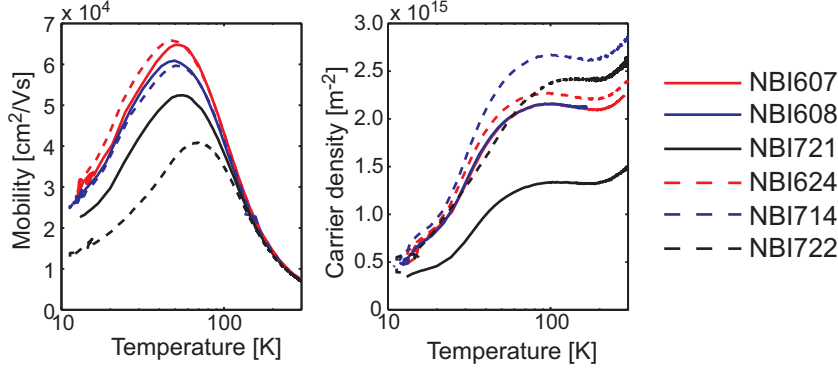


**Figure 4.10:** Hall bar measurements for bulk GaAs growths. Solid lines indicates Si doped growths and dashed lines indicates Si doped growths with Au co-doping. Growth details are summarized in Tab. 4.3.

fitting a function of the type

$$n \propto \exp\left(\frac{-E_{xx}}{k_b T}\right), \quad (4.5)$$

where  $k_b$  is the Boltzmann constant and  $E_{xx}$  is the activation energy for the specific regime. Three regimes are recognized, corresponding to the so-called deep donor ionization, saturation, and shallow donor ionization regimes. The shallow donor ionization regime is characterized by two different activation energies, which arise for a partially compensated semiconductor[116]. Three lines are fitted to the data using Eq. 4.5 to estimate the donor activation energies, with an example shown in Fig. 4.11. At temperatures in the range 300 K to 200 K five of the data series could be analyzed, and we found a mean value of  $E_{dd} = 13 \pm 2$  meV, where  $\pm$  denotes the standard deviation. Note that to obtain a more realistic value one should subtract the shallow donor concentration from the data first[117]. However, for this study where we are only interested in comparing growths to each other,  $E_{dd}$  can be compared directly.

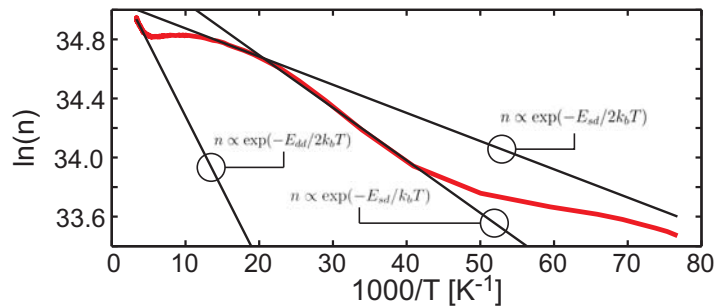


**Figure 4.11:** Arrhenius plot of the carrier density for estimation of activation energies for NBI721. Three activation energies have been estimated, one for a deep donor and two for a shallow donor in a compensated semiconductor. Fitting to functions of the type  $n \propto \exp(-E_{xx}/k_b T)$  gives  $E_{dd} = 17$  meV,  $E_{sd}/2 = 1.6$  meV, and  $E_{sd} = 3.1$  meV.

At lower temperatures, Fig. 4.11(b), two other exponential decreases in the carrier

density are observed. From fitting to the second ionization regime we find shallow donor activation energies to  $E_{sd} = 2.7 \pm 0.3$  meV ( $N=3$ ) and  $E_{sd} = 2.6 \pm 0.3$  meV ( $N=3$ ) for samples without and with Au co-doping, respectively. The estimated value of  $E_{sd}$  is smaller than the activation energy  $E_d = 5.8$  meV for Si as a shallow donor in GaAs[118]. Again, for this study only the comparison between growths with and without Au is of interest, and here we do not observe a significant difference. One can argue that this is a result in itself, but it would be desirable to have a growth with so much Au that there was no doubt about the effect.

It shall be mention that J.-C. Harmand presented a similar study at the PDI Workshop 2011, but to our knowledge this has not published. In the study they do not observe a significant effect of adding Au as a co-dopant to GaAs bulk growth until the surface roughness is considerably modified from the presence of Au. From secondary ion mass spectrometry measurements they also found an increased amount of Au at the surface and interface to the substrate, indicating that the diffusion of Au is significant.

In summary, we observe a small increase in the carrier density for Si-doped GaAs growth with Au co-doping. However, the variations are within the statistical uncertainties, and a more systematic study is necessary to get conclusive results. The amount of Au should be increased until a significant effect of Au as a co-dopant is observed and one should then be able to deduce the activation energy for Au in GaAs.

## 4.5 Summary

We have shown that using Au particles we can achieve good control of the growth of InAs NWs on InAs(111)B substrates by tuning the basic growth parameters. In a systematic study, the growth temperature and beam fluxes have been optimized to achieve the highest yield and NWs with minimal overgrowth. NWs have also been grown in large well-defined arrays using e-beam lithography and the observed height difference has been modeled using a mass continuity approach. The fitting parameters give experimental values for the effective diffusion lengths and incorporation factors of In adatoms. These value are confirmed in another experiment where periodic heterostructures are fabricated, and the same growth model used to fit the length of each segment.

NWs with a defect free crystal structure are grown using a two step growth method. A thin NW with WZ crystal structure is grown first and subsequently the growth conditions are changed to facilitate radial growth. The second growth step adapts the crystal structure of the core, and one can fabricate thick NWs with pure WZ structure.

Many devices based on the growth of Au-assisted InAs NWs presented in this chapter have been fabricated, ranging from transport devices to large scale vertical arrays for interfacing with mammalian cells. Some of these devices and associated measurements will be presented in the following chapters.



## Self-Assisted Nanowire Growth

In this section we will look at NW growth without a foreign metal particle to assist the growth. Within the last few years self-assisted NW growth of both GaAs and InAs on Si(111) has been reported for MBE directly on oxide[60, 65, 61, 62, 63, 68, 69][I,XII], from e-beam lithography defined holes in the oxide layer[66, 61, 119] and on bare substrates[67][I]. Self-assisted InAs NW growth on Si substrates by MOCVD has also been reported, see for instance Refs. [52, 54, 56]. Recently NW growth on few-layer graphene has been demonstrated for both self-assisted InAs[120] and GaAs[64], giving possibilities for new types of hybrid devices.

The advantage of omitting the gold is that one avoids contamination of both the MBE system and the individual NWs. Gold is known to be detrimental to the opto-electronic properties of semiconductors and an MBE dedicated for high electron mobility devices should therefore avoid it. Another advantage is that growth is conducted on silicon substrates, which are much cheaper than InAs substrates, and exotic sandwich structures, such as silicon-on-insulator (SOI) can be bought from large scale manufacturers.

### 5.1 Influence of the Oxide Layer

*This section is partly adapted from Ref. [I]*

The key parameters to control the NW morphology, length and width have been reported to be the temperature and the incoming fluxes, especially the V/III-ratio [59, 65, 61]. For self-assisted InAs NWs we have found it possible to obtain very different growths for the same growth parameters by changing the pre-treatment of the substrate. On the basis of our results using different pre-treatment techniques, we have found that the oxide layer thickness is a critical parameter for controlling the density and yield. In general, the NW growth can be divided into three different types of morphologies: (1) Growth on oxide; high density and many tilted NWs, (2) growth on a thin oxide layer ( $\sim 1$  nm); vertical and high aspect ratio NW growth (see Fig. 5.1(B,C)), and (3) growth without oxide; vertical NW

growth, with a low density and low aspect ratio and high probability of parasitic structures (Fig. 5.1A). We have in particular focused on the second regime, as it seems to be the most promising for growth of NWs.

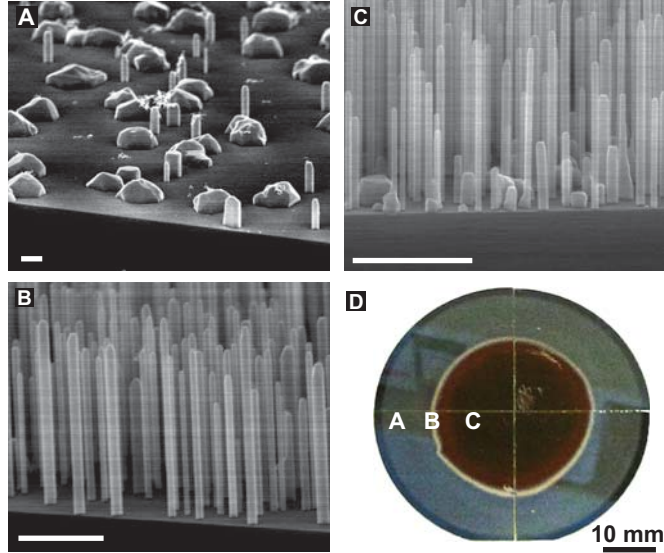


**Figure 5.1:** InAs NWs grown on Ga-assisted deoxidized substrate (described in Sec. 5.1.3). (A-C) Sideview scanning electron microscope (SEM) images of the three different wafer positions as marked in (D), corresponding to different oxide layer thicknesses. (D) is an optical image of a full 2 inch wafer where the oxide has only been removed in the outer part. Area A is an example of growth regime 3 and areas B and C are from growth regime 2, see text. The absence of parasitic bulk structures makes area B superior to area C. White scale bars are 1  $\mu\text{m}$ . Adapted from Ref. [I].

2 inch epi-ready undoped Si(111) substrates were pre-degassed at 500 °C before transfer to the growth chamber where they were degassed for 8 minutes at 630 °C immediately before growth. The temperature was then lowered to 460 °C, and the growth was initiated by opening the In-shutter. We used an In BEP of  $4 \cdot 10^{-8}$  torr, corresponding to a bulk InAs GR of 100 nm/hr. The As flux was turned on during the cool down from annealing to growth temperature unless otherwise stated. No pure In deposition was necessary to initialize growth, similar to the case of GaAs NW growth on Si(111)[XII].

Si substrates are covered by a native oxide layer consisting of  $\text{Si}_x\text{O}$ , where  $x$  is a number between 1 and 2. Using spectroscopic ellipsometry we have measured the oxide layer thicknesses to  $(14 \pm 1)$  Å for substrates taken directly from the box. This layer is a bit too thick for a good yield of vertical InAs NWs, and in this study we have controlled the thickness of the oxide layer using several different methods: (1) Regrowth of oxide, (2) Etching with HF, (3) Ga-assisted deoxidization, and (4) local etching in e-beam defined holes.

### 5.1.1 Regrowth of the Oxide Layer

One pre-processing approach is to remove the oxide layer completely by HF and then regrow the oxide layer. The latter was done by placing the substrate on a 200 °C hotplate in a fumehood. For non-treated substrates we observe growth of NWs in many different directions (Fig. 5.2D), defined as growth regime 1 above, and for growth on completely oxide free wafers, similar to Fig. 5.1A, only vertical NWs are observed (fig. 5.2C). No optimal conditions were found for growth on a re-grown oxide layer.

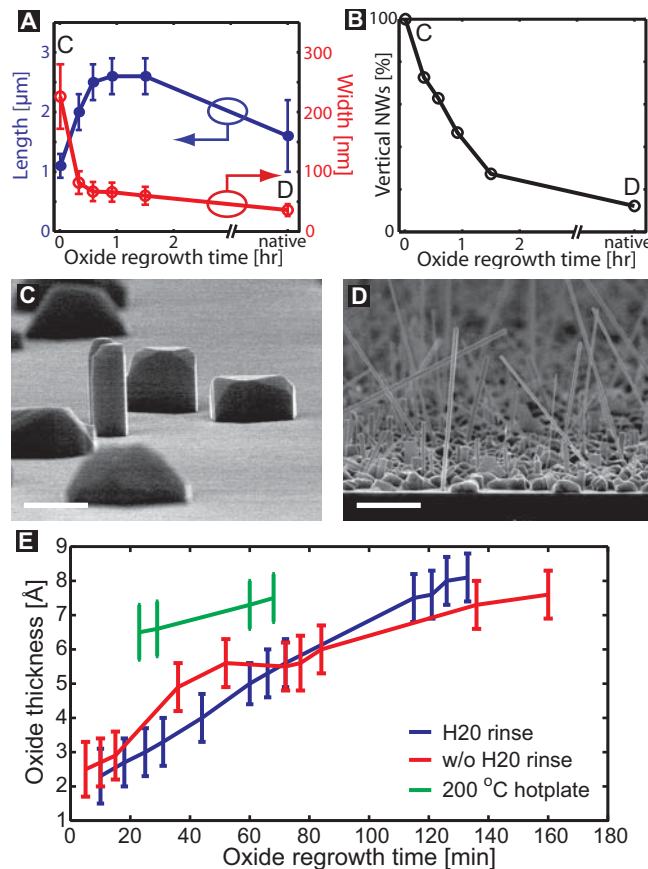


**Figure 5.2:** Regrowth of oxide on a 200 °C hotplate. (A) Length and width of InAs NWs as a function of regrowth time for the oxide layer. (B) Percentage of vertical NWs. The  $\text{As}_4$  flux is  $1.30 \cdot 10^{-5}$  torr, corresponding to a V/III-ratio of 320, and the growth time is 30 min. The point to the left marked with a C is without any re-oxidization treatment. A typical SEM image for this regime is shown in (C). (D) SEM image of growth on a native oxide layer marked with a D in the graphs. Scale bars are 1  $\mu\text{m}$ . (E) The regrowth of the oxide layer is measured with spectroscopic ellipsometry. Adapted from Ref. [1].

The thickness of the oxide layer as a function of regrowth time has been measured using spectroscopic ellipsometry, see Fig. 5.2(E). The oxide layer is stripped by dipping the substrate in 5% HF for 30 sec and then either transfer to the ellipsometer or place on a 200 °C hotplate. No difference is seen whether the substrate is rinsed with Millipore water for 15 sec after the HF etching or this step is omitted. As expected the re-growth of oxide

is faster when the substrate is placed on a hotplate.

### 5.1.2 Etching of the Oxide Layer

HF is effective for stripping the oxide, and it is possible to get a sharp gradient between the areas with and without oxide as previously shown in Fig. 2.8. In order to precisely control the oxide layer thickness we have conducted a series of experiments for finding the etch rates using both HF and buffered HF, which is 12 % HF diluted in ammonium fluoride. Buffered HF is often used for enhanced control of the etching process and it is less harmful to a resist layer when lithographically defined holes are etched out.

For measuring the etch rates, substrates with a 30 nm oxide layer were etched for 16 sec to 360 sec with different concentrations of HF and buffered HF. The etching was stopped by rinsing with Millipore water, blow dried with nitrogen and immediately transferred to the ellipsometer. Data are presented in Fig. 5.3 and the solid lines are linear fits to the data points. The slopes of the lines give the etch rates and these are indicated directly in the graphs. As a rule of thumb, the etch rate for  $\text{SiO}_x$  is found to be,

$$\text{Etch rate SiO}_x = 1 \text{ \AA/s} \cdot [\% \text{ HF conc.}], \quad (5.1)$$

where the concentration in percentage of the used HF solution is the last part of the expression. This relation is only valid for low concentrations (up to around 5 %) and in good agreement with previously published results[121].

It is difficult to exactly control the etch rate from time to time, and instead we made a gradient in the thickness of the oxide layer by slowly lowering a substrate only with native oxide on in a 1 % HF solution. An estimated oxide thickness varying from 5 Å to 14 Å was made, and the best growth of NWs were found at around 9 Å. This method ensured growth in a good regime every time, but made a systematic study of the other growth parameters rather meaningless, as identical pre-treatment conditions could not be reproduced every time.

### 5.1.3 Ga assisted deoxidization

A third method to remove the oxide without contaminating the substrate is Ga assisted deoxidization[122].  $\text{SiO}_2$  desorbs at temperatures around 900 °C depending on the composition and background pressure. Ga can react with the silicon oxide via the chemical reactions[123]



and the excess Si reacts further via



## 5.1. INFLUENCE OF THE OXIDE LAYER

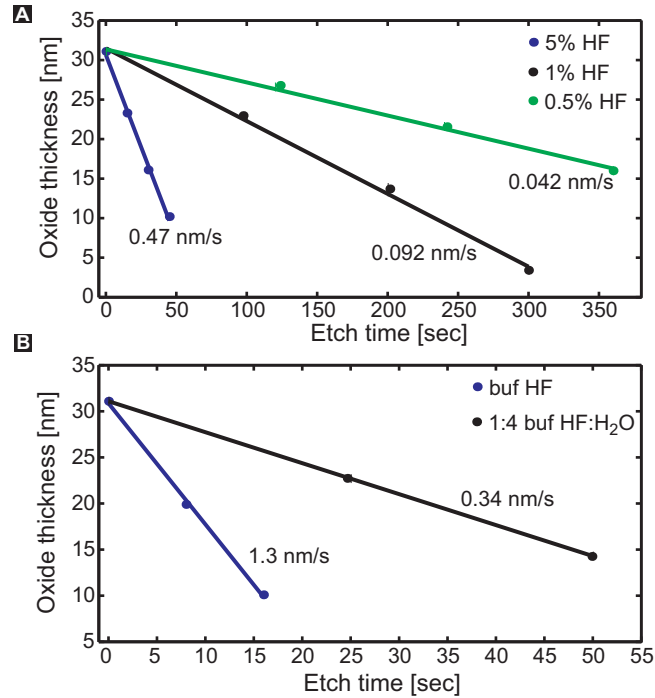


**Figure 5.3:** Etch rates for SiO<sub>x</sub> on silicon substrates at 20 ° using (a) HF and (b) buffered HF (12 %) diluted in ammonium fluoride. The etch rates are indicated in graphs and found as the slope of the linear fits made to the data points.

Both SiO and Ga<sub>2</sub>O desorbs at a much lower temperature than SiO<sub>2</sub>. From the stoichiometry we can expect to remove one SiO<sub>2</sub> pair for every two Ga atoms, and as the lattice spacings for SiO<sub>2</sub> and GaAs are almost identical, we can use the bulk growth rate for GaAs measured with RHEED to get an estimate of the evaporation rate.

Using ellipsometry we have measured the deoxidization rate. After unloading the sample from the MBE system, and exposing it to air, it was transferred immediately to the ellipsometer. We have corrected the data for the small amount of reoxidization in the transfer period. We find that the deoxidization rate is slightly larger than expected from the stoichiometric calculations, i.e. deposition of the amount of Ga to form a 2 nm GaAs bulk layer removes slightly more than 1 nm SiO<sub>2</sub>. This is close to the result by Wright and Kroemer who states that the deoxidization rate is slightly smaller than the stoichiometric amount[122]. The difference might be due to the native oxide layer consisting of both SiO and SiO<sub>2</sub> referred to as SiO<sub>x</sub>.

The Ga-assisted deoxidization reactions are very temperature sensitive around 800 °C[122]. By exploiting the substrate temperature gradient when growth is carried out without a backside diffuser plate (see details in Sec. 2.2.4) we were able to make a partial deoxidization. The oxide layer has only been removed in the hotter part of the substrate, recognized as the bright part of the optical image in fig. 5.1D. We used a Ga deposition rate equivalent to a bulk growth rate of GaAs of 300 nm/hr and a temperature of 820 °C, measured with a pyrometer. The Ga flux was on for 30 min and afterwards the substrate was kept at 820 °C

for 10 min to ensure that all Ga was re-evaporated. As control experiments we have raised the temperature to 840 °C, which completely deoxidizes the entire substrate. Subsequently heating of the substrate without applying Ga gives no measurable deoxidization.

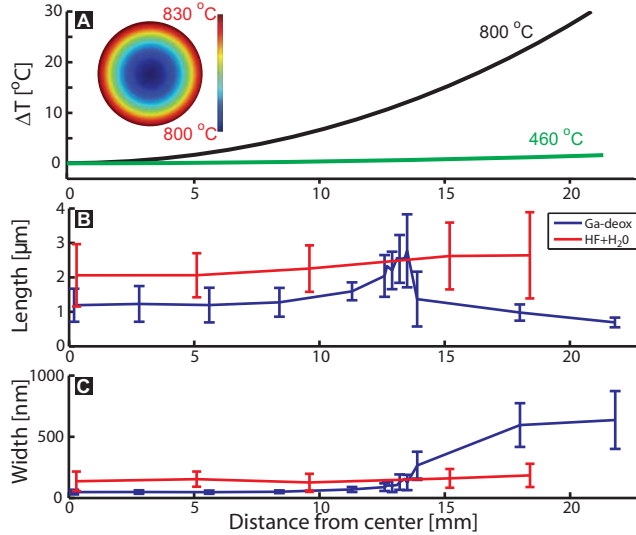


**Figure 5.4:** Temperature and NW morphology across 2-inch substrates. (A) Simulation of the temperature across a 2 inch Si substrate during Ga-deoxidization and growth, see details in Sec. 2.2.4. Inset shows the full wafer. (B,C) Morphology of NWs for two pre-treatment methods as a function of the radial distance from the center. The blue curve is data from the growth with Ga-assisted deoxidization shown in Fig. 5.1 and the red curve is a HF deoxidized substrate with similar growth conditions. The longest NWs grown on the Ga-assisted deoxidized substrate are observed to be at position B marked in Fig. 5.1. The growth time is 60 min and an  $\text{As}_4$  BEP of  $1.30 \cdot 10^{-5}$  torr, corresponding to a V/III-ratio of 320 has been used for both substrates. Adapted from Ref. [I].

For similar growth conditions, the Ga-assisted deoxidization and the regrowth of oxide for a very short time are compared in Fig. 5.4(B,C). The blue curve is for the same growth as shown in fig. 5.1 where the Ga-deoxidization method is used, whereas the red curve is for a substrate dipped in 5% HF for 10 sec and rinsed with Millipore water ( $>18 \text{ M}\Omega$  resistance) for one minute, which forms a thin oxide layer. The average width and height of the NWs are plotted in Fig. 5.4(B,C) as a function of the radial distance from the center of the wafer. It shall be emphasized that the temperature gradient in Fig. 5.4(A) only applies for the Ga-deoxidized substrate during the deoxidization process. At the growth temperature (green curve) the temperature gradient is only a few degrees. All NWs for both pre-treatment methods are observed to grow perpendicular to the substrate and therefore belonging to either regime 2 for a thin oxide layer or regime 3 in areas where the oxide has been completely removed.

The width and length distributions of the NWs are highly uniform across the HF etched substrate, whereas for Ga-assisted deoxidized substrates it completely changes around 13 mm from the center. This area is recognized as the bright band in Fig. 5.1(D). In this band, the length and width distributions of the NWs are similar to the ones from the HF etched substrate *and* no parasitic bulk structures in between the NWs are found, see

Fig. 5.1(B). This growth regime is therefore of paramount interest for self-assisted InAs NWs. The results above are the first report of parasitic island free growth of self-assisted NWs on non pre-patterned substrates.

The large variation of the lengths and widths within the same area, represented by the error bars, may be explained by the formation of non-uniform openings in the oxide film. Mandl *et al.* has measured openings in a  $\text{SiO}_x$  layer on InAs(111)B ranging from less than hundred nm to several micrometers[70]. In the oxide free areas the morphology of the NWs are very different, and a low density of thick and short NWs are found. This clearly shows that the oxide layer plays a major role for self-assisted NW growth.

### 5.1.4 Selective Area Growth

A more promising way for obtaining consisting growths is by using the selective area growth method, where holes in an oxide layer are etched out, as described in Sec. 2.4.2 and shown in Fig. 5.5.

Holes with a diameter ranging from 20 nm to 400 nm were etched out in 30 nm thermal oxide on Si(111) substrates using e-beam lithography. We have experimented with both wet and dry etching, but actually achieved the best results with wet etching, reaching a yield of  $> 85\%$  consistently. Dry etching has in other studies been used as the preferred method of fabrication[66]. A critical step when using reactive ion etching (RIE) is to stop before reaching the Si surface, and then remove the last few nm oxide immediately prior to growth. For wet etching with buffered HF the etching time does not seem as critical and 25 sec gave consistent results. For holes up to around 200 nm in diameter, only a single NW is found in each hole, but for larger hole diameters multiple NWs are found. Generally a hole diameter of 150 nm to 200 nm was used and we did not observe an abrupt decrease in the yield with respect to hole diameter as reported in Ref. [71]. The different behaviour can be explained by other growth parameters and the intrinsic differences between MBE and MOCVD systems.

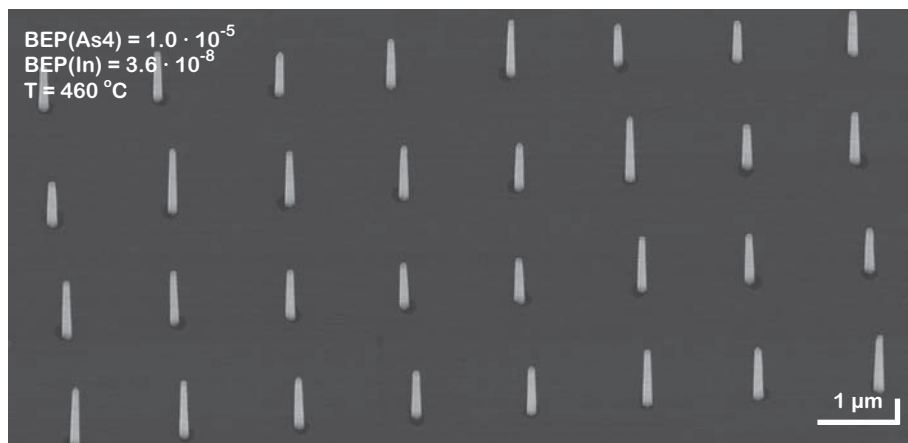


**Figure 5.5:** Array of self-assisted InAs NWs on Si(111). E-beam lithography defined holes are etched in a 30 nm oxide layer and allows for a selective area growth.

Growth conditions were kept constant at an In bulk equivalent growth rate of 100 nm/hr, a high As flux of around  $1 \cdot 10^{-5}$  torr and a growth temperature of 460 °C. These growth parameters have also been tested in the MBE system at the SPring8 synchrotron with success. Again, when keeping these parameters, the single most important step is the pre-treatment of the substrate. A 5 min plasma cleaning and a dip in 1 % HF for 60 sec just before loading the substrates, cleaning the holes for any residues and stripping the remaining oxide, considerably improved the yield.

The main scope of applying the method for self-assisted NWs was for easier and cheaper device fabrication, with further details in Sec. 6.3. After a set of acceptable growth parameters were found, no effort was put into optimizing these further. When using new substrates or growths at other MBE systems, we only focused on optimizing the growth temperature and kept the beam fluxes constant. For growth of positioned NWs on a 30 nm thermal oxide layer, we found a fast method for finding the optimal growth temperature. At a temperature around 460 °C the sticking on the oxide layer drops drastically, which can sometimes even be observed in an optical microscope. A growth temperature just above the critical sticking temperature was found as a good choice for growth of self-assisted InAs NWs.

## 5.2 Growth Mechanism

One of the most debated subjects for self-assisted growth of InAs NWs is the presence of a droplet, that is, whether the growth mechanism is VLS or VS. Mandl *et al* suggest a VLS growth mechanism for MOCVD grown wires based on growth interruptions[70]. They can continue growth after an As interrupt when preserving the flow of the In precursor. On the other side Hertenberger *et al* report the absence of a liquid droplet based on *in-situ* RHEED measurements and *ex-situ* SEM studies[68]. A combined VLS/VS scheme is suggested by Dimakis *et al*, where the growth is initialized by a VLS mechanism and then changes to VS[67]. In this section we will describe new experiments to increase the insight in the fundamental growth mechanism.

### 5.2.1 Crystal Structure Analysis

The fastest and most direct method for analyzing the crystal structure is by TEM. The NWs are mechanically transferred to a TEM grid and one can image and obtain diffraction patterns for the same NW. For all analyzed self-assisted InAs NWs, with only a few exceptions which will be discussed in the next section, the crystal structure is extremely mixed and consists of small ZB, twinned ZB, and WZ segments. This can be seen from the large variations in intensity along the NW in BF TEM images(Fig. 5.6(a)) and from the streaky diffraction patterns(Fig. 5.6(b)). The streaks arise from the high density of twin interfaces, which are perpendicular to the wire growth direction. The twin interfaces produce streaks perpendicular to the interface planes and therefore parallel to the common (111) g-vectors.

## 5.2. GROWTH MECHANISM

With high resolution TEM one can image crystal planes directly and with HAADF-STEM it is also possible to use the intensity variations in the columns of atoms to distinguish elements, as can be seen in Fig. 5.6(c,d). As the difference in atomic number between In ( $Z = 49$ ) and As ( $Z = 33$ ) is fairly large, one can by visual inspection conclude that the NWs are As-terminated during growth. The same has been found for GaAs NWs, though the task is more challenging here, as the atomic number for Ga ( $Z = 31$ ) is almost identical to that of As[124].

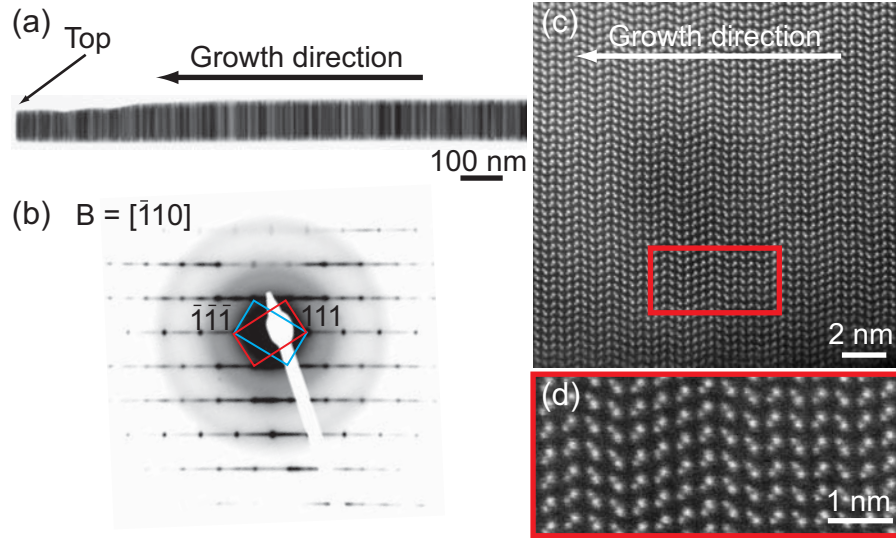


**Figure 5.6:** Crystal structure analysis of self-assisted InAs NWs on Si(111). (a) TEM image of top part of NW, where the tip is seen to be very flat. The intensity fringes come from variation in the crystal structure. (b) Typical selective area diffraction image in the  $[\bar{1}10]$  direction. Both the ZB and twinned ZB patterns are visible and the high density of twin interfaces gives rise to streaks parallel to the common (111) g-vector. (c,d) HAADF-STEM image where the individual columns of atoms can be resolved. From the insert it can clearly be seen that the growth is As-terminated during growth. HAADF-STEM images are obtained by Erik Johnson, NBI at NCEM, Berkeley Nat. Lab.

The morphology of the droplet is known to influence the crystal structure formation[17, 22], and the tendency to random layer stacking with a high density of planar defects therefore suggests the absence of a droplet. A similar random layer stacking has also been reported for GaAs NWs grown in a regime favouring VS[125], which supports the argument that self-assisted InAs NWs grow via a VS mechanism.

A combinatorial approach has been used by Johansson *et al* to calculate the polytype formation probabilities[126]. They have found all possible stacking sequences for six layers starting with an A layer and identify them as polytypes, e.g., the ABABAB sequence gives the 2H polytype (WZ), the ABCABC sequence gives the 3C polytype (ZB), and ABABAC gives a hexagonal polytype with stacking faults referred to as 2Hs. The probability for each stacking sequence is calculated using the formation probability factors  $p_c$  and  $p_h$  for cubic and hexagonal nucleation, respectively. One should note that  $p_c = 1 - p_h$  and that the formation probability can be calculated for all the polytypes, as shown in Fig. 5.7.

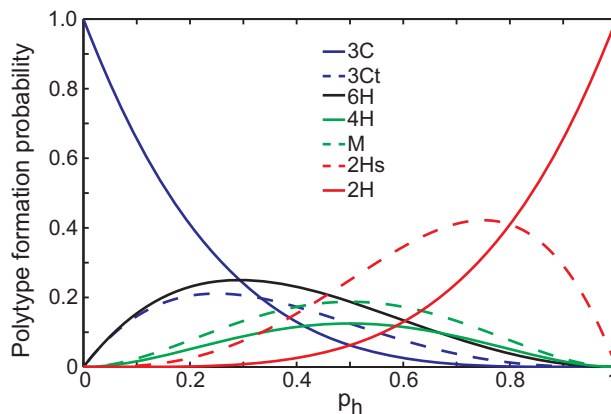


**Figure 5.7:** Formation probabilities for the most common polytypes in III-V NWs. Using a combinatorial approach for a crystal structure with six layers, the probability of all possible stacking sequences are found as a function of the probability of forming a hexagonal layer  $p_h$ . The different polytypes are: ZB (3C), ZB with twins (3Ct), periodic structures with hexagonalities of 33.3 % (6H) and 50 % (4H), a mixed phase with a hexagonality of 50 % (M), WZ (2H), and WZ with high density of stacking faults (2Hs). The figure is reproduced using the approach described in Ref. [126].

From Fig. 5.6(c) we find 23 hexagonal and 20 cubic stacking layers, giving that  $p_h \approx p_c \approx 0.50$ . Counterintuitively, when using the combinatorial approach this will give rise to a mainly WZ crystal structure with many stacking faults, and only small segments of ZB[126].

### 5.2.2 Formation of Droplets

So far no images of droplets have been reported for self-assisted InAs NWs, whereas they can be preserved after growth for self-assisted GaAs NWs[60]. By terminating the growth in different ways, we have been able to form a droplet on top of the NWs, which can be observed directly by SEM, as shown in Fig. 5.8. Five procedures have been investigated to terminate the growth and these are graphically illustrated in Fig. 5.8(a). The start of the growth termination procedure is defined to  $t_{\text{end}} = 0$  sec and up to then the growth is carried out as normal with a growth time of around 30 min. Hereafter is the growth termination modified as graphically shown in Fig. 5.8(a), where the green and blue bars indicate when the In and As fluxes are on, respectively. The red bars show the heater settings, as long as it is on, the temperature is maintained at 460 °C, and after it is turned off, the temperature drops rapidly. According to the thermocouple device the temperature is  $\sim 400$  °C after 1 min and  $\sim 300$  °C after 5 min.

When closing the In shutter at the same time as the heater is turned off, procedure I and II, no droplets are observed in the post growth analysis. If we instead keep the In flux during cooling down to at least 400 °C, In droplets are observed at the top, on the sidewall or at the bottom of each wire, as shown in Fig. 5.8(b,e). Only one droplet is observed at each NW, with the exception of very thick wires ( $>500$  nm) where multiple droplets are observed at the root of the wire. The observation with only a single droplet

## 5.2. GROWTH MECHANISM

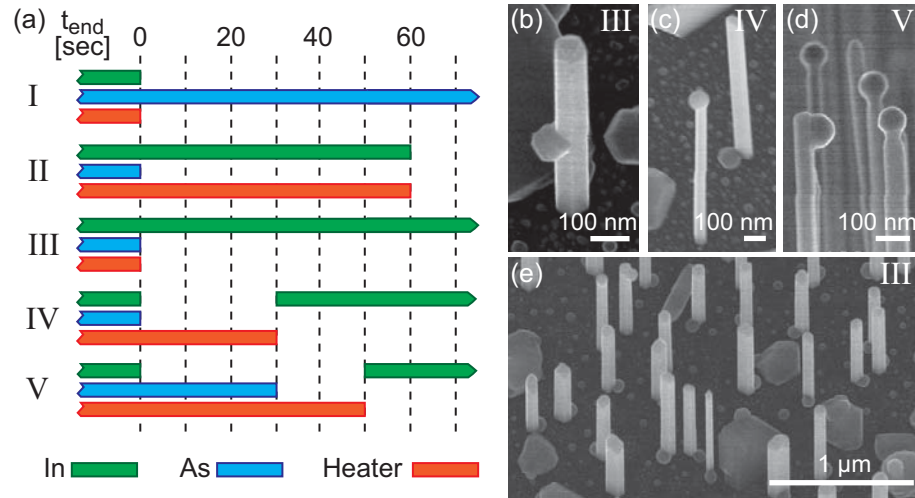


**Figure 5.8:** Procedures for termination of the growth. (a) Graphical illustration of five procedures for ending the growth with the time  $t_{\text{end}}$ . The bars indicate when the In, As and heater are turned on. (b-e) SEM images of InAs NWs where the droplets are preserved. Only one droplet is found at each NW, either at the tip, the sidewall or at the nanowire/substrate interface. (b) NBI 731 (c) NBI726 (d) NBI738, cross section (e) NBI726

at each NW, can be interpreted as the droplet is formed on the top of the NW and then slid down, instead of being formed directly at the bottom. The substrate temperature when the In flux is turned off relates to the number of droplets on top of the NWs. When In is turned off at  $\sim 300$  °C, more droplets stay on the top. At higher temperature they are often observed at the bottom of the NWs, and sometimes on the sidewall. We can therefore conclude that the critical parameter to maintain droplets on top of the NWs, is the substrate temperature when the In flux is turned off.

To determine whether the droplet is formed during cooling or is preserved from the growth, two control experiments were carried out. Procedure IV, where the In and As flux were turned off while the growth temperature was maintained for 30 sec after which the In shutter was opened again when the heater was turned off. And procedure V, the same as IV but with the inclusion of 30 sec gap with the As flux turned on. Both these termination procedures also gave large visible droplets on top, bottom or sidewalls of the NWs. It is unlikely that a droplet remaining from the growth can be preserved for 30 sec with a high As flux on. From these experiments we cannot conclude whether a droplet is present during growth or not, but we have observed that a droplet can be formed on top of the NWs after growth.

The elemental composition of the droplet was determined to consist of pure In using EDX in a TEM, as shown in Fig. 5.9. The NWs have the usual random stacking formation, but for some NWs a small segment of pure ZB is observed just below the droplet. As seen in Fig. 5.9 the morphology of the NW changes abruptly just before the small segment of pure ZB. We contribute the small ZB segment to growth after the As shutter has been closed and temperature started to drop, as an effect of liquid phase epitaxy with As supplied

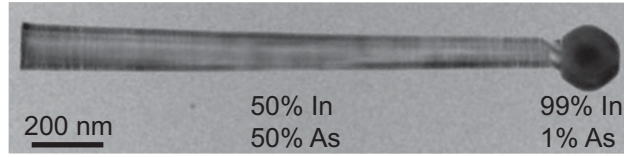


**Figure 5.9:** TEM image of an InAs NW (NBI720) fabricated using growth termination procedure III. The elemental compositions have been determined using EDX, where it is found the droplet is pure In.

from the background pressure. The indication that we can form a droplet and use this for controlling the crystal structure is an important observation and more experiments were carried out to enhance the control of the growths.

### 5.2.3 Growth Interruptions

A series of experiments with interruptions of the As flux was carried out to form a droplet and then continue growth. NWs with a large variation in diameter were fabricated on the same substrate by a local HF etch, and thereby only remove the oxide in a region on the substrate. The growth is initiated with an In flux equivalent to a bulk GR of 100 nm/hr for 15 min, then the In flux is ramped over 10 minutes to a  $GR_{In} = 300$  nm/hr and maintained for 1 min at the high flux before the growth interrupts. The As source was now closed for a period ranging from 15 sec to 120 sec while the In flux was maintained. Finally the growth was continued for 6 minutes with the high In flux. For all growths the substrate temperature was kept constant at 460 °C.

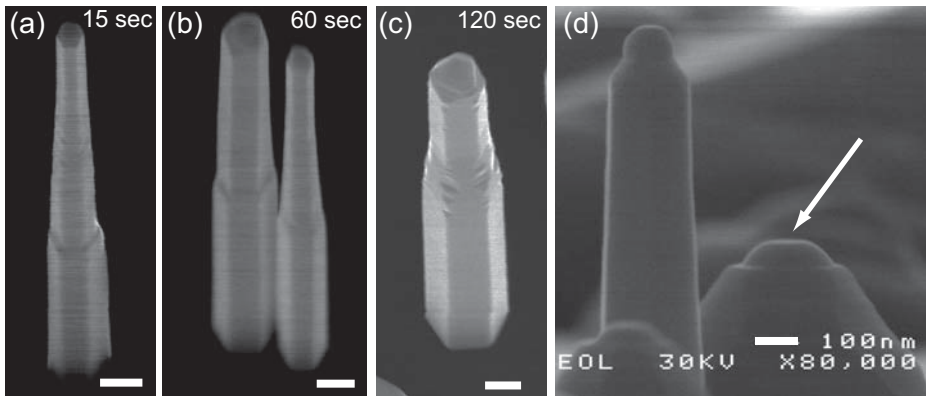


**Figure 5.10:** Effect of a growth interrupts for thick InAs NWs. (a-c) SEM images (tilting angle 15°) of InAs NWs grown on an oxide free substrate with interrupts of the As for 15 sec, 30 sec and 120 sec, respectively. (d) Side view SEM image of a growth where In has been maintained during cooling (procedure III). The arrow points to a droplet on a flat (111) facet and the edge of the droplet is clearly retracted from the edge of the thick NW. The average contact angle for droplet on (111) top facets is measured to  $\theta_c \approx 55^\circ$ , which is less than the average contact angle found for In droplets on a silicon substrate  $\theta_c \approx 70^\circ$  for otherwise identical conditions. Growth no. (a) NBI817, (b) NBI818, (c) NBI806, and (d) NBI720.

For thick NWs, mainly from growth on an oxide free substrate, most of the NWs have a shoulder, as can be seen in Fig. 5.10(a-c). The majority of the thick wires have the shoulder

## 5.2. GROWTH MECHANISM

morphology and the shoulder has only been observed for NWs with a growth interrupt. With reference to our study of growth termination methods, thick NWs following procedure III where the In flux is maintained during cooling down are investigated, as shown in Fig. 5.10(d). The shown NW has a flat (111) top facet and a droplet has been formed here, with its edge clearly retracted from the edge of the facet. This observation supports the idea that the shoulder is formed as a result of a liquid droplet formed during the growth interrupts. In other words, the growth is re-initiated in an In-rich VLS growth mode, and then changes to an As-rich VS growth. Such a growth scheme has been suggested by Dimakis *et al* for the initialization of the growth[67].

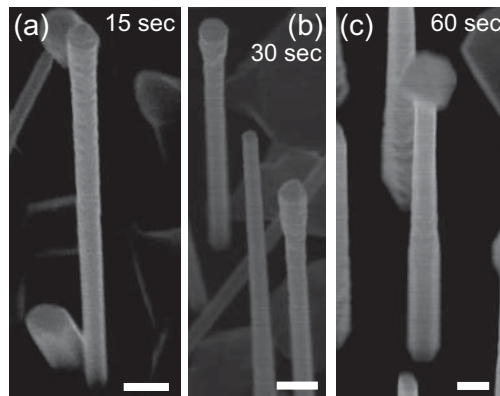


**Figure 5.11:** Effect of growth interrupts for thin InAs NWs. (a-c) SEM images (tilting angle  $15^\circ$ ) of InAs NWs grown on a thin  $\text{SiO}_x$  layer on a Si substrate with interrupts of the As for 15 sec, 30 sec and 60 sec, respectively. A few percent of the NWs are found to express reverse tapering. Growth no. (a) NBI817, (b) NBI796, and (c) NBI818.

Reverse tapering, where the diameter of the NWs increases towards the tip, has been reported for self-assisted growth of GaAs NWs[59]. It is explained by an increase in the droplet size when growing with a high group III flux. Very rarely we have also observed reverse tapering for self-assisted InAs by ramping the In flux during growth. The amount of NWs with reverse tapering could be increased significantly by interrupting the As flux for 15-60 sec, while only few were observed for 120 sec, while maintaining the In flux. The NW thickness also seems to influence the amount of NWs with reverse tapering and is mostly seen for thin NWs grown on a thin oxide layer, as shown in Fig. 5.11(a,b). For the 60 sec growth interrupt large structures too are found on top of the NWs, actually so large that they are out of focus in the SEM image in Fig. 5.11(c). Odd shaped structures have also been reported for InSb NWs under special growth conditions[109].

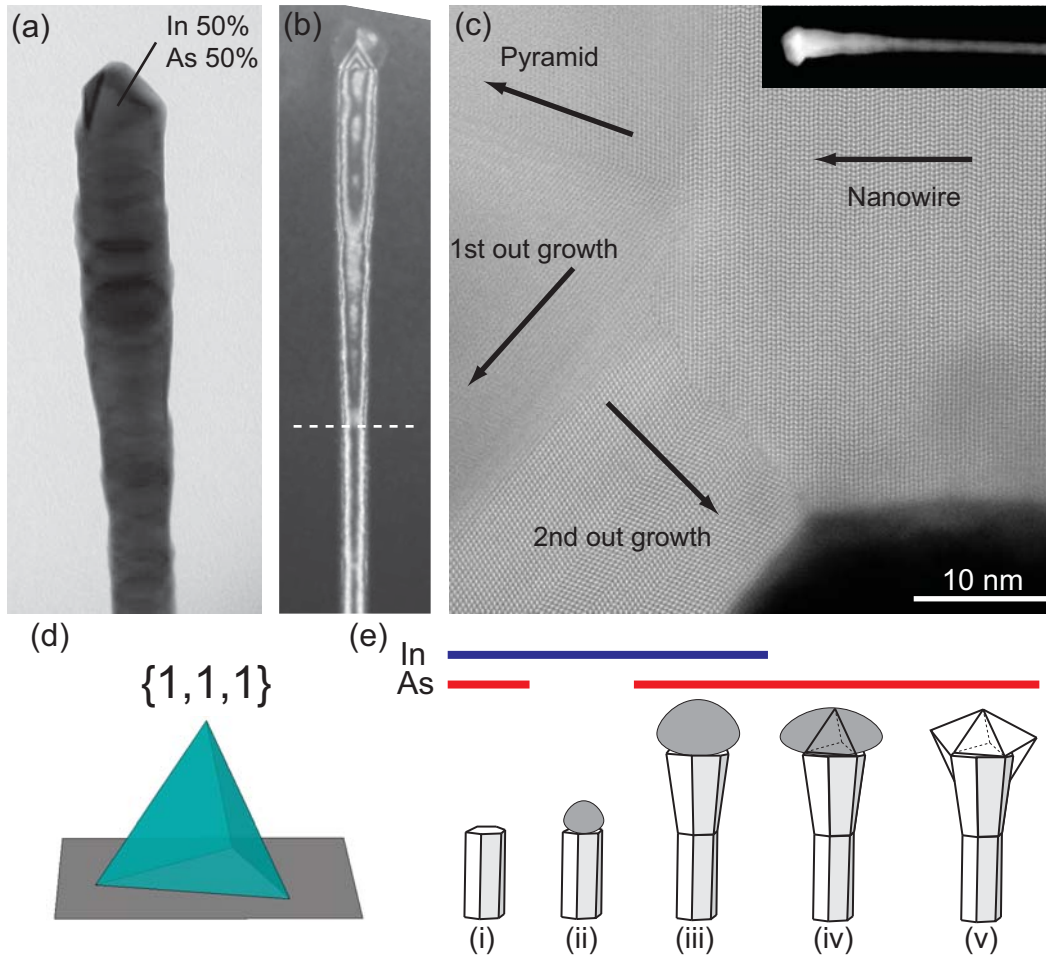


**Figure 5.12:** Structure analysis of InAs NWs with reverse tapering (NBI796). (a) BF TEM image where the pyramid is directly visible. The pyramid is found to consist of InAs from EDX analysis. (b) WBDF TEM image. The pyramid is covered with over growth, but can be seen in DF mode. The dashed line indicates where the tapering begins and a change in the thickness fringes is observed. (c) HAADF STEM image of a tip. The pyramid is found to have pure ZB crystal structure. From analysis of the polarity we can see that the growth direction changes and the growth takes place in several steps. Insert shows an overview image of the NW and the HR image is from the lower left corner of the NW. Image obtained by Erik Johnson, NBI, at NCEM, Berkeley Nat. Lab. (d) Wulff shape construction for low energy  $\{111\}$  facets using Wulffmaker software[127]. The angles of the structure are seen to match the observed ones. (e) Sketch of the evolution of tapered NWs with a pyramid on top. (i) VS growth where the  $GR_{In}$  is ramped from 100 nm/hr to 300 nm/hr over 10 min. (ii) As interrupt with a duration from 15-120 sec. (iii) Continuous growth with an expanding droplet, hence the reverse tapering. (iv) In turned off and temperature lowered. A ZB pyramid with In-terminated  $\{111\}$  facets are formed. (v) Several outgrowths from the droplet are formed during cool down.

The crystal structure of the reverse tapered NWs has been investigated using TEM and is shown in Fig. 5.12. All NWs which express reverse tapering have a tetrahedron on the top (a), but often this has been covered with overgrowth of InAs. In these cases the pyramid can very clearly be seen when changing to WBDF mode (b). With EDX it was confirmed that elemental composition of the pyramid and overgrowth structures consists of InAs. A more detailed analysis was carried out using HAADF STEM, where the individual columns of atoms can be resolved and the polarity can be used to determine the growth direction (c). The growth can be seen to take place in several steps, with first growth of the NW, then the pyramidal structure and finally two times overgrowth. The second overgrowth step is almost growing in the opposite direction as the original NW. When analyzing the crystal structure, it is confirmed that the NWs have the mixed crystal phases, but the pyramid is pure ZB. The outgrowths are also ZB but with few SFs.

The pyramids are found on all NWs with reverse tapering, but also on a few NWs without reverse tapering. We expect they are formed during the cooling of the substrate, as 3D nucleation becomes more favourable at lower temperatures, and 2D nucleation becomes less favourable[128]. The diffusion of In below the growth temperature is still significant and even at 0 °C In is found to form droplets. We therefore suggest that the pyramidal formation and overgrowth is formed at a temperature lower than 460 °C. A schematic of the pyramid formation is shown in Fig. 5.12(e).

The Wulff shapes for ZB crystals have been calculated using the winterbottom construction in the Wulffmaker software package[127]. NW growth is carried out in non-equilibrium conditions, so the calculations are not valid to describe actual growth, but can still be used to understand the observed structures. Three groups of facets ( $\{100\}$ ,  $\{110\}$ , and  $\{111\}$ ) are taken into the calculations, and equilibrium structures with only a single family of facets are found by setting the surface energy significant lower than the other facets, i.e.  $\frac{1}{2}\gamma_{\{111\}} = \gamma_{\{110\}} = \gamma_{\{100\}}$ . All three facet families forms pyramids as the equilibrium structure, but only  $\{111\}$  facets are seen to form a tall pyramid identical to the observed structures, see Fig. 5.12(d). The angles between two  $\{111\}$  planes are 19.47°[102], and they are In-terminated.

The evidence of 3D nucleation and the reverse tapered NWs indicates that a droplet can be present during growth. One should remember that only a minority of the NWs has reverse tapering and the presence of a droplet is therefore rather unusual. We still need to understand the mechanisms at the growth interface better, as the behaviour of stacking formation is different than for self-assisted GaAs NWs, where we have found a morphology change of the growth interface and long WZ segments when the Ga flux is changed[III]. It therefore seems possible that the morphology change of the growth interface is much smaller for self-assisted InAs NWs compared to GaAs NWs, which can explain the challenge it is to control the crystal structure.

### 5.2.4 Homoepitaxial Growth

As we have shown in the previous section NW growth can continue after an As interrupt, we tried to see if it was possible to initialize the growth directly on an InAs(111) surface, i.e.

homoepitaxial growth, which has so far only been demonstrated for selective area grown NWs using MOCVD[53]. InAs(111)B substrates were loaded and the growth temperature raised directly to 450 °C without a degassing step while an As backing pressure was applied to avoid desorption. The As was turned off and In supplied for 30 sec with a  $GR_{In} = 300$  nm/hr to form droplets. Hereafter the As source was reopened and growth continued for 20 min.

NWs were found at several locations on the substrate, usually within a circular area as shown in Fig. 5.13(a). A SEM image of one area with a high density of NWs is shown in Fig. 5.13(b), and some of the NWs have a length exceeding 2  $\mu\text{m}$ , but the length of most NWs is  $< 1$   $\mu\text{m}$ . It is still unclear whether the circular areas arise from the pre-processing (cleaving or cleaning) or from random accumulation of In during the As interrupt. A combination of the two schemes is possible, that is, some areas have an increased amount of impurities, and when In is deposited, it will be collected at these areas and facilitate the growth. The increased amount of In that might be necessary to initialize the growth again indicates that it follows a VLS growth mechanism in the beginning.

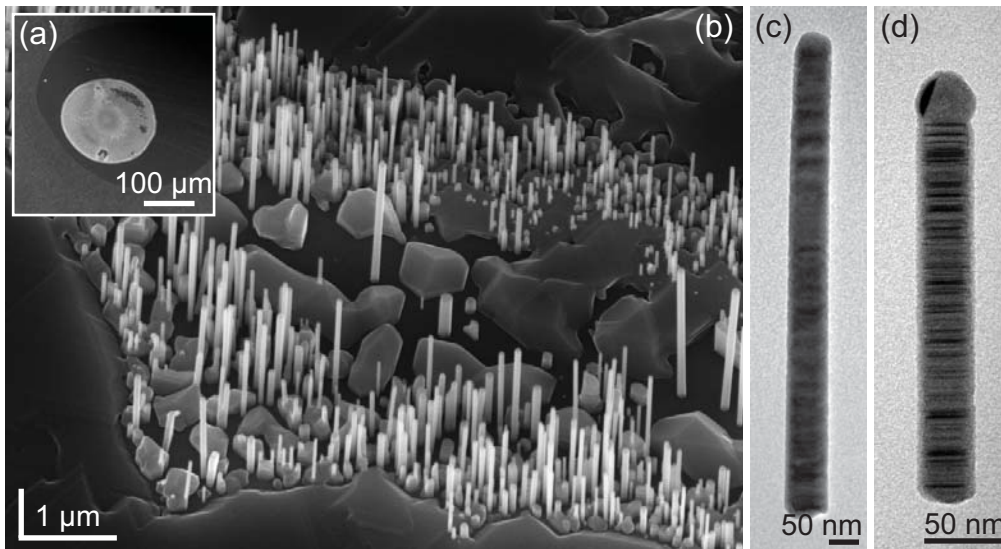


**Figure 5.13:** Self-assisted InAs NWs grown on an InAs(111)B substrate. (a) Low magnification SEM image of an area with NWs. A high density of NWs is found within the bright circular area. (b) SEM image (tilting angle 30°) of an area with high density of NWs. (c,d) TEM images with visible streaks from stacking faults in the crystal structure.

We succeeded in transferring a few NWs to a TEM grid for detailed analysis. As can be seen in the TEM images in Fig. 5.13(c,d), the NWs look like self-assisted InAs NWs grown on Si(111) substrates and streaks perpendicular to the growth direction indicate the presence of a mixed crystal structure. From this observation we can exclude the lattice mismatch when growing on silicon substrates as the primary reason for the random stacking sequences. NWs with a pyramidal structure as those presented in Sec. 5.2.3 are also found as shown in Fig. 5.13(d). The pyramid can only have been formed at the end of the growth and not at the growth interrupt, as no wires had been grown at this time. This

supports our description from last section where the pyramidal structures are expected to form during the cool down period.

#### 5.2.5 Conclusion

The growth mechanism of self-assisted InAs NWs is heavily debated and it is unclear whether it follows a VS, VLS or combined growth scheme. We have investigated this further by new experiments and shown for the first time that a droplet can be formed on top of the NWs, however this does not tell us whether a droplet is present during growth or not. Actually, a flat growth interface and the complete lack of control of the crystal structure might indicate that no droplet is present. We therefore conclude that the growth mainly following a VS mechanism, however, by introducing an As interrupt preceded we can continue growth in a VLS scheme. The new experiments show that a droplet can be formed and growth re-initiated even after a 2 min As interrupt. The exact growth mechanism is still not understood, as the growth behaviour is much different than for growth of self-assisted GaAs NWs.

### 5.3 *In-situ* Study with X-rays

*This section is partly adapted from Ref. [III]*

We have *in-situ* studied the crystal structure formation during self-assisted NW growth on Si(111) substrates in a combined MBE growth and x-ray characterization experiment at the beamline BL11XU at SPring-8 in Japan in collaboration with beamline scientist Masamitsu Takahashi and his group. With x-ray scattering one can determine the structure and shape of NWs[91, 129, 130, 131], and the advanced setup with a MBE chamber attached to the beamline makes time-lapse analysis possible. The combined growth and x-ray characterization experiment is superior to a study using RHEED because it is possible to monitor even small changes in the amount of a given crystal structure during the complete growth cycle.

The combination of two advanced experiments give some limitations for both the MBE system and the diffractometer. For instance, it is not possible to measure the direct beam fluxes before growth, and instead we had to rely on old calibrations relating the source temperature to a beam pressure. For the As source the total chamber pressure could be used, and the other sources could be calibrated using bulk equivalent growth rates measured with RHEED. The x-rays enter the vacuum chamber through beryllium windows. Beryllium can sustain high temperatures and it is almost invisible to x-rays, as it has a low atomic number. However, both the entrance and exit windows still give some diffuse scattering that is picked up by the CCD camera.

Before measurements could be initiated, the sample was aligned with respect to the Bragg reflections from the silicon substrate. As the lattice mismatch between silicon and GaAs (InAs) is 4 % (11 %) the Bragg reflections are easily distinguishable. After alignment

we had to keep the substrate temperature constant, as the crystal would move when the temperature was changed. Though, for some samples we were able to keep alignment in temperature spans larger than 100 °C, and typically we could change the temperature and then go back to the original level to re-do the alignment.

### 5.3.1 Wurtzite Formation In Self-Assisted GaAs Nanowires

In the first experiment we looked at crystal formation in self-assisted GaAs NWs grown directly on Si(111) substrates. A sketch of the setup is shown in Fig. 5.14 with a representative SEM image obtained in the post growth study. During most of the growth we monitored the intensity of the  $[10\bar{1}1]$  WZ Bragg peak. This peak is ideal for the experiment as the nearby  $[020]$  Bragg peak from the Si substrate is forbidden[129]. The WZ GaAs Bragg peak is expected alone to arise from NW growth, as bulk GaAs always exploits the ZB (or twinned ZB) crystal structure. Another advantage of the  $[10\bar{1}1]$  Bragg peak is that the  $[11\bar{1}]$  twinned ZB Bragg peak can be monitored simultaneously as seen on the CCD image in Fig. 5.14.

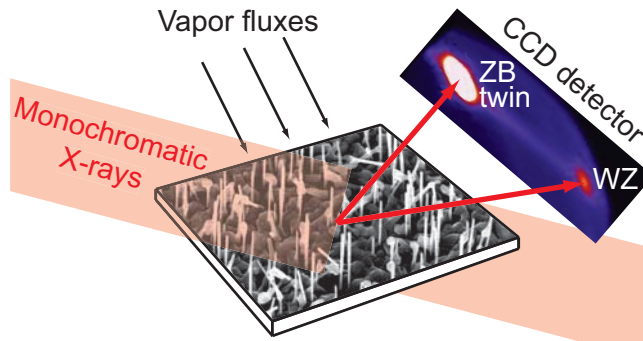


**Figure 5.14:** Sketch of the NW growth and *in-situ* x-ray characterization setup. The diffracted x-rays are detected with a CCD camera and a typical image from the camera is shown. The WZ crystal structure is only found in NWs whereas the twinned ZB is found in both NWs and bulk structures on the substrates. The SEM image is obtained in the post growth analysis of the sample. Adapted from Ref. [IV].

After alignment of the diffractometer, the growth was initiated by first adjusting the As beam pressure, and then open the Ga shutter. The CCD camera was used for capturing time lapse images with 1 sec acquisition time and approximately 2 sec read out time, and thereby obtaining around 20 images per minute. To prevent saturation of the detector Cu foil filters could be used for attenuation of the x-ray beam.

In the data analysis we integrated the intensity for an area around the WZ Bragg peak, and monitored the evolution of intensity with respect to the NW growth as seen in Fig. 5.15(a). To bring out the small features the differentiated intensity,  $dI_{WZ}/dt$ , is plotted in the same graph. The intensity,  $I_{WZ}$ , of the WZ Bragg peak is directly proportional to the total volume of the WZ crystal, and the change in intensity,  $dI_{WZ}/dt$ , is thus a direct measure of the growth rate. For clarity and to improve statistics 20 data points have been binned in the figure and the solid line is a guide to the eye. Also, shaded areas indicate

### 5.3. IN-SITU STUDY WITH X-RAYS

regions where the Ga flux is changed from a bulk equivalent growth rate of 100 nm/hr to 300 nm/hr or back.

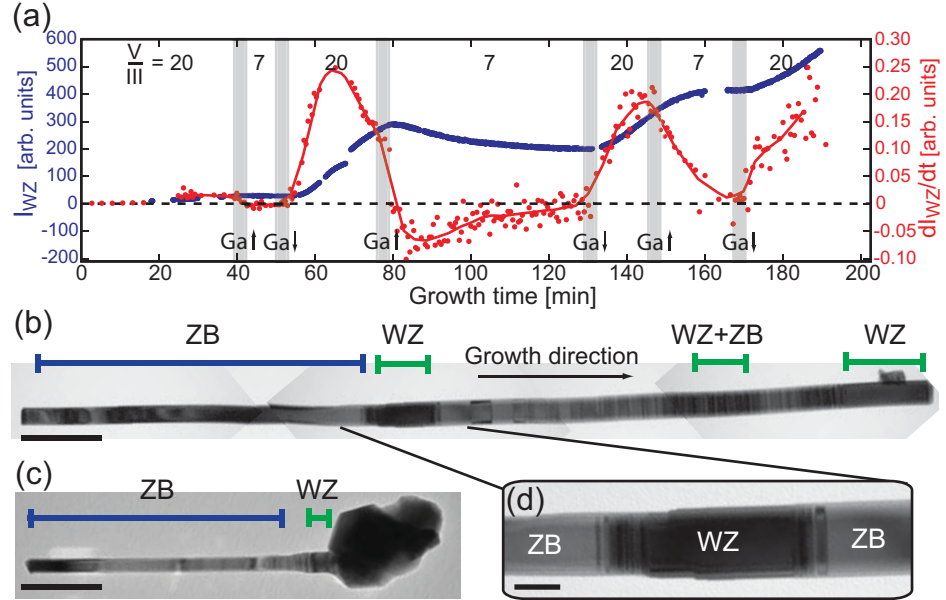


**Figure 5.15:** WZ crystal formation analysis of self-assisted GaAs NWs. (a) Total WZ crystal (blue points) and WZ growth rate (red points) of NWs by monitoring the  $[10\bar{1}1]$  Bragg peak. The solid line is a guide to the eye and the grey regions indicate periods where the Ga flux is changed between V/III ratios of 7 and 20. (b,c) TEM images of the two different types of NWs found in the post growth analysis. The crystal structure along the length was identified using convergent beam electron diffraction analysis. As seen in the straight wires (b) there are three sections with WZ structure, which correspond to the three regions of increased WZ formation in (a). In the wires which displayed a bulge formation, the WZ segment seen in (c) corresponds to the first segment in (b). However, these segments are either much shorter or even absent in the "bulged" wires due to a crystal phase transition from WZ to ZB. Scale bars are (b) 500 nm, (c) 500 nm, and (d) 100 nm. Adapted from Ref. [IV].

It is interesting to notice that the highest WZ growth rates are observed shortly after going from high to low Ga flux. To explain this, we suggest a morphological change of the droplet and the growth interface region, as the time scales for adatom kinetics and liquid diffusion become much smaller[132]. One should look at a full dynamic system where not only the V/III ratio is an important parameter, but also the morphology of the growth interface region at the given time.

Another interesting observation is the decreasing amount of WZ in the midsection of Fig. 5.15(a). The decrease in  $I_{WZ}$  can be explained by either desorption or a transformation of WZ into ZB, similar to the epitaxial burying observed by Ref. [133]. A desorption mechanism is difficult to explain during growth for the given conditions, and instead we suggest that a crystal phase transition takes place. This is confirmed from TEM images in the post growth analysis, where two types of NWs are observed: (A) straight NWs with three segments of WZ as shown in Fig. 5.15(b), and (B) NWs with a "bulge" formation at the tip and only one small (or none) WZ segment, see Fig. 5.15(c). The first part of the

two types of NWs is identical with a nearly fault free ZB segment of  $1.5 - 2 \mu\text{m}$ . Hereafter follows a segment of pure WZ and either continued growth (type A) or a large ZB crystal "bulge" formation (type B). From the x-ray scattering data, Fig. 5.15(a), the negative WZ growth rate is observed right after the first large WZ segment, exactly at the position where we find the "bulge" formation. This indicates that the "bulge" formation is responsible for the crystal phase transformation that has taken place during the low V/III growth period.

### 5.3.2 Crystal Structure of Self-assisted InAs Nanostructures

In a similar study the growth of self-assisted InAs NWs under presence of Sb was monitored, as Sb has been reported influence the crystal structure formation of NWs[134, 106]. To improve the experiment the NWs were grown on patterned substrates as described in Sec. 5.1.4, which ensures a much more uniform growth without parasitic bulk structures. A  $10 \text{ mm} \times 10 \text{ mm}$  area was prepared with  $300 \text{ nm}$  holes and a pitch of  $2 \mu\text{m}$  on Si(111) substrates.

The diffractometer was aligned as described above, but due to a mal-functioning In shutter, the growth was initiated by ramping the In source up quickly to a bulk equivalent growth rate of  $100 \text{ nm/hr}$  (beam flux  $\sim 1 \cdot 10^{-5} \text{ Pa}$ ). The evolution of the  $[10\bar{1}1]$  WZ Bragg peak was measured using a Pilatus detector, which has a much higher dynamic range and shorter read out time than the CCD camera used in the GaAs NW experiment. Like with the CCD camera it was possible to observe the tail of the twinned ZB peak in the same detector image, and we could thereby simultaneously obtain growth rates for WZ and ZB crystal formation, as shown in Fig. 5.16.

After around  $40 \text{ min}$  growth we started to introduce Sb to the growth, as indicated with vertical grey lines in Fig. 5.16. Even a very low beam flux of  $5 \cdot 10^{-8} \text{ torr}$  had an influence on the growth, and for increased amounts of Sb the growth rate of WZ decreases while the ZB growth rate is unchanged or shows a minor increase. It is interesting to notice that both the ZB and WZ growth rates increase significantly right after the Sb shutter is closed.

The post growth analysis, SEM image shown in the inset in Fig. 5.16(a), showed a low yield of NWs and instead positioned bulk structures at the openings in the oxide layer. The low yield can be explained by the defect shutter and with the In flux ramp, not enough In is accumulated in the holes at the start of the growth to facilitate NW growth[67].

The influence of Sb has been reported to change the crystal structure from WZ to ZB for Au-assisted GaAs NWs[134] and for InAs NWs[106]. In the study a complete change from pure WZ NWs for InAs to pure ZB NWs for an  $\text{InAs}_{0.88}\text{Sb}_{0.12}$  composition was found. Also self-assisted NWs are expected to express a similar change in crystal structure when introducing Sb[135]. A similar trend is observed in our data, even though the diffraction signal only comes partly from the NWs and mostly from the bulk structures, a clear change in the WZ formation rate is observed when Sb is introduced.

Not only is the WZ growth rate suppressed, also the ZB formation is slower, as seen from the large increase in growth rate right after the Sb is turned off again. Assuming that we still have group III mass conservation, i.e., no desorption of In adatoms, Sb seems

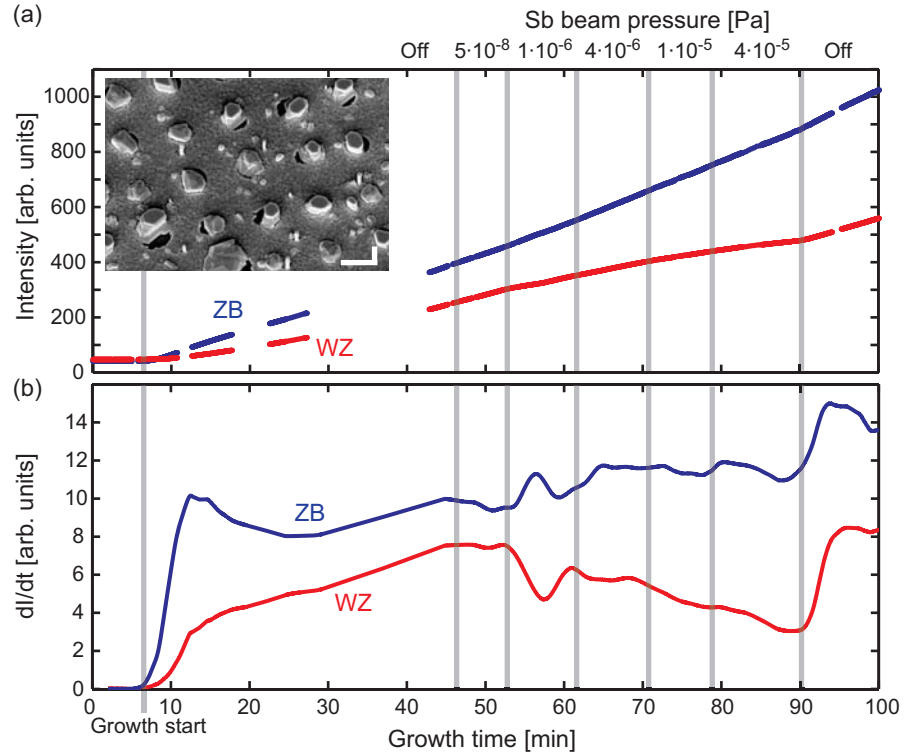


**Figure 5.16:** X-ray characterization of self-assisted InAs growth and the influence of Sb. (a) Intensities of the ZB (blue) and WZ (red) Bragg peaks. The first vertical line indicates the initialization of the growth and the other lines indicate changes in Sb beam pressure. The inset shows a SEM image of the growth. Scalebar is 1  $\mu\text{m}$ . (b) Growth rate of the ZB (blue) and WZ (red) crystals. Even a small amount of Sb is seen to have a large influence on the growth.

to facilitate growth on the oxide layer without epitaxial relationship to the substrate. The lower incorporation coefficient of In adatom when introducing Sb might be a key to better understanding of InSb growths and some of the strange reported effects related to it[109].

## 5.4 Summary

In this chapter we have looked at the growth of self-assisted InAs NWs. It has been demonstrated that enhanced control of the morphology can be gained by proper pre-treatment of the oxide layer on Si(111) substrates. The optimal layer thickness was found to be around 9  $\text{\AA}$  and several methods have been demonstrated to achieve this. Also, further control has been gained by selective area growth in e-beam defined areas.

The growth mechanism of the NWs has been investigated, and indications of both VLS and VS growth have been found. A combined growth mechanism, where the main growth section is in a VS regime is suggested. Several new observations have been reported, such as reverse tapering, pyramidal structures and self-assisted homoepitaxial growth.

We have shown that a MBE chamber attached to a synchrotron beamline offers a novel

and powerful tool for investigation of NW growth processes. The monitoring of the WZ growth rate was the easiest way to distinguish between the formation of parasitic bulk structures and NWs. From the formation rate of WZ crystal we suggest that a morphological change of the droplet and the growth interface region takes place, as the time scales for adatom kinetics and liquid diffusion is expected to give much faster changes, than those reported in this experiment. In the future we hope to continue the measurements on patterned substrates and eventually with a highly focused x-ray beam, making measurements on individual NWs possible.

## Biological Experiments

By combining the knowledge from different fields, new and interesting research areas evolve. In this chapter we will look at the merging of materials science with biochemistry and some of the unique possibilities and challenges associated with it.

Much effort has been put into using InAs NWs for intracellular probes through the CLIPS<sup>1</sup> project in collaboration with Karen Martinez's group, Department of Chemistry, Univ. of Copenhagen, who performed the biological experiments on the NW substrates.

Moreover, as part of my PhD program I spent 6 months at ORNL for an academic change of environment. At the group of T. McKnight I got directly involved in projects with interfacing VACNFs with cells, among other things for fast transfection and for capturing of cancer cells, as will be described in this chapter. With a background in physics, this was the first time I had to work with living objects, but a great experience to actually be able to keep them alive!

### 6.1 Nanowires for Biological Interface

Many different approaches are used for interfacing NWs with cells, with some of the most remarkable methods published by Charles Lieber's group at Harvard. Based on CVD synthesized group IV NWs, they have fabricated nano-sized field-effect transistors (FETs) suitable for intracellular measurements[9, 136].

NWs have also been used as optical probes for single cell endoscopy [137] by P. Yang's group, Berkeley. Using a micromanipulator a NW with an attached optical fibre is inserted into a single cell. By functionalizing the surface of the NW it is possible to simultaneously deliver drugs to the cell.

New methods for interfacing nano-sized structures with mammalian cells are reported all the time. Some interesting approaches including using single-walled carbon nanotubes[138] and ALD fabricated nanostraws[139] have been published within the last year. However,

---

<sup>1</sup>'Constructing Local Intracellular Probe Systems.' The project was funded by the Danish Strategic Research Council.

in the following sections we will beside NWs use VACNFs for interface to the cells, which were among the first techniques reported by McKnight *et al* around 10 years ago[12, 13].

We have used a method more suited for large scale production, where cells are suspended on InAs NWs still standing perpendicular to the substrate[7, 8][VI]. A similar approach has been utilized by other groups for other materials, for instance GaP[140] and Si[10, 11]. Examples of InAs NW arrays used for cell experiments are shown in Fig. 6.1, where the distributions of lengths and widths are shown below each array. A large homogeneity is found for NWs within the same field (around 5 mm  $\times$  5 mm) and a yield of nearly 100 % have been achieved on a full 2 inch substrate.

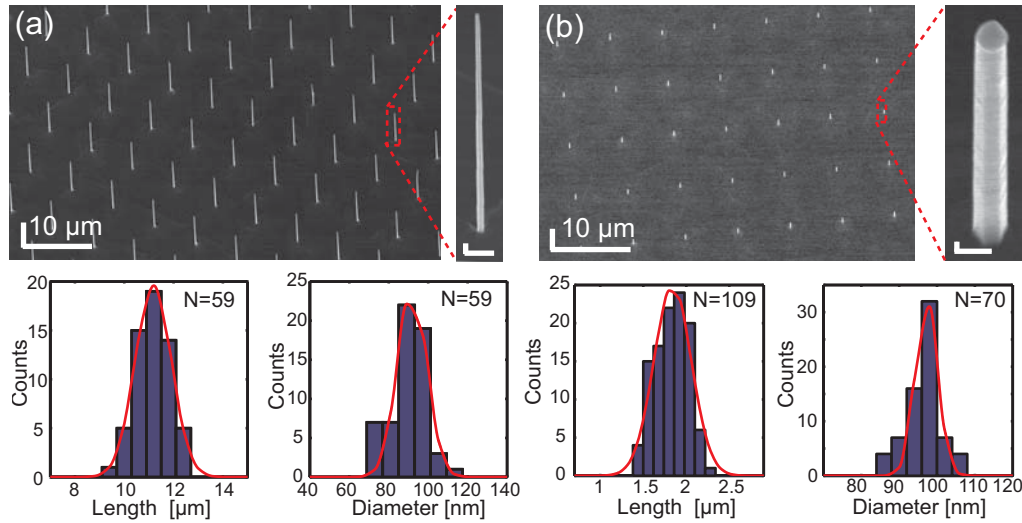


**Figure 6.1:** InAs NW arrays used for cell experiments. The NWs are found to be uniform in height and width when positioned using e-beam lithography. Scalebars of the zoom images are 500 nm (a), and 100 nm (b). Adapted from Ref. [VI].

Suspended HEK293 cells have been drop-wise added to sterilized InAs NW arrays and incubated for two days. By using fluorescence microscopy, the majority of the cells are found to still be alive after two days[8].

### 6.1.1 Cell Membrane Bending

As reported in Ref. [VI], though it by first sight clearly looks like the NWs penetrate the cell membrane (Fig. 6.2(a)) things become more complicated when one zooms in on individual NWs (Fig. 6.2(c)). Here the cell membrane bends around the NW forming a tent-like structure. The question is now whether there is intracellular access or not. It shall be noted that in order to obtain SEM images of the cells we first dry them using a critical point dryer and then evaporate a thin layer of Au. This process might influence the appearance of the cell, i.e. in Fig. 6.2(b) the cell is lifted from the substrate, and we do not know what the membrane bending would look like for living cells.

Instead we have used a technique with fluorescent labeling images using confocal microscopy for investigation of living cells. The cells were drop-wise applied to the NW array

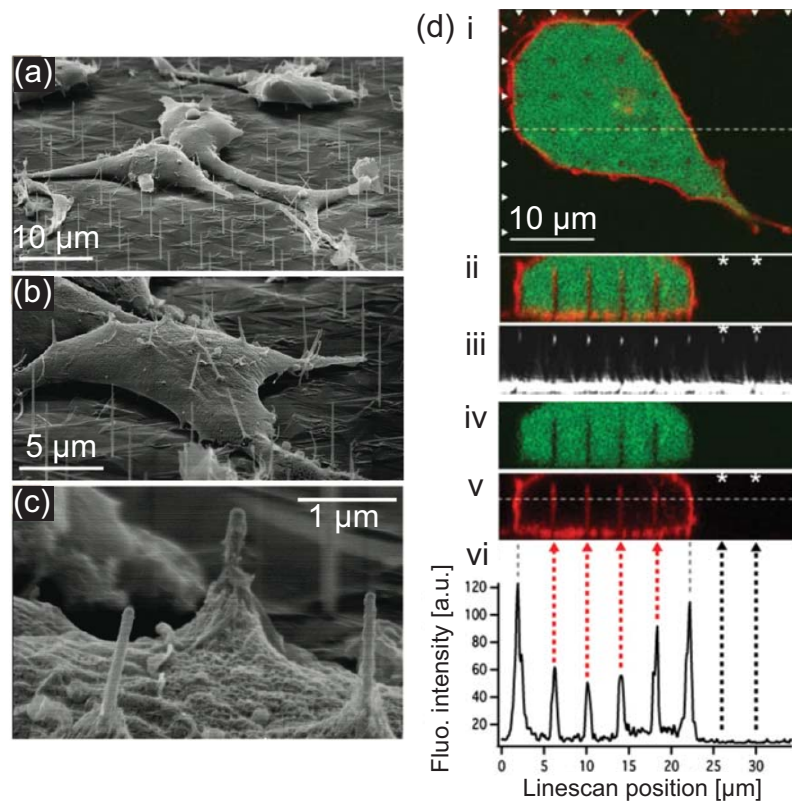


**Figure 6.2:** Cells interfaced with InAs NWs. (a-c) SEM images of HEK293 cells on a 7  $\mu\text{m}$  square lattice e-beam positioned array of NWs. The NWs are often clearly coated with the cell membrane as can be seen in (c). (d) Fluorescence confocal imaging for imaging of the cell membrane in living cells. (i) Top-view, the NWs are visible where the fluorescent cytosol have been excluded. (ii) Side-view, fluorescent imaging of both membrane and cytosol. (iii) Side-view reflection imaging. (iv) Fluorescent imaging of the cytosol. (v) Fluorescent imaging of the cell membrane. (vi) Linescan along the dotted line in (v) indicating that the cell membrane bends around the NWs. Imaging was performed by Trine Berthing and Sara Bonde and the figures are adapted from Ref. [VI].

and then allowed to settle for two days before the imaging experiments. The outer lipids of the cells were labelled with a membrane impermeable fluorophore which allowed imaging of the membrane. Cells were also labelled with calcein, which interacts with an enzyme in living cells, and can therefore be used to check the viability of them. Green fluorescence from the cytosol shows that the cells are alive.

An example of fluorescence confocal imaging is shown in Fig. 6.2(d) with both top-view and side-view of the same cell. The NWs can be visualized looking at the reflection from their Au-tip (iii) or indirectly as a dark region where the fluorescent cytosol have been excluded, (i) and (iv). The cell membrane is seen to wrap around the NWs in (v) and also in the line-scan (iv). NWs outside the cell (marked with asterisks) does not show signs of fluorescence, confirming that the fluorescence comes from the cell membrane.

This discovery of a very conformable cell membrane is a challenge for the intended experiments as sketched in Fig. 1.3, including effective drug delivery using NW array.

Methods to overcome this are available, where one of them is to literally stab the cells with the array of nanostructures, as will be discussed below.

## 6.2 Time-lapse Transfection Experiments

For successful delivery of genes to living cells one needs to bypass the cell membrane, either by diffusion or physical penetration. In this study, nanostructures are used for microinjection of plasmid using a technique called impalefection[13]. The name refers to a physical impalement of the cells and a transfection by modifying the surface of the nanostructures with plasmid.

The cells were cultured to obtain a homogeneous population and could be used for the impalefection experiment 1-2 times per week. Several cell lines were used for the experiments, and for all of them it was possible to deliver the plasmid directly into the cells. We look at the time it takes before the cells begin to express fluorescence after being impalefected. The first cells usually 'turn on' after about 1 hour, much faster than one would expect for a diffusion governed process.

### 6.2.1 Experimental Methods

Individual VACNFs with a pitch of 10  $\mu\text{m}$  are grown on a Si(100) substrate with Ni catalyst particles defined using e-beam lithography. After growth the fibers are protected with a SPR-220 (Shipley) resist layer, and diced out in  $2 \times 2 \text{ mm}^2$  pieces with a dicing saw. Just before the impalefection experiments, the resist is stripped using Microposit Remover 1165 (Shipley) and the chips are given a 30 sec plasma etch in a low pressure hydrogen atmosphere. These processes clean the pieces and modify the surface of the fibers with more functional groups, making them hydrophilic and thereby making it possible to attach plasmid to them. A solution with 100 ng of plasmid was put on each piece and dried in ambient air, typically within a few seconds. Two types of yellow fluorescent protein (YFP) reporter plasmids were used: pd2E and Venus. The Venus plasmid is expected to express fluorescence faster than pd2E[141].

The impalefection is executed by a stabbing method as sketched in Fig. 6.3. Cultured cells dispensed in 5 mL PBS solution are centrifuged (1000 rpm for 10 min, 60  $g$ ) into a pellet. The pellet is placed on a concave glass slide and a functionalized chip is pressed down on it using a pair of tweezers. The concave glass slide prevents the fibers from breaking during contact, as only the sides of the chip touch the glass slide.

The chips were then placed upside down in a 5 mL Petri dish, that had been prepared with a Gelrite layer for liquid diffusion of media. Lebowitz media was used to compensate for the fact that the cells were kept in atmospheric air during the imaging.

Within a few minutes after the impalefection, imaging was initiated using an inverted fluorescence microscope with a 10x objective and equipped with a CCD detector with a resolution of 1.92 MPx. A green-yellow filter cube was used for illumination and detection

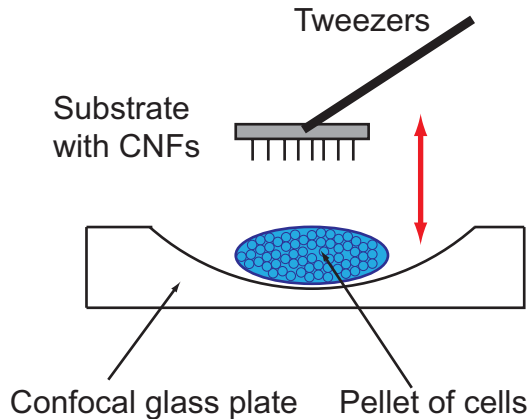


**Figure 6.3:** Sketch of the stabbing method for impalefection. Cells are centrifuged into a pellet and placed on a confocal glass slide. Small chips with VACNFs functionalized with plasmid are pressed down on the pellet using tweezers.

of the YFP expression, and time lapse images were typically acquired every minute for over 15 hours.

### 6.2.2 Macro for Intensity Analysis

The series of time-lapse images were analyzed using scripts written in Matlab and ImageJ. The fluorescence intensity of all cells (ranging from 10 to 200) in one experimental run could be analyzed simultaneously using the scripts. As a side note, it should be mentioned that the Matlab script was based on the code developed for the analysis of the time-resolved x-ray diffraction data (see Sec. 5.3). Sometimes the gap between different areas in physics is not as big as expected.

The protocol for analyzing the images follows a semi-automatic approach, where some parameters have to be adjusted manually to the given experiment and most of the analysis is automated. The first step is to find the position of all cells which express fluorescence. An image acquired after all the cells have started to express fluorescence and still not fading, typically  $\sim 300$  min, was loaded into ImageJ, see part of a full image in Fig. 6.4(a). The background was now removed by subtracting the first acquired image in time-lapse series from the image at  $t = 300$  min. The removal of the background was important to get a good signal-to-noise ratio (S/N), and also removed the effects from spots on the microscope lenses. A threshold value was now chosen 'by eye', such that all cells were included and only single pixels in the background. Hereafter could the 'Analyze Particles' command be used to find the position of the center of each cell. At the same time a new figure with all the cell outlines was generated, as shown in Fig. 6.4(b). The figure with outlines could be used later on to identify which cell we were looking at.

A list with positions of all the fluorescent cells was exported to Matlab. The background was removed by subtracting the first acquired image from all the other images. The total intensity within a region of interest (ROI) of  $25 \text{ px} \times 25 \text{ px}$  was now automatically found

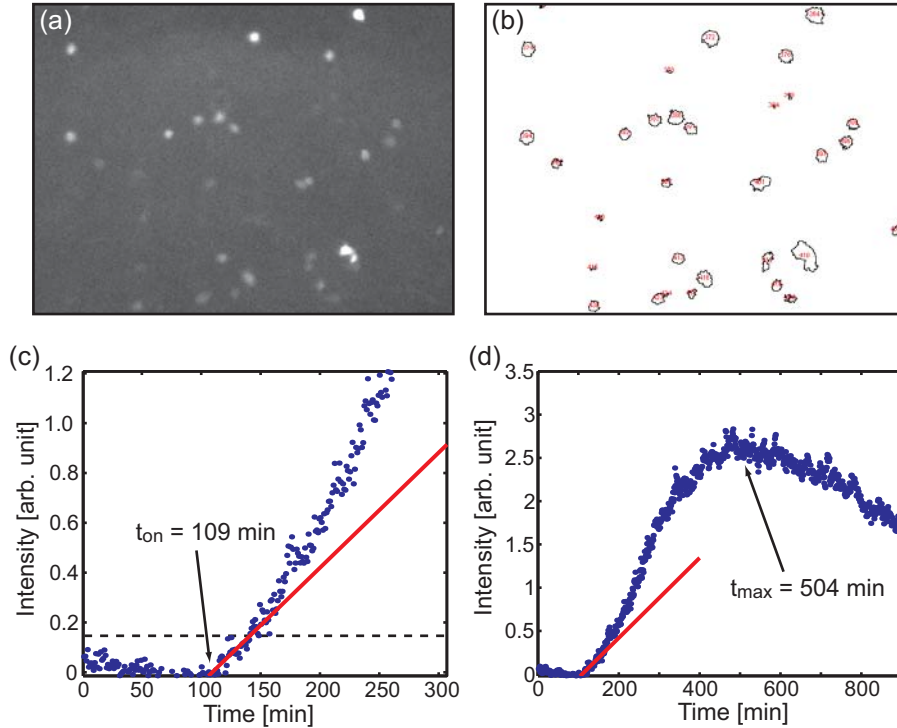


**Figure 6.4:** Analysis of fluorescence images. Hepg2 cells impalefected with Venus plasmid. (a) Part of a fluorescence image captured after 300 min. (b) Outline and position of cells are automatically found for image (a). The time evolution of the intensity for each cell is found. (c) The time when the cell is beginning to express fluorescence is termed  $t_{on}$  and obtained for all cells. (d) A time with maximum fluorescence intensity,  $t_{max}$ , is also found for each cell.

at each cell position for the whole data set. The size of the ROI was chosen larger than most cells to account for minor movements of the cells. As the background is subtracted from the images, one could have chosen a larger ROI with only a small decrease in S/N. However, the probability of having two cells within the same ROI increases with its size, and the  $25 \text{ px} \times 25 \text{ px}$  area was found as a good compromise. The time evolution of the total intensity for a single cell is plotted in Fig. 6.4(c,d).

What we are actually interested in is the time when the cells begin to express fluorescence, which we call  $t_{on}$ . From the time evolution intensity plots one can usually deduce the  $t_{on}$  by eye without problems. It is trickier to build a routine that can do it automatically for all cells. The procedure we used for finding  $t_{on}$  for all cells, was to first remove a constant background, found as the mean value of the first around 25 data points. Hereafter an intensity threshold value was defined, typically around 0.15 as indicated with a dashed line in Fig. 6.4(c). When the intensity exceeds the threshold value, the program fits a straight line to data points around this point, and extrapolates the time for zero intensity. This time is defined as  $t_{on}$  and could be obtained automatically for around 95 % of the fluorescent cells. For the last 5 % we either estimated  $t_{on}$  manually or omitted the results.

For most cells the intensity usually reaches a maximum and then slowly decreases, as

## 6.2. TIME-LAPSE TRANSFECTION EXPERIMENTS

can be seen in Fig. 6.4(d). The decrease is probably due to photobleaching, where the YFPs are destroyed in a photochemical process. The times for the maximum intensity were also found for all cells by smoothing the data and then find the maximum value.

### 6.2.3 Experimental Results

Many different cell lines (e.g. Hepg2, MCF-7, HEK293, CHO, and d3) were studied using the time-lapse imaging of the fluorescence immediately after impalefection. All analyzed cell lines expressed fluorescence using the impalefection method, but in this work, only the Hepg2 and MCF-7 cell lines will be discussed.

Analysis of Hepg2 cells impalefected with Venus plasmid is shown in Fig. 6.5. The histogram shows the distribution of times when the cells begin to express fluorescence after impalefection. The fastest cells are at  $t_{\text{on}} = 70$  min, and most cells begin fluorescence in the time frame  $t_{\text{on}} = 90 - 150$  min. The red solid line is a fit to a Gamma distribution function, which are often used to fit biological data[142]. For this study, the Gamma distribution fit is only used as a crude indicator for the shape of the distribution.

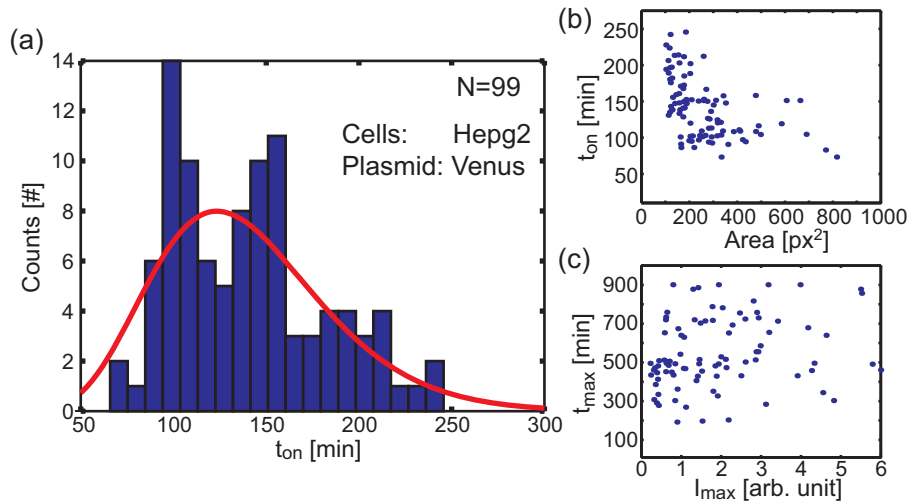


**Figure 6.5:** Analysis of Hepg2 cells impalefected with Venus plasmid. (a) Histogram of  $t_{\text{on}}$  for all analyzed cells in one experiment. The red solid line is the best fit assuming a Gamma distribution. (b)  $t_{\text{on}}$  as a function of the fluorescent area of the cells at  $t = 300$  min. (c) The time for the highest intensity,  $t_{\text{max}}$ , plotted against the intensity value at maximum,  $I_{\text{max}}$ .

Many parameters can be plotted against each other to look for trends between the fluorescence intensity,  $t_{\text{on}}$ ,  $t_{\text{max}}$ , sizes of the cells, etc. In Fig. 6.5(b) is a scatter plot of  $t_{\text{on}}$  versus the size of the cells presented. The areas are measured at  $t = 300$  min using ImageJ. As expected, cells with  $t_{\text{on}}$  close to 300 min have a relative small area and cells with a large area express fluorescence as some of the first ones. If one instead looks at the cells with an area ranging from 200 px<sup>2</sup> to 300 px<sup>2</sup>, cells with both early and late expression of fluorescence are observed, making it difficult to describe a general trend.

The scatter plot in Fig. 6.5(c) shows  $t_{\max}$  versus the intensity at maximum,  $I_{\max}$ . Again, it is difficult to describe any conclusive trends, as the maximum intensity is reached from  $t = 200$  min and up, for different intensities.

For MCF-7 cells impalefected with pd2E YFP plasmid, see Fig. 6.6(a), we observe a comparable distribution of the turn on times as for Hepg2 cells. For this experiment most cells began to express fluorescence in the time interval 60 min to 140 min. The times for the maximum intensities are plotted in a histogram in Fig. 6.6(b), and the red solid line is a Gamma distribution fit with a maximum at around  $t = 400$  min. The effect of photobleaching can be reduced by exposing the fluorophores less, for instance by less intensity, shorter duration of each exposure or increasing the time intervals.

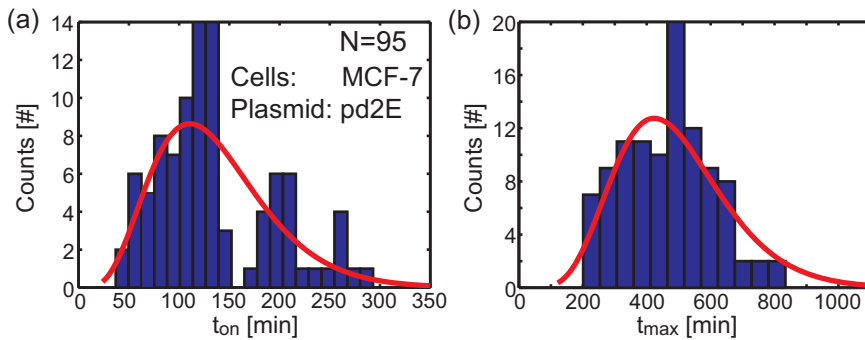


**Figure 6.6:** Analysis of MCF-7 cells impalefected with pd2E YFP plasmid. (a) Histogram of  $t_{\text{on}}$  for all analyzed cells in one experiment. The red solid line is the best fit assuming a Gamma distribution. (b) Histogram of  $t_{\text{max}}$  for the same cells as in (a). The decrease in fluorescence intensity comes from photo bleaching effects.

For some cells we observe apoptosis, or programmed cell death, where the cell kills itself. In Fig. 6.7 the apoptosis of a Hepg2 cell is studied. Within two minutes the cell goes from bright to death, as can be seen in images (b)-(d). About 5 % of all cells showed apoptotic behavior, which is within the range of what we would expect for a normal colony of cells. It therefore seems like the penetration of VACNFs does not stress the cells very much. The presence of fibers might still have other toxic effects to the cells, but no single effect killing all the cells has been found. Also, for a substrate with InAs NWs it has been found that the viability of cells are almost unaffected by the presence of NWs[8].

In summary we have shown that by stabbing the cells with an array of VACNFs it is possible to deliver plasmid directly into them. The fast expression of fluorescence, down to 50 min here and even less in other experiments, indicates that the plasmid is delivered directly to the cell. Impalefection by stabbing is therefore one possible technique for overcoming the challenge with an extremely flexible cell membrane.

A large variation in the time it takes before the cells express fluorescence is observed, and more statistics is needed to understand these differences. When a consistent protocol has been found, one can potentially use this setup to compare cell lines, test new plasmids, and many more experiments.

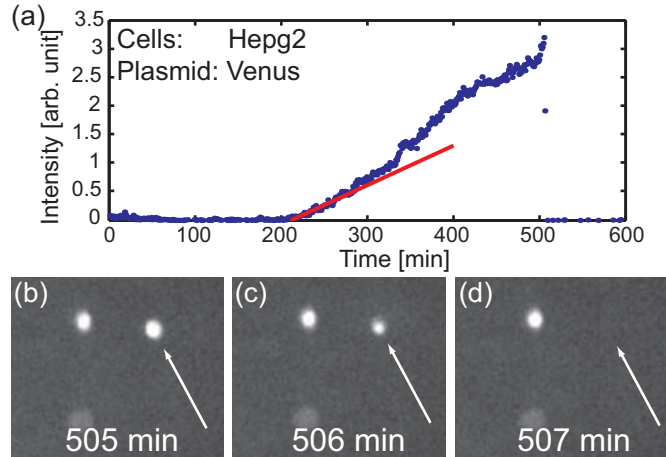


**Figure 6.7:** Time-lapse study of programmed cell death (apoptosis) of a Hepg2 cell. (a) Intensity of the cell as a function of time. From the linear fit (red line) the cell is found to express fluorescence at 214 min and at around 500 min the intensity drops to 0. (b-d) Fluorescence microscope images of the monitored cell (marked with white arrows). In two minutes the intensity of the cell goes from bright to vanish completely.

## 6.3 Electrical Addressable Vertical InAs Nanowires

For measurements on individual cells (see sketch in Fig. 1.3(a)), establishing of leads to the vertically standing NWs is necessary for electrical connection to external instruments so that the NWs can be used e.g. as probes. Similar devices have previously been reported for InAs NWs[143] and VACNFs[144], and we opted for two paths to fabricate such devices:

1. Growth of Au-assisted InAs NWs on GaAs substrates and subsequently etching leads out.
2. Defining leads on SOI substrates using reactive-ion etching (RIE) and subsequently growth of self-assisted InAs NWs.

Both methods proved successful in fabricating electrical addressable vertical NWs. The pre-processing on SOI substrates was the most scalable one, and as larger quantities at some time might be of interest, most effort was put into developing this technique. The fabrication and measurements were carried out in collaboration with the biotec company InXell, Copenhagen.

### 6.3.1 Growth on GaAs Substrates

The basic idea is to create a structure consisting of a conductive layer on top of an insulating layer, followed by a UV lithography defined wet etch step that transforms the conductive layer into conducting leads arranged isolated from each other on top of the insulating layer. For this experiment, undoped GaAs(111)B substrates were used as the insulating structure and a MBE grown InAs bulk layer as the conductive layer.

The substrates were loaded without any pre-treatment and degassed. A 370 nm GaAs layer was added as an in-house grown transition layer which should be more compatible with subsequent in-house grown layers. This layer was grown at  $T = 580$  °C and a  $GR_{\text{GaAs}} = 370$  nm/hr and was followed by a 25 nm buffer layer of  $\text{In}_{0.31}\text{Ga}_{0.69}\text{As}$  grown with a  $GR_{\text{InGaAs}} = 540$  nm/hr. The composition and growth rate are taken as the combined growth rates for GaAs and InAs. The actual composition might be slightly different, but for this study it is not of importance, as it only serves as a strain relaxation layer. At the end, the top layer of 50 nm InAs was grown with  $GR_{\text{InAs}} = 170$  nm/hr at  $T = 300$  °C. A schematic of the grown planar structure is shown in Fig. 6.8(a).

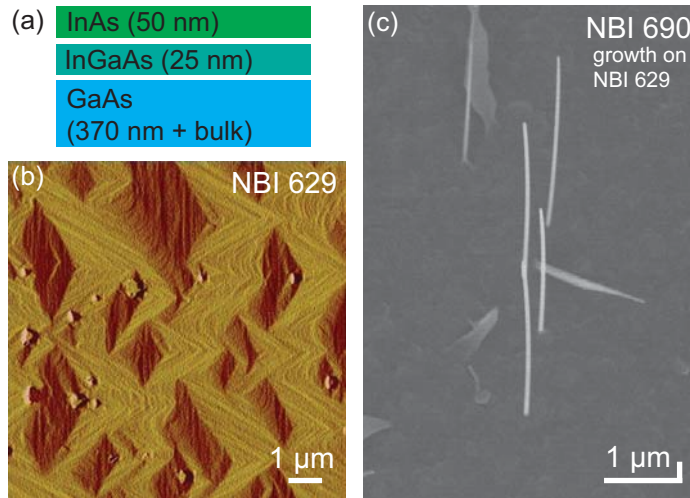


**Figure 6.8:** Growth of InAs NWs on GaAs substrates. (a) Schematic of planar growth of InAs on undoped GaAs(111)B substrates. First a 370 nm thick GaAs layer is grown, then a 25 nm  $\text{In}_{0.31}\text{Ga}_{0.69}\text{As}$  buffer layer for lattice relaxation, and finally a 50 nm InAs layer. (b) Amplitude AFM image of the surface after growth of InAs. The surface roughness is found to  $R_q = 7.0$  nm and  $R_a = 5.5$  nm. Image by Anders Eliassen, InXell. (c) SEM image of Au-assisted InAs NWs grown on the substrate imaged in (b).

The surface of the grown layers was analyzed using tapping mode AFM. Topography, amplitude, and phase images were acquired for a  $10 \mu\text{m} \times 10 \mu\text{m}$  area. The topography image was used to estimate the surface roughness, but an amplitude image is shown in Fig. 6.8(b), as the shape of the structures is easier visualized here. For the substrate shown in the figure, both a surface roughness average and root means square (rms) was computed using the software for the AFM, giving values of  $R_a = 5.5$  nm and  $R_q = 7.0$  nm, respectively.

The surface roughness was reduced by optimizing the growth methods and changing to GaAs(111)B substrates misoriented  $2^\circ$  towards the  $[2\bar{1}\bar{1}]$  direction. For optimized conditions the best growth had a surface roughness of  $R_a = 1.2$  nm and  $R_q = 1.6$  nm.

On top of the bulk growth we have grown Au-assisted InAs NWs as shown in Fig. 6.8(c). We deposited 40 nm Au colloids using the HF-technique (see Sec. 2.3.2) for a fast test of the substrates, but in principle, we could have used e-beam lithography defined Au seeds for enhanced control of the growth. Standard growth parameters were used and we achieved long, vertical NWs.

Leads were now etched out in the InAs layer using UV lithography. An etchant solution of  $\text{H}_2\text{PO}_4:\text{H}_2\text{O}_2:\text{H}_2\text{O}$  (1:1:38) was used for etching of the InAs/InGaAs/GaAs structure in order to define leads. In an experiment where the resistance between two neighboring etch defined InAs leads was measured, it was found that the insulating properties of the undoped GaAs substrate ( $\rho = 1 \cdot 10^7 \Omega\text{m}$ ) would not be good enough when the large resistance of the NW-liquid interface in 'wet experiments' were to be taken into account. This was to some extent overcome by including an AlAs layer in the bulk growth, which has a higher bandgap. However, even better results were obtained using SOI substrates.

#### 6.3.2 Growth on SOI Substrates

Exploiting the newly developed method of self-assisted growth of InAs as described in details in Chap. 5, we took a different approach for contacting individual vertical NWs. SOI substrate from Ultrasil consisting of a device layer of  $2 \mu\text{m}$  n-doped Si(111) with 30 nm thermal oxide on top and a  $500 \mu\text{m}$  Si(100) handle wafer separated by a  $2 \mu\text{m}$  thick oxide layer.

In contrast to the GaAs substrates, the leads were etched out as the first step in the processing on the SOI substrates. For Si(111) substrates, the etch rate of anisotropical wet etchants, for instance KOH, is extremely slow in the (111) direction, so RIE was used instead. The etching of leads were made in collaboration with DTU Danchip, and a sketch of a system with 16 leads is shown in Fig. 6.9(a).

IV measurements were carried out in order to find the leak current/the resistance between neighboring Si(111) leads on top of the insulating  $\text{SiO}_2$  layer. It was not possible to detect a leak current in sweeps from -10 V to +10 V, suggesting that very high quality devices with electrically insulated leads can be made from SOI substrates.

The e-beam lithography step is now a bit more challenging, as it is difficult to evenly spin coat a substrate with  $3 \mu\text{m}$  height differences. We found a solution using a two-step exposure, where large openings are first defined in a thick PMMA layer and subsequently the pattern design exposed in a new thin PMMA layer. The first resist layer consists of 9 % co-polymer and two layers of 8 % PMMA all spin coated at 4000 rpm for 45 sec. This thick layer leveled the height differences on the substrate. The e-beam lithography system was used to make small openings at the end of each lead with a size of around  $10 \mu\text{m} \times 20 \mu\text{m}$ . Hereafter the standard recipe for e-beam lithography was applied, see Sec. 2.3.2, and a dot pattern was exposed within the openings at the end of the leads.

NWs were synthesized following the optimized procedure described in Sec. 5.1.4, with a growth temperature of  $460 \text{ }^\circ\text{C}$ , to ensure minimal sticking on the substrate and still a reasonable growth rate. An In flux corresponding to a bulk equivalent growth rate of  $100 \text{ nm/hr}$  and  $\text{BEP}(\text{As}_4)=1.2 \cdot 10^{-5} \text{ torr}$  was used. A typical growth time of 75 min resulted in  $\sim 6 \mu\text{m}$  long and slightly tapered NWs, with a diameter decreasing from around 130 nm at the bottom to around 80 nm at the tip. An SEM image of a single NW on a lead is shown in Fig. 6.9(c).

To verify that the InAs NWs were well electrically connected with the top Si(111) leads, an insulating SU-8 layer was applied to the device, so that the InAs NWs penetrated the

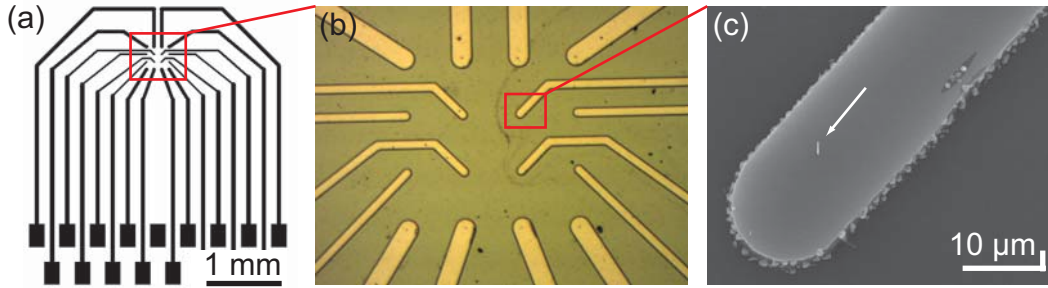


**Figure 6.9:** Growth of InAs NWs on SOI substrates. (a) Sketch of the pattern used to define individual leads by RIE. (b) Optical image (objective 10x) of the ends of the leads. (c) SEM image (tilting angle 15° of a single NW grown on a lead.

SU-8 layer, followed by evaporating gold contacts for bridging NWs of two neighboring leads, as sketched in Fig. 6.10(a). The measured IV curves were linear with resistances in the low  $k\Omega$  regime. In a similar experiment the NWs were connected with a liquid droplet of saline (Fig. 6.10(b)) and it was found that the resistance through the substrate is much greater than the resistance through the NWs and liquid ( $R_{\text{sub}} \gg R_{\text{NWs}}$ ).

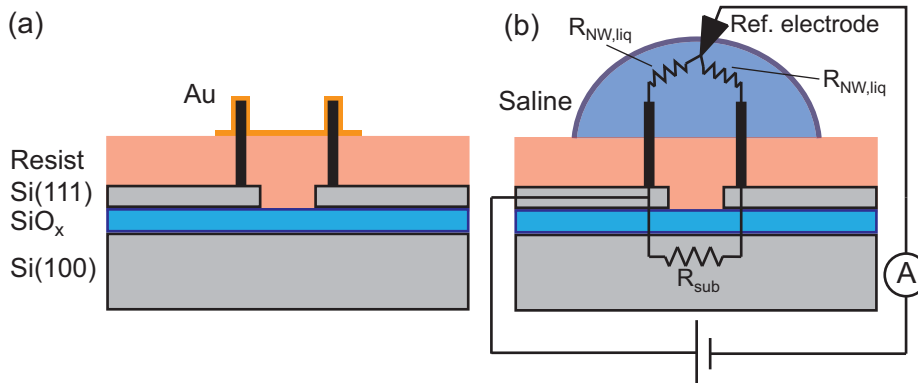


**Figure 6.10:** Setup for measuring the conductivity. (a) Cross-section sketch showing the SOI substrate with NWs prepared for measuring the conductivity. (b) Simple schematic of the resistances in the system. To avoid a leaking current  $R_{\text{sub}}$  must be much greater than  $R_{\text{NWs}}$ .

The integration of InAs NWs on an insulated Si substrate can potentially be used for many different applications, ranging from electroporation and measurements on cells[136] to vertical aligned transistors by using wrap-gates[145]. Several experiments are planned with the devices and results will eventually be presented elsewhere.

In conclusion, we have shown two methods of establishing individual contact to vertical NWs. By using SOI substrates the leaking current is minimal, which is important for high resistance probing measurements, e.g. when NW-liquid interfaces are involved in the electrical circuit.

## 6.4 Capture of Circulating Tumor Cells

Circulating tumor cells (CTCs) are cancer cells transported around in the bloodstream. They are detached from a primary tumor and can facilitate the spreading of cancer to other parts of the body (metastasis)[146]. The concentration is extremely low, only around 1 CTC per billion normal blood cells for patients with cancer, and high quality capturing devices are important for collecting enough cells for studying them.

Some commercial equipment for capturing CTCs is already available[147], but to increase the capturing efficiency, much effort is put into developing CTC capturing devices using microfluidics[148, 149, 150, 151, 152]. In microfluidics, small amounts ( $\mu\text{L}$  or less) of liquid can be controlled precisely using sub-millimeter channels. The invention of soft-lithography using molding of polymers in the late 90s have brought a huge boost to the field of microfluidics and integration with biological systems[153, 154].

In this project we aim for integrating VACNFs in a microfluidic device where the flow of cells can be controlled. The microfluidic devices are fabricated using both SU-8 and poly-di-methyl siloxane (PDMS). Furthermore, we establish electrical contact to the VACNFs, so a static potential can be applied to (hopefully) attract more cells. The project is still on-going, and the work presented here focuses on the fabrication of devices. The results shown are only preliminary and more work is needed, before the devices can be used for screening the blood of cancer patients.

### 6.4.1 Fabrication of Microfluidic Devices

All clean room processing for fabrication of the devices were conducted at Center for Nanophase Materials (CNMS) at ORNL. A guide for fabrication of microfluidic devices using SU-8 has been written, see App. A. It is primarily based on the work performed at CNMS and some tips and tricks from the online guide by Nadkarni have been included[155].

Three types of microfluidic devices were fabricated using SU-8:

- A. Bifurcation channel.** Devices where the liquid is spread out into a large channel and collected again at the other end, see design in Fig. 6.11(a).
- B. SU-8 pillars.** Same structure as device A and with a non-periodic array of  $100\ \mu\text{m}$  pillars filling the large channel. Same structure as in Ref. [148] and used as a reference device. Sketch shown in Fig. 6.11(b).
- C. VACNFs.** Same structure as device A and with bunches of VACNFs grown in a non-periodic array in the channel. Each bunch of fibers are  $\approx 5\ \mu\text{m}$  and devices are fabricated with pitches of 15, 25, and  $50\ \mu\text{m}$ . SEM images shown in Fig. 6.11(c).

And two types of lids were constructed for covering the channel:

- X. Plain.** An indium tin oxide (ITO) coated microscope glass slide ( $1\ \text{inch} \times 3\ \text{inches}$ ) covered with a plain layer of PDMS. A  $17\ \mu\text{m}$  thick plain layer was obtained by spin coating the PDMS on at 3000 rpm for 45 sec and let it harden for at least 12 hours at room temperature.

**Y. Herringbone structure.** An ITO covered Borofloat glass substrate with a chaotic mixer molded in SU-8[156], which looks like a herringbone (Fig. 6.11(d)). These devices were fabricated in the same way as the microfluidic channels.

A total of 6 different devices were possible by combination of the microfluidic base structures and lids, as summarized in Tab. 6.1.

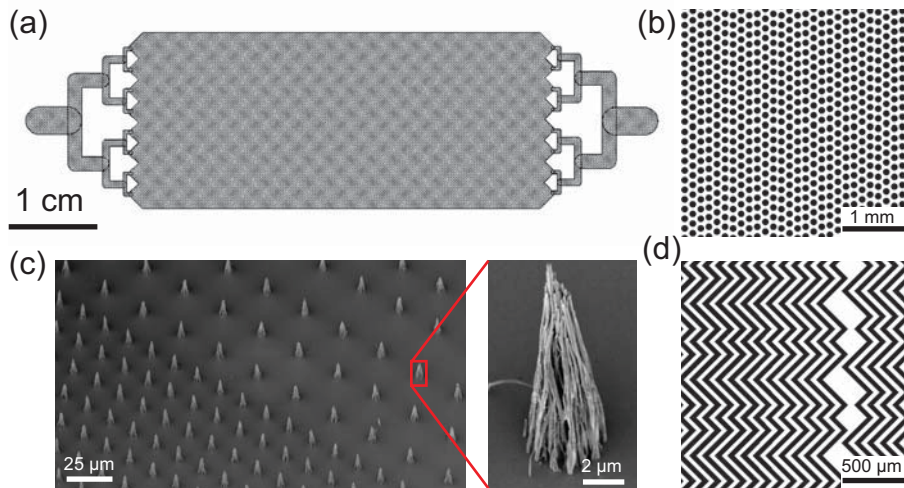


**Figure 6.11:** Microfluidic designs for capturing of CTCs. (a) Basic bifurcation channel. Due to the symmetric design, the inlet and outlet can be interchanged, that is, flow can be established in both directions. (b) Pillars positioned in an asymmetric array for increased 'bouncing' of the cells. (c) Bundles of VACNFs to be positioned within the flow channel shown in (a). (d) Herringbone structure for the lid to induce mixing in the otherwise laminar flow.

Microfluidic structure			
Channel	Lid	Reference	Fabricated
A	X	Basic	yes
A	Y	[150]	yes
B	X	[148]	yes
B	Y	[148]+[150]	no
C	X	New	yes
C	Y	New	yes

**Table 6.1:** Overview of the fabricated devices for capturing CTCs. The description of the different channels and lids can be found in the text and in Fig. 6.11.

The base microfluidic channel and the lid were assembled by plasma induced bonding[157]. Silanol groups (OH) are exposed at the PDMS surface by oxygen plasma cleaning. When two activated surfaces are brought together they form covalent siloxane bonds (Si-O-Si), found to have a bond strength of 300 kPa[157]. The PDMS was treated for 30 sec in

## 6.4. CAPTURE OF CIRCULATING TUMOR CELLS

the oxygen plasma and the substrates should be bonded immediately after the end of the treatment, that is, within one minute after being exposed to atmospheric air.

As the microfluidic channel was molded in SU-8 the surface had to be silanized first. A simple method for the silanization was to place the SU-8 channel in a closed zipper bag with a few droplets of 3-Aminopropyltrimethoxysilane for half an hour. The SU-8 was now handled in the same way as the PDMS.

The seal formed by the cross-link between PDMS and SU-8 was not completely tight. The seal could probably be improved by optimization of the processes, but instead we tightened it using the bio-compatible epoxy Traecon FDA-2T. At the same time rubber tubes were glued on to the in- and outlets of the channel, see optical image in Fig. 6.12.



**Figure 6.12:** Simple SU-8 microfluidic channel (type A) on a half 4 inch substrate plasma bonded to a PDMS coated glass slide (type X). The seal has been tightened and one inlet glued on with epoxy.

### 6.4.2 Flow Studies using Cancer Cells

It is difficult to mimic the flow behavior of cells using synthetic materials, so living cells were used for studying the flow in the channels. Cancer cells are often bigger than other cells, so we opted for breast cancer cells of the type Michigan Cancer Foundation - 7 (MCF-7) for the simple flow studies. The MCF-7 cells were cultured and a low concentration was suspended in a PBS solution.

In the first series of experiments we were only interested in the flow behavior of the cells. To avoid capturing of cells, the channel was coated with Bovine Serum Albumin (BSA). A solution of 1 mg/mL BSA was diluted in PBS and flushed through the channel. The cells were now let into the channel and monitored using an optical microscope (OM); in first place just through the eye pieces and later on with a CCD camera. The flow rate was controlled by differential pressure, that is, by raising or lowering the inlet tube. A height difference of up to 10 cm between levels of the solution in the inlet and outlet tubes could be achieved in the given setup.

A series of time-lapse images were obtained to measure the velocity of cells in a channel with VACNFs (type C-X), which are shown in Fig. 6.13. The inlet was raised and the movement of the cell (indicated by a black arrow) could be traced. For a height difference of 10 cm the cell velocity was found to 90  $\mu\text{m}/\text{sec}$ . In the image at  $t = 2$  sec it is observed that the cell hits a bunch of VACNFs and changes its direction. The trajectory of the cell

is plotted in the last image with a white dashed line, and the change in direction can be seen.

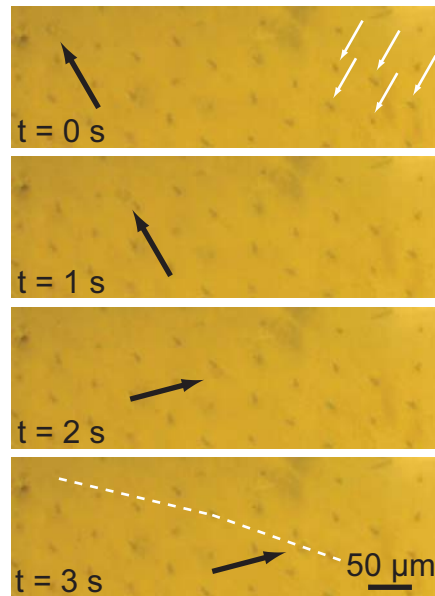


**Figure 6.13:** Time-lapse OM images for flow study of a microfluidic channel with bunches of VACNFs (type C) and a plain lid (type X) using MCF-7 cells. The flow rate was controlled by lifting the inlet tube to a higher level than the outlet, and the images are obtained for a height difference of 10 cm, giving a cell velocity of  $90 \mu\text{m}/\text{sec}$ . The black arrows show the position of the cell and the white arrows indicate some of the VACNFs. In the image for  $t = 2$  sec, the cell hits a bunch of VACNFs and changes direction, as can also be seen from the trajectory (white dashed line) plotted in the last image.

Flow studies of the bare channel devices (type A-X) gave comparable results for the velocity of cells, indicating that the presence of VACNFs only have little influence of the flow in the devices. The influence of the chaotic mixer does not seem to change the flow rate much for both the bare channels and with fibers in (types A-Y and C-Y). More experiments will be necessary to test whether the chaotic mixer actually improves the cells/fibers interaction.

For the microfluidic systems with pillars, the cells follow a smooth path around the pillars, and no bouncing with abrupt change in their direction are observed. The shear forces are large for the pillar devices and seem to prevent physical contact. It seems that VACNFs have a major advantage compared to the pillar structures with respect to physical contact.

### 6.4.3 Outlook

In the simple flow experiments we see that the trajectories of the cells are influenced by the VACNFs. In the OM they appear to have contact, but shear forces might prevent actual physical contact. Further experiments are needed to clarify this. Also, by applying

a potential to all the VACNFs, it might be possible to attract the cells and enhance physical contact to the fibers.

To actually capture CTCs in a bloodstream, the VACNFs will have to be chemically functionalized with epithelial cell adhesion molecule (EpCAM) antibodies, as have also been used in other studies[148, 150]. EpCAM is found in most cancer cells and is at the same time absent from hematology cells. The antibodies will therefore only capture the cancer cells.

The next step with the devices is to test the capturing efficiency of MCF-7 after functionalization with EpCAM antibodies. The flow rate should be optimized, such that it is as high as possible and still have a high capturing efficiency. For the devices to be of commercial interest, it is of paramount interest to provide a fast and reliable method for the blood screening.

Hereafter experiments with blood from cancer patients can be initiated. Only few  $\mu\text{L}$  of blood is necessary for each experiment, and as there is no direct contact with the patients, the administrative work for starting clinical test should not be overwhelming. Also, it will be necessary to compare the new method to previously reported microfluidic systems and commercially available equipment.

## 6.5 Summary

The interface of nano-sized structures with mammalian cells has been discussed and experiments using InAs NWs and VACNFs have been described. Despite the small size of NWs, typically less than 100 nm, the cell membrane can wrap around the NWs as tent-like structures, without being penetrated. By mechanically pressing a substrate with VACNFs down on cells centrifuged into a pellet we have demonstrated one way to get intra-cellular access. This has been found by the fast expression of a fluorescent protein.

By integrating a large array of VACNFs with a microfluid channel, we have fabricated a device suitable for capturing of CTCs. By combining different microfluidic designs of base channels and lids, a total of 5 different devices were fabricated. Simple flow measurements were performed, showing that the cells have much more contact with bunches of VACNFs than SU-8 defined micropillars.



## Summary

The process of fabricating InAs NWs in a MBE system has been discussed and through a series of experiments an optimal set of parameters for Au-assisted growth is found for a substrate temperature of 425 °C, an In flux equivalent to a bulk growth rate of  $GR_{\text{In}} = 400$  nm/hr and a high  $\text{As}_2$  flux of around  $1 \cdot 10^{-5}$  torr. Using these conditions for e-beam lithography deposited Au droplets, a yield exceeding  $> 99$  % has been achieved on an entire 2 inch substrate. By applying a two step growth technique, where thin NWs are overgrown with a planar layer, long segments ( $> 3 \mu\text{m}$ ) of pure WZ NWs with a tunable diameter have been fabricated.

InAs NWs have also been synthesized on Si(111) substrates without a foreign catalyst particle. Several methods for controlling the oxide layer is presented and an optimal thickness of the oxide layer is found to be 9 Å. The underlying growth mechanism for these self-assisted growths has been investigated and it is found that a droplet can be formed on top of each NW, but that it usually disappears again at a growth temperature of 460 °C. By introducing As interrupts during the growth, a droplet can be formed, and growth can continue in a vapor-liquid-solid mode. This is observed by reverse tapering of some NWs, where the tip is thicker than the bottom, and from pyramidal structures formed on top of the wires. Also by first forming a liquid In droplet, we have shown that homoepitaxial growth of self-assisted InAs NWs is possible.

It is shown that NWs can be positioned by selectively define openings in a 30 nm oxide layer, and large scale arrays have been fabricated, with a yield of up to 85 %. The yield of self-assisted NWs is found to be extremely dependent on the pre-treatment methods, and optimization of these are suggested as the most important. Only few experiments with dry etching were tried, and optimization of the dry etching conditions might help to improve the yield.

An *in-situ* growth and characterization experiment has been presented. With an MBE chamber attached to a synchrotron beam line the evolution in crystal structure formation has been monitored for different growth conditions. Changes in the crystal structure are observed to happen at a time scale slower than

Several devices utilizing NWs and VACNFs have been produced, with focus on mea-

measurements on living cells. For instance, VACNFs integrated in a microfluidic channel for capturing of CTCs have been fabricated and flow studies of cancer cells carried out. We have also shown that contact to individual vertical NWs is possible by growth on SOI substrates where leads have been etched out in the surface. These devices could for instance be used for electrical measurements on cells.

## 7.1 Outlook

The number of groups involved in research related to NW growth is rapidly growing and to be among the best, the requirements to produce high quality NWs steadily increase. The fabrication of NWs with long defect free WZ segments was one achievement, but further control of the growth procedure is necessary to continuously improve the devices where NWs are used. Another interesting option is to begin the fabrication of InSb NWs[106], as these are expected to have superior properties for low temperature transport measurements.

Both MBE and MOCVD are widely used for synthesis of NWs. The advantage of the MOCVD is the faster growth time, especially in the loading and degassing phase, and therefore a much higher throughput. On the other hand, a MBE system has a cleaner environment and in principle one should be able to produce higher quality devices[39, 40]. One can also grow crystal layers at a much lower temperature in a MBE, as no cracking of precursors is necessary. This has for instance been used for capping the NWs while still in the ultra high vacuum to protect the surface from oxidation[106].

The growth of self-assisted InAs NWs is a new field, and the first MBE grown wires were reported less than 3 years ago[65]. The mixed crystal structure and less controllable growth method is still a major limitation to their popularity. However the easier integration with the Si industry makes them very interesting for future devices. So far the only method for tuning the crystal structure has been to introduce small amounts of Sb to the growth[135], but the formation of a droplet might be another way to gain control of the stacking formation. To continue the experiments it can be interesting to investigate the droplet formation in *in-situ* x-ray diffraction setup[III]. The *in-situ* x-ray experiments can be improved in many ways. It is important to eliminate the parasitic bulk growth by optimizing the growth conditions of patterned growth, and eventually one can focus the beam to only a single NW during growth.

The fundamental understanding of NW growth dynamics improves all the time, and especially new characterization techniques, such as *in-situ* TEM[24, 25] and RHEED[68], have significantly improved the understanding of NW growth. A lot of complex processes are involved in NW growth and a 'real' theoretical model needs to take all these into account. Experiments that investigate a sub area, such as studies of the diffusion lengths, aid the overall understanding of NW growth. The continuous improvement of growth and characterization methods is important for the theoretical description of NW growth and we can expect a much improved understanding of the growth processes within the next few years.

The interdisciplinary field of integrating nanostructures with living cells opens a new

## 7.1. OUTLOOK

---

world of possibilities. New applications are reported all the time and I think it in the coming years will revolutionize our way of developing new drugs. One might be able to target the drug delivery to individual cells and monitor them for an extended period of time. Much improved understanding can be obtained when one can manipulate individual cells and look at the influence of one effect at a time.

Microfluidic channels can be used for a lot more than capture of CTCs. By integrating the nanostructures in a microfluidic channel an enhanced control of the cell environment can be achieved[154]. For instance, a microfluidic channel can help us to faster and much easier change of media in which the cells are living[153].

With the first products using NWs becoming available on the consumer market and much research concerned with NWs, I expect the field of NW growth and device fabrication using NWs to expand much in the years to come. I am convinced we will see many applications using NWs, but it will be interesting to see, in which field they have the greatest impact.



## Guide to SU8 microfluidics

*Guide based on a 4 inch Si(100) substrate*

Author: Morten Hannibal Madsen

Place: CNMS at ORNL

### **Spin coating**

1. Dehydrate the substrate for at least 30 min at 180 °C. There is no upper limit on the dehydration time.
2. Find desired thickness of SU8 in the recipe book. For a 30  $\mu\text{m}$  layer, use SU8 2015 with 1300 rpm for 30 sec and an acceleration of 300 rpm/s.
  - (a) Nadkarni: Use two step spinning, first 500 rpm with 100 rpm/s ramp to spread the resist, then 2000 rpm with 400 rpm/s ramp to get the desired thickness.
3. Pour SU8 directly from a small bottle to the center of the substrate
  - (a) Nadkarni: Heat 2 min on 200 °C hotplate just before loading at spinner.
  - (b) Nadkarni: Pour into the small bottle at least one day in advance to ensure no air bubbles are left.
  - (c) Nadkarni: Pour slowly and very close to the substrate.
  - (d) Nadkarni: Weight the bottle before and after to estimate the amount of used SU8, aim for 4 g.
4. Use the higher end of the suggested bake times. For 30  $\mu\text{m}$  use 2 min at 65 °C and 5-6 min at 95°C. If the resist is still sticky when you take it off, bake it for some longer.
  - (a) Important that the heater is leveled, i.e. use one of the new heaters.

- (b) Nadkarni: If the SU8 layer does not look uniform, it is better to start over with a new wafer. It is extremely difficult to get SU8 off again.
- (c) Nadkarni: Put a cover on with holes, so air vapor can escape. The cover protects the substrate from dust particles.

### Exposure

5. Use mask aligner in pressure contact mode (program 6). 16 sec exposure seems to work fine for 30  $\mu\text{m}$  SU8. Look away during exposure.
6. For a thick resist layer ( $> 5\mu\text{m}$ ) the substrate might need some time to rest after exposure, to give it time for re-accumulating some moisture.
7. Post-bake substrate for 2 min at 65 °C and 5 min at 95 °C. Might be that a temperature ramp will give fewer cracks.
  - (a) Nadkarni: Use a temperature ramp to avoid cracks. 1 min at 65 °C, ramp up to 75 °C, wait 1 min, ramp up to 85 °C, wait 1 min, ramp up to 95 °C, wait 4 min. Do the same on the way back. Take off substrate when at 65 °C.

### Development

8. Use the puddle-development-method
  - (a) Use SU8-developer in squeezing bottle in the fume hood.
  - (b) Put the substrate in a container and pour a little developer on it
  - (c) Continue to pour small amounts of developer on for 3-5 min
  - (d) Make the IPA test. If substrate turns white when poured with IPA, it is not fully developed. Go back to step c.
  - (e) Rinse with IPA and blow dry with nitrogen.
9. Look at the structures in an optical microscope.

### Final steps

10. Hard-bake for 5 min at 180 °C.
11. Measure the height using the profilometer (Dektak).

# Bibliography

- [1] K. S. Novoselov, A. K. Geim, S. V. Morozov, D. Jiang, Y. Zhang, S. V. Dubonos, I. V. Grigorieva, and A. A. Firsov, “Electric Field Effect in Atomically Thin Carbon Films,” *Science*, vol. 306, no. 5696, pp. 666–669, 2004.
- [2] R. Yan, D. Gargas, and P. Yang, “Nanowire photonics,” *Nature Photonics*, vol. 3, pp. 569–576, Oct. 2009.
- [3] C. K. Chan, H. Peng, G. Liu, K. McIlwrath, X. F. Zhang, R. A. Huggins, and Y. Cui, “High-performance lithium battery anodes using silicon nanowires,” *Nature Nanotechnology*, vol. 3, pp. 31–35, Jan. 2008.
- [4] F. Patolsky, G. Zheng, and C. M. Lieber, “Nanowire-Based Biosensors,” *Analytical Chemistry*, vol. 78, no. 13, pp. 4260–4269, 2006.
- [5] A. Milnes and A. Polyakov, “Indium arsenide: a semiconductor for high speed and electro-optical devices,” *Materials Science and Engineering: B*, vol. 18, no. 3, pp. 237 – 259, 1993.
- [6] P. Wongsrikeao, D. Saenz, T. Rinkoski, T. Otoi, and E. Poeschla, “Antiviral restriction factor transgenesis in the domestic cat,” *Nat Meth*, vol. 8, pp. 853–859, Oct. 2011.
- [7] T. Berthing, C. B. Sørensen, J. Nygård, and K. L. Martinez, “Applications of Nanowire Arrays in Nanomedicine,” *Journal of Nanoneuroscience*, vol. 1, pp. 3–9, June 2009.
- [8] T. Berthing, S. Bonde, C. B. Sørensen, P. Utko, J. Nygård, and K. L. Martinez, “Intact Mammalian Cell Function on Semiconductor Nanowire Arrays: New Perspectives for Cell-Based Biosensing,” *Small*, vol. 7, no. 5, pp. 640–647, 2011.
- [9] B. Tian, T. Cohen-Karni, Q. Qing, X. Duan, P. Xie, and C. M. Lieber, “Three-Dimensional, Flexible Nanoscale Field-Effect Transistors as Localized Bioprobes,” *Science*, vol. 329, pp. 830–, Aug. 2010.

- [10] W. Kim, J. K. Ng, M. E. Kunitake, B. R. Conklin, and P. Yang, "Interfacing Silicon Nanowires with Mammalian Cells," *Journal of the American Chemical Society*, vol. 129, no. 23, pp. 7228–7229, 2007.
- [11] J. T. Robinson, M. Jorgolli, A. K. Shalek, M.-H. Yoon, R. S. Gertner, and H. Park, "Vertical nanowire electrode arrays as a scalable platform for intracellular interfacing to neuronal circuits," *Nature Nanotechnology*, vol. 7, pp. 180–184, Mar. 2012.
- [12] T. E. McKnight, A. V. Melechko, G. D. Griffin, M. A. Guillorn, V. I. Merkulov, F. Serna, D. K. Hensley, M. J. Doktycz, D. H. Lowndes, and M. L. Simpson, "Intracellular integration of synthetic nanostructures with viable cells for controlled biochemical manipulation," *Nanotechnology*, vol. 14, no. 5, p. 551, 2003.
- [13] T. E. McKnight, A. V. Melechko, D. K. Hensley, D. G. J. Mann, G. D. Griffin, and M. L. Simpson, "Tracking Gene Expression after DNA Delivery Using Spatially Indexed Nanofiber Arrays," *Nano Letters*, vol. 4, pp. 1213–1219, July 2004.
- [14] R. S. Wagner and W. C. Ellis, "VAPOR-LIQUID-SOLID MECHANISM OF SINGLE CRYSTAL GROWTH," *Applied Physics Letters*, vol. 4, no. 5, pp. 89–90, 1964.
- [15] A. I. Persson, M. W. Larsson, S. Stenström, B. J. Ohlsson, L. Samuelson, and L. R. Wallenberg, "Solid-phase diffusion mechanism for GaAs nanowire growth," *Nature Materials*, vol. 3, pp. 677–681, Oct. 2004.
- [16] J. C. Harmand, G. Patriarche, N. Péré-Laperne, M.-N. Mérat-Combes, L. Travers, and F. Glas, "Analysis of vapor-liquid-solid mechanism in Au-assisted GaAs nanowire growth," *Applied Physics Letters*, vol. 87, p. 203101, Nov. 2005.
- [17] F. Glas, J.-C. Harmand, and G. Patriarche, "Why Does Wurtzite Form in Nanowires of III-V Zinc Blende Semiconductors?," *Phys. Rev. Lett.*, vol. 99, p. 146101, Oct 2007.
- [18] R. E. Algra, M. A. Verheijen, M. T. Borgström, L.-F. Feiner, G. Immink, W. J. P. van Enckevort, E. Vlieg, and E. P. A. M. Bakkers, "Twinning superlattices in indium phosphide nanowires," *Nature*, vol. 456, pp. 369–372, Nov. 2008.
- [19] J. Johansson, K. A. Dick, P. Caroff, M. E. Messing, J. Bolinsson, K. Deppert, and L. Samuelson, "Diameter Dependence of the Wurtzite/Zinc Blende Transition in InAs Nanowires," *The Journal of Physical Chemistry C*, vol. 114, no. 9, pp. 3837–3842, 2010.
- [20] V. G. Dubrovskii, N. V. Sibirev, J. C. Harmand, and F. Glas, "Growth kinetics and crystal structure of semiconductor nanowires," *Phys. Rev. B*, vol. 78, p. 235301, Dec 2008.
- [21] G. E. Cirlin, V. G. Dubrovskii, Y. B. Samsonenko, A. D. Bouravleuy, K. Durose, Y. Y. Proskuryakov, B. Mendes, L. Bowen, M. A. Kaliteevski, R. A. Abram, and

## BIBLIOGRAPHY

---

- D. Zeze, "Self-catalyzed, pure zincblende GaAs nanowires grown on Si(111) by molecular beam epitaxy," *Phys. Rev. B*, vol. 82, p. 035302, Jul 2010.
- [22] P. Krogstrup, S. Curiotto, E. Johnson, M. Aagesen, J. Nygård, and D. Chatain, "Impact of the Liquid Phase Shape on the Structure of III-V Nanowires," *Phys. Rev. Lett.*, vol. 106, p. 125505, Mar 2011.
- [23] K. W. Schwarz and J. Tersoff, "Elementary Processes in Nanowire Growth," *Nano Letters*, vol. 11, pp. 316–320, Feb. 2011.
- [24] S. H. Oh, M. F. Chisholm, Y. Kauffmann, W. D. Kaplan, W. Luo, M. Rühle, and C. Scheu, "Oscillatory Mass Transport in Vapor-Liquid-Solid Growth of Sapphire Nanowires," *Science*, vol. 330, no. 6003, pp. 489–493, 2010.
- [25] C.-Y. Wen, J. Tersoff, K. Hillerich, M. C. Reuter, J. H. Park, S. Kodambaka, E. A. Stach, and F. M. Ross, "Periodically Changing Morphology of the Growth Interface in Si, Ge, and GaP Nanowires," *Phys. Rev. Lett.*, vol. 107, p. 025503, Jul 2011.
- [26] M. Tchernycheva, L. Travers, G. Patriarche, F. Glas, J.-C. Harmand, G. E. Cirilin, and V. G. Dubrovskii, "Au-assisted molecular beam epitaxy of InAs nanowires: Growth and theoretical analysis," *Journal of Applied Physics*, vol. 102, p. 094313, Nov. 2007.
- [27] J. Johansson, C. P. T. Svensson, T. Mårtensson, L. Samuelson, and W. Seifert, "Mass Transport Model for Semiconductor Nanowire Growth," *The Journal of Physical Chemistry B*, vol. 109, no. 28, pp. 13567–13571, 2005.
- [28] V. G. Dubrovskii, N. V. Sibirev, G. E. Cirilin, I. P. Soshnikov, W. H. Chen, R. Larde, E. Cadel, P. Pareige, T. Xu, B. Grandidier, J.-P. Nys, D. Stievenard, M. Moewe, L. C. Chuang, and C. Chang-Hasnain, "Gibbs-Thomson and diffusion-induced contributions to the growth rate of Si, InP, and GaAs nanowires," *Phys. Rev. B*, vol. 79, p. 205316, May 2009.
- [29] V. G. Dubrovskii, G. E. Cirilin, I. P. Soshnikov, A. A. Tonkikh, N. V. Sibirev, Y. B. Samsonenko, and V. M. Ustinov, "Diffusion-induced growth of GaAs nanowhiskers during molecular beam epitaxy: Theory and experiment," *Phys. Rev. B*, vol. 71, p. 205325, May 2005.
- [30] L. E. Jensen, M. T. Björk, S. Jeppesen, A. I. Persson, B. J. Ohlsson, and L. Samuelson, "Role of Surface Diffusion in Chemical Beam Epitaxy of InAs Nanowires," *Nano Letters*, vol. 4, no. 10, pp. 1961–1964, 2004.
- [31] M. C. Plante and R. R. Lapierre, "Analytical description of the metal-assisted growth of III-V nanowires: Axial and radial growths," *Journal of Applied Physics*, vol. 105, p. 114304, June 2009.

- [32] K. v. Klitzing, G. Dorda, and M. Pepper, “New Method for High-Accuracy Determination of the Fine-Structure Constant Based on Quantized Hall Resistance,” *Phys. Rev. Lett.*, vol. 45, pp. 494–497, Aug 1980.
- [33] C. B. Sørensen, *MBE-Growth, Processing and Characterization of Low-Dimensional GaAs/AlAs Heterostructures*. PhD thesis, Mikroelektronik Centret and Niels Bohr Institute, 1998.
- [34] S. R. Johnson, C. Lavoie, E. Nodwell, M. K. Nissen, T. Tiedje, and J. A. Mackenzie, “Factors affecting the temperature uniformity of semiconductor substrates in molecular-beam epitaxy,” *Journal of Vacuum Science & Technology B: Microelectronics and Nanometer Structures*, vol. 12, pp. 1225–1228, 1994.
- [35] P. Vandenabeele and K. Maex, “Influence of temperature and backside roughness on the emissivity of Si wafers during rapid thermal processing,” *Journal of Applied Physics*, vol. 72, pp. 5867–5875, Dec. 1992.
- [36] J. C. Sturm and C. M. Reaves, “Silicon Temperature Measurement by Infrared Absorption: Fundamental Processes and Doping Effects,” *IEEE Transactions on Electron Devices*, vol. 39, no. 1, p. 81, 1992.
- [37] P. J. Timans, “Emissivity of silicon at elevated temperatures,” *Journal of Applied Physics*, vol. 74, pp. 6353–6364, Nov. 1993.
- [38] T. Matsumoto, A. Cezairliyan, and D. Basak, “Hemispherical Total Emissivity of Niobium, Molybdenum, and Tungsten at High Temperatures Using a Combined Transient and Brief Steady-State Technique,” *International Journal of Thermophysics*, vol. 20, pp. 943–952, 1999.
- [39] C. Thelander, K. A. Dick, M. T. Borgström, L. E. Fröberg, P. Caroff, H. A. Nilsson, and L. Samuelson, “The electrical and structural properties of n-type InAs nanowires grown from metal-organic precursors,” *Nanotechnology*, vol. 21, no. 20, p. 205703, 2010.
- [40] H. Shtrikman, R. Popovitz-Biro, A. Kretinin, and P. Kacman, “GaAs and InAs Nanowires for Ballistic Transport,” *Selected Topics in Quantum Electronics, IEEE Journal of*, vol. 17, pp. 922–934, july-aug. 2011.
- [41] F. Martelli, S. Rubini, M. Piccin, G. Bais, F. Jabeen, S. De Franceschi, V. Grillo, E. Carlino, F. D’Acapito, F. Boscherini, S. Cabrini, M. Lazzarino, L. Businaro, F. Romanato, and A. Franciosi, “Manganese-Induced Growth of GaAs Nanowires,” *Nano Letters*, vol. 6, no. 9, pp. 2130–2134, 2006.
- [42] K. Hillerich, M. E. Messing, L. R. Wallenberg, K. Deppert, and K. A. Dick, “Epitaxial InP nanowire growth from Cu seed particles,” *Journal of Crystal Growth*, vol. 315, no. 1, pp. 134–137, 2011.

## BIBLIOGRAPHY

---

- [43] M. Messing, K. Hillerich, J. Johansson, K. Deppert, and K. A. Dick, “The use of gold for fabrication of nanowire structures,” *Gold Bulletin*, vol. 42, no. 3, pp. 172–181, 2009.
- [44] P. Kratzer, S. Sakong, and V. Pankoke, “Catalytic Role of Gold Nanoparticle in GaAs Nanowire Growth: A Density Functional Theory Study,” *Nano Letters*, vol. 12, no. 2, pp. 943–948, 2012.
- [45] S. Breuer, C. Pfüller, T. Flissikowski, O. Brandt, H. T. Grahn, L. Geelhaar, and H. Riechert, “Suitability of Au- and Self-Assisted GaAs Nanowires for Optoelectronic Applications,” *Nano Letters*, vol. 11, no. 3, pp. 1276–1279, 2011.
- [46] M. Bar-Sadan, J. Barthel, H. Shtrikman, and L. Houben, “Direct Imaging of Single Au Atoms Within GaAs Nanowires,” *Nano Letters*, vol. 12, no. 5, pp. 2352–2356, 2012.
- [47] J. E. Allen, E. R. Hemesath, D. E. Perea, J. L. Lensch-Falk, Z. Y. Li, F. Yin, M. H. Gass, P. Wang, A. L. Bleloch, R. E. Palmer, and L. J. Lauhon, “High-resolution detection of Au catalyst atoms in Si nanowires,” *Nature Nanotechnology*, vol. 3, pp. 168–173, Mar. 2008.
- [48] M. Messing, K. Hillerich, J. Bolinsson, K. Storm, J. Johansson, K. Dick, and K. Deppert, “A comparative study of the effect of gold seed particle preparation method on nanowire growth,” *Nano Research*, vol. 3, pp. 506–519, 2010.
- [49] T. Mårtensson, M. Borgström, W. Seifert, B. J. Ohlsson, and L. Samuelson, “Fabrication of individually seeded nanowire arrays by vapour liquid solid growth,” *Nanotechnology*, vol. 14, no. 12, p. 1255, 2003.
- [50] J. Motohisa, J. Noborisaka, J. Takeda, M. Inari, and T. Fukui, “Catalyst-free selective-area MOVPE of semiconductor nanowires on (111)B oriented substrates,” *Journal of Crystal Growth*, vol. 272, no. 1-4, pp. 180–185, 2004.
- [51] C. J. Novotny and P. K. L. Yu, “Vertically aligned, catalyst-free InP nanowires grown by metalorganic chemical vapor deposition,” *Applied Physics Letters*, vol. 87, no. 20, p. 203111, 2005.
- [52] B. Mandl, J. Stangl, T. Mårtensson, A. Mikkelsen, J. Eriksson, L. S. Karlsson, G. Bauer, L. Samuelson, and W. Seifert, “Au-Free Epitaxial Growth of InAs Nanowires,” *Nano Letters*, vol. 6, pp. 1817–1821, Aug. 2006.
- [53] K. Tomioka, P. Mohan, J. Noborisaka, S. Hara, J. Motohisa, and T. Fukui, “Growth of highly uniform InAs nanowire arrays by selective-area MOVPE,” *Journal of Crystal Growth*, vol. 298, pp. 644–647, Jan. 2007.

- [54] S. A. Dayeh, E. T. Yu, and D. Wang, "Growth of InAs Nanowires on SiO<sub>2</sub> Substrates: Nucleation, Evolution, and the Role of Au Nanoparticles," *The Journal of Physical Chemistry C*, vol. 111, no. 36, pp. 13331–13336, 2007.
- [55] H. Paetzelt, V. Gottschalch, J. Bauer, G. Benndorf, and G. Wagner, "Selective-area growth of GaAs and InAs nanowires - homo- and heteroepitaxy using SiN<sub>x</sub> templates," *Journal of Crystal Growth*, vol. 310, pp. 5093–5097, Nov. 2008.
- [56] K. Tomioka, J. Motohisa, S. Hara, and T. Fukui, "Control of InAs Nanowire Growth Directions on Si," *Nano Letters*, vol. 8, no. 10, pp. 3475–3480, 2008.
- [57] D. Forbes, S. Hubbard, R. Raffaele, and J. S. McNatt, "Au-catalyst-free epitaxy of InAs nanowires," *Journal of Crystal Growth*, vol. 312, no. 8, pp. 1391 – 1395, 2010.
- [58] M. T. Björk, H. Schmid, C. M. Breslin, L. Gignac, and H. Riel, "InAs nanowire growth on oxide-masked  $\langle 111 \rangle$  silicon," *Journal of Crystal Growth*, vol. 344, pp. 31–37, Apr. 2012.
- [59] C. Colombo, D. Spirkoska, M. Frimmer, G. Abstreiter, and A. Fontcuberta i Morral, "Ga-assisted catalyst-free growth mechanism of GaAs nanowires by molecular beam epitaxy," *Phys. Rev. B*, vol. 77, p. 155326, Apr 2008.
- [60] A. Fontcuberta I Morral, C. Colombo, G. Abstreiter, J. Arbiol, and J. R. Morante, "Nucleation mechanism of gallium-assisted molecular beam epitaxy growth of gallium arsenide nanowires," *Applied Physics Letters*, vol. 92, pp. 063112–+, Feb. 2008.
- [61] S. Plissard, K. A. Dick, G. Larrieu, S. Godey, A. Addad, X. Wallart, and P. Caroff, "Gold-free growth of GaAs nanowires on silicon: arrays and polytypism," *Nanotechnology*, vol. 21, no. 38, p. 385602, 2010.
- [62] F. Jabeen, V. Grillo, S. Rubini, and F. Martelli, "Self-catalyzed growth of GaAs nanowires on cleaved Si by molecular beam epitaxy," *Nanotechnology*, vol. 19, no. 27, p. 275711, 2008.
- [63] J. H. Paek, T. Nishiwaki, M. Yamaguchi, and N. Sawaki, "Catalyst free MBE-VLS growth of GaAs nanowires on (111)Si substrate," *physica status solidi (c)*, vol. 6, no. 6, pp. 1436–1440, 2009.
- [64] A. M. Munshi, D. L. Dheeraj, V. T. Fauske, D.-C. Kim, A. T. J. van Helvoort, B.-O. Fimland, and H. Weman, "Vertically Aligned GaAs Nanowires on Graphite and Few-Layer Graphene: Generic Model and Epitaxial Growth," *Nano Letters*, vol. 12, no. 9, pp. 4570–4576, 2012.
- [65] G. Koblmüller, S. Hertenberger, K. Vizbaras, M. Bichler, F. Bao, J. Zhang, and G. Abstreiter, "Self-induced growth of vertical free-standing InAs nanowires on Si(111) by molecular beam epitaxy," *Nanotechnology*, vol. 21, pp. J5602+, Sept. 2010.

## BIBLIOGRAPHY

---

- [66] S. Hertenberger, D. Rudolph, M. Bichler, J. J. Finley, G. Abstreiter, and G. Koblmüller, “Growth kinetics in position-controlled and catalyst-free InAs nanowire arrays on Si(111) grown by selective area molecular beam epitaxy,” *Journal of Applied Physics*, vol. 108, pp. 114316–+, Dec. 2010.
- [67] E. Dimakis, J. Lähnemann, U. Jahn, S. Breuer, M. Hilse, L. Geelhaar, and H. Riechert, “Self-Assisted Nucleation and Vapor Solid Growth of InAs Nanowires on Bare Si(111),” *Crystal Growth & Design*, vol. 11, no. 9, pp. 4001–4008, 2011.
- [68] S. Hertenberger, D. Rudolph, S. Bolte, M. Döblinger, M. Bichler, D. Spirkoska, J. J. Finley, G. Abstreiter, and G. Koblmüller, “Absence of vapor-liquid-solid growth during molecular beam epitaxy of self-induced InAs nanowires on Si,” *Applied Physics Letters*, vol. 98, no. 12, p. 123114, 2011.
- [69] S. Hertenberger, D. Rudolph, J. Becker, M. Bichler, J. J. Finley, G. Abstreiter, and G. Koblmüller, “Rate-limiting mechanisms in high-temperature growth of catalyst-free InAs nanowires with large thermal stability,” *Nanotechnology*, vol. 23, no. 23, p. 235602, 2012.
- [70] B. Mandl, J. Stangl, E. Hilner, A. A. Zakharov, K. Hillerich, A. W. Dey, L. Samuelson, G. Bauer, K. Deppert, and A. Mikkelsen, “Growth Mechanism of Self-Catalyzed Group III/V Nanowires,” *Nano Letters*, vol. 10, no. 11, pp. 4443–4449, 2010.
- [71] B. Mandl, A. W. Dey, J. Stangl, M. Cantoro, L.-E. Wernersson, G. Bauer, L. Samuelson, K. Deppert, and C. Thelander, “Self-seeded, position-controlled InAs nanowire growth on Si: A growth parameter study,” *Journal of Crystal Growth*, vol. 334, no. 1, pp. 51 – 56, 2011.
- [72] K. Tomioka, K. Ikejiri, T. Tanaka, J. Motohisa, S. Hara, K. Hiruma, and T. Fukui, “Selective-area growth of III-V nanowires and their applications,” *Journal of Materials Research*, vol. 26, pp. 2127–2141, Sept. 2011.
- [73] A. V. Melechko, V. I. Merkulov, T. E. McKnight, M. A. Guillorn, K. L. Klein, D. H. Lowndes, and M. L. Simpson, “Vertically aligned carbon nanofibers and related structures: Controlled synthesis and directed assembly,” *Journal of Applied Physics*, vol. 97, no. 4, p. 041301, 2005.
- [74] Z. F. Ren, Z. P. Huang, J. W. Xu, J. H. Wang, P. Bush, M. P. Siegal, and P. N. Provencio, “Synthesis of Large Arrays of Well-Aligned Carbon Nanotubes on Glass,” *Science*, vol. 282, no. 5391, pp. 1105–1107, 1998.
- [75] Z. F. Ren, Z. P. Huang, D. Z. Wang, J. G. Wen, J. W. Xu, J. H. Wang, L. E. Calvet, J. Chen, J. F. Klemic, and M. A. Reed, “Growth of a single freestanding multiwall carbon nanotube on each nanonickel dot,” *Applied Physics Letters*, vol. 75, no. 8, pp. 1086–1088, 1999.

- [76] V. I. Merkulov, D. H. Lowndes, Y. Y. Wei, G. Eres, and E. Voelkl, "Patterned growth of individual and multiple vertically aligned carbon nanofibers," *Applied Physics Letters*, vol. 76, no. 24, pp. 3555–3557, 2000.
- [77] A. V. Melechko, R. Desikan, T. E. McKnight, K. L. Klein, and P. D. Rack, "Synthesis of vertically aligned carbon nanofibres for interfacing with live systems," *Journal of Physics D: Applied Physics*, vol. 42, no. 19, p. 193001, 2009.
- [78] "<http://www.ammrf.org.au/myscope/sem/practice/principles/layout.php>," 2012.
- [79] M. Lexholm, I. Karlsson, F. Boxberg, and D. Hessman, "Optical determination of Young's modulus of InAs nanowires," *Applied Physics Letters*, vol. 95, p. 113103, Sept. 2009.
- [80] S. O. Mariager, D. Khakhulin, H. T. Lemke, K. S. Kjær, L. Guerin, L. Nuccio, C. B. Sørensen, M. M. Nielsen, and R. Feidenhans'l, "Direct Observation of Acoustic Oscillations in InAs Nanowires," *Nano Letters*, vol. 10, no. 7, pp. 2461–2465, 2010.
- [81] R. M. Martin, "Relation between Elastic Tensors of Wurtzite and Zinc-Blende Structure Materials," *Phys. Rev. B*, vol. 6, pp. 4546–4553, Dec 1972.
- [82] A. Johnson, J. Lewis, M. Ra, K. Roberts, P. Walter, and B. Alberts, *Molecular Biology of The Cell*. Garland Science, 5th edition ed., 2008.
- [83] D. B. Williams and C. B. Carter, *Transmission Electron Microscopy*. Plenum Press, 1996.
- [84] K. A. Dick, J. Bolinsson, B. M. Borg, and J. Johansson, "Controlling the Abruptness of Axial Heterojunctions in III-V Nanowires: Beyond the Reservoir Effect," *Nano Letters*, vol. 12, no. 6, pp. 3200–3206, 2012.
- [85] P. Krogstrup, J. Yamasaki, C. B. Sørensen, E. Johnson, J. B. Wagner, R. Pennington, M. Aagesen, N. Tanaka, and J. Nygård, "Junctions in Axial III/V Heterostructure Nanowires Obtained via an Interchange of Group III Elements," *Nano Letters*, vol. 9, no. 11, pp. 3689–3693, 2009.
- [86] P. Hartel, H. Rose, and C. Dinges, "Conditions and reasons for incoherent imaging in STEM," *Ultramicroscopy*, vol. 63, no. 2, pp. 93 – 114, 1996.
- [87] K. Hiruma, H. Murakoshi, M. Yazawa, and T. Katsuyama, "Self-organized growth of GaAs/InAs heterostructure nanocylinders by organometallic vapor phase epitaxy," *Journal of Crystal Growth*, vol. 163, no. 3, pp. 226 – 231, 1996.
- [88] M. Paladugu, J. Zou, Y.-N. Guo, X. Zhang, Y. Kim, H. J. Joyce, Q. Gao, H. H. Tan, and C. Jagadish, "Nature of heterointerfaces in GaAs/InAs and InAs/GaAs axial nanowire heterostructures," *Applied Physics Letters*, vol. 93, no. 10, p. 101911, 2008.

## BIBLIOGRAPHY

---

- [89] L. E. Radford, “Equal rights for the reciprocal lattice,” *American Journal of Physics*, vol. 43, no. 8, pp. 697–700, 1975.
- [90] C. Kittel, *Introduction to Solid State Physics*. Wiley, 2004.
- [91] S. O. Mariager, C. B. Sørensen, M. Aagesen, J. Nygård, R. Feidenhans’l, and P. R. Willmott, “Facet structure of GaAs nanowires grown by molecular beam epitaxy,” *Applied Physics Letters*, vol. 91, no. 8, p. 083106, 2007.
- [92] “<http://jp-minerals.org/vesta/en/>,” 2012.
- [93] P. Caroff, J. Bolinsson, and J. Johansson, “Crystal Phases in III-V Nanowires: From Random Toward Engineered Polytypism,” *Selected Topics in Quantum Electronics, IEEE Journal of*, vol. 17, no. 4, pp. 829–846, 2011.
- [94] J. W. Edington, *Practical Electron Microscopy in Materials Science*, vol. 2. Macmillian, 1975.
- [95] J. Als-Nielsen and D. McMorrow, *Elements of Modern X-ray Physics*. John Wiley & Sons, Ltd, 2010.
- [96] F. Martelli, S. Rubini, F. Jabeen, L. Felisari, and V. Grillo, “On the growth of InAs nanowires by molecular beam epitaxy,” *Journal of Crystal Growth*, vol. 323, no. 1, pp. 297 – 300, 2011.
- [97] S. Heun, B. Radha, D. Ercolani, G. U. Kulkarni, F. Rossi, V. Grillo, G. Salvati, F. Beltram, and L. Sorba, “Pd-Assisted Growth of InAs Nanowires,” *Crystal Growth & Design*, vol. 10, no. 9, pp. 4197–4202, 2010.
- [98] H. Xu, Y. Wang, Y. Guo, Z. Liao, Q. Gao, H. H. Tan, C. Jagadish, and J. Zou, “Defect-Free  $\langle 110 \rangle$  Zinc-Blende Structured InAs Nanowires Catalyzed by Palladium,” *Nano Letters*, vol. 12, no. 11, pp. 5744–5749, 2012.
- [99] K. A. Dick, J. Bolinsson, M. E. Messing, S. Lehmann, J. Johansson, and P. Caroff, “Parameter space mapping of InAs nanowire crystal structure,” *Journal of Vacuum Science Technology B: Microelectronics and Nanometer Structures*, vol. 29, no. 4, p. 040000, 2011.
- [100] H. J. Joyce, J. Wong-Leung, Q. Gao, H. H. Tan, and C. Jagadish, “Phase Perfection in Zinc Blende and Wurtzite III-V Nanowires Using Basic Growth Parameters,” *Nano Letters*, vol. 10, no. 3, pp. 908–915, 2010.
- [101] P. Caroff, K. A. Dick, J. Johansson, M. E. Messing, K. Deppert, and L. Samuelson, “Controlled polytypic and twin-plane superlattices in III-V nanowires,” *Nature Nanotechnology*, vol. 4, pp. 50–55, Jan. 2009.

- [102] E. Uccelli, J. Arbiol, C. Magen, P. Krogstrup, E. Russo-Averchi, M. Heiss, G. Mugny, F. Morier-Genoud, J. Nygård, J. R. Morante, and A. Fontcuberta i Morral, “Three-Dimensional Multiple-Order Twinning of Self-Catalyzed GaAs Nanowires on Si Substrates,” *Nano Letters*, vol. 11, no. 9, pp. 3827–3832, 2011.
- [103] J. B. Babu and K. Yoh, “Effect of As/In-flux on the growth of InAs nanowire by molecular beam epitaxy,” *Journal of Crystal Growth*, vol. 323, no. 1, pp. 301 – 303, 2011.
- [104] J. Bubesh Babu and K. Yoh, “Growth rate enhancement of InAs nanowire by molecular beam epitaxy,” *Journal of Crystal Growth*, vol. 322, pp. 10–14, May 2011.
- [105] H. Shtrikman, R. Popovitz-Biro, A. Kretinin, L. Houben, M. Heiblum, M. Bukala, M. Galicka, R. Buczko, and P. Kacman, “Method for Suppression of Stacking Faults in Wurtzite III/V Nanowires,” *Nano Letters*, vol. 9, no. 4, pp. 1506–1510, 2009. PMID: 19253998.
- [106] T. Xu, K. A. Dick, S. Plissard, T. H. Nguyen, Y. Makoudi, M. Berthe, J.-P. Nys, X. Wallart, B. Grandidier, and P. Caroff, “Faceting, composition and crystal phase evolution in III/V antimonide nanowire heterostructures revealed by combining microscopy techniques,” *Nanotechnology*, vol. 23, no. 9, p. 095702, 2012.
- [107] N. V. Sibirev, M. Tchernycheva, M. A. Timofeeva, J.-C. Harmand, G. E. Cirlin, and V. G. Dubrovskii, “Influence of shadow effect on the growth and shape of InAs nanowires,” *Journal of Applied Physics*, vol. 111, no. 10, p. 104317, 2012.
- [108] M. T. Borgström, G. Immink, B. Ketelaars, R. Algra, and E. P. A. M. Bakkers, “Synergetic nanowire growth,” *Nature Nanotechnology*, vol. 2, pp. 541–544, Sept. 2007.
- [109] S. R. Plissard, D. R. Slapak, M. A. Verheijen, M. Hocevar, G. W. G. Immink, I. van Weperen, S. Nadj-Perge, S. M. Frolov, L. P. Kouwenhoven, and E. P. A. M. Bakkers, “From InSb Nanowires to Nanocubes: Looking for the Sweet Spot,” *Nano Letters*, vol. 12, no. 4, pp. 1794–1798, 2012.
- [110] C. Thelander, P. Caroff, S. Plissard, A. W. Dey, and K. A. Dick, “Effects of Crystal Phase Mixing on the Electrical Properties of InAs Nanowires,” *Nano Letters*, vol. 11, no. 6, pp. 2424–2429, 2011.
- [111] M. D. Schroer and J. R. Petta, “Correlating the Nanostructure and Electronic Properties of InAs Nanowires,” *Nano Letters*, vol. 10, no. 5, pp. 1618–1622, 2010.
- [112] L. Hofstetter, S. Csonka, J. Nygård, and C. Schönenberger, “Cooper pair splitter realized in a two-quantum-dot Y-junction,” *Nature*, vol. 461, pp. 960–963, Oct. 2009.
- [113] K. A. Dick, C. Thelander, L. Samuelson, and P. Caroff, “Crystal Phase Engineering in Single InAs Nanowires,” *Nano Letters*, vol. 10, no. 9, pp. 3494–3499, 2010.

## BIBLIOGRAPHY

---

- [114] P. Hiesinger, “Hall-Effect Levels in Ag- and Au-Doped p-Type GaAs,” *Phys. Stat. Sol. (a)*, vol. 33, pp. K39–K41, 1976.
- [115] S. Datta, *Electronic Transport in Mesoscopic Systems*. Cambridge University Press, 5th ed., 1995.
- [116] E. F. Schubert, *Doping in III-V Semiconductors*. AT&T, 1993.
- [117] E. F. Schubert and K. Ploog, “Shallow and deep donors in direct-gap  $n$ -type  $\text{Al}_x\text{Ga}_{1-x}\text{As} : \text{Si}$  grown by molecular-beam epitaxy,” *Phys. Rev. B*, vol. 30, pp. 7021–7029, Dec 1984.
- [118] R. K. Willardson and E. R. Weber, *Processing and Properties of Compound Semiconductors*, vol. 73. Academic Press, 2001.
- [119] S. Plissard, G. Larrieu, X. Wallart, and P. Caroff, “High yield of self-catalyzed GaAs nanowire arrays grown on silicon via gallium droplet positioning,” *Nanotechnology*, vol. 22, no. 27, p. 275602, 2011.
- [120] Y. J. Hong, W. H. Lee, Y. Wu, R. S. Ruoff, and T. Fukui, “van der Waals Epitaxy of InAs Nanowires Vertically Aligned on Single-Layer Graphene,” *Nano Letters*, vol. 12, no. 3, pp. 1431–1436, 2012.
- [121] K. Williams and R. Muller, “Etch rates for micromachining processing,” *Microelectromechanical Systems, Journal of*, vol. 5, no. 4, pp. 256–269, 1996.
- [122] S. Wright and H. Kroemer, “Reduction of oxides on silicon by heating in a gallium molecular beam at 800 °C,” *Applied Physics Letters*, vol. 36, pp. 210–+, Feb. 1980.
- [123] C. N. Cochran and L. M. Foster, “Vapor Pressure of Gallium, Stability of Gallium Suboxide Vapor, and Equilibria of Some Reactions Producing Gallium Suboxide Vapor,” *Journal of The Electrochemical Society*, vol. 109, no. 2, pp. 144–148, 1962.
- [124] M. de la Mata, C. Magen, J. Gazquez, M. I. B. Utama, M. Heiss, S. Lopatin, F. Furtmayr, C. J. Fernandez-Rojas, B. Peng, J. R. Morante, R. Rurali, M. Eickhoff, A. Fontcuberta i Morral, Q. Xiong, and J. Arbiol, “Polarity Assignment in ZnTe, GaAs, ZnO, and GaN-AlN Nanowires from Direct Dumbbell Analysis,” *Nano Letters*, vol. 12, no. 5, pp. 2579–2586, 2012.
- [125] D. Rudolph, S. Hertenberger, S. Bolte, W. Paosangthong, D. Spirkoska, M. Döblinger, M. Bichler, J. J. Finley, G. Abstreiter, and G. Koblmüller, “Direct Observation of a Noncatalytic Growth Regime for GaAs Nanowires,” *Nano Letters*, vol. 11, no. 9, pp. 3848–3854, 2011.
- [126] J. Johansson, J. Bolinsson, M. Ek, P. Caroff, and K. A. Dick, “Combinatorial Approaches to Understanding Polytypism in III-V Nanowires,” *ACS Nano*, vol. 6, no. 7, pp. 6142–6149, 2012.

- [127] R. V. Zucker, D. Chatain, U. Dahmen, S. Hagège, and W. Carter, “New software tools for the calculation and display of isolated and attached interfacial-energy minimizing particle shapes,” *Journal of Materials Science*, vol. 47, pp. 8290–8302, 2012.
- [128] I. V. Markov, *Crystal Growth for Beginners: Fundamentals of Nucleation, Crystal Growth, and Epitaxy*. World Scientific Publishing Company, 2 ed., 2003.
- [129] S. O. Mariager, S. L. Lauridsen, C. B. Sørensen, A. Dohn, P. R. Willmott, J. Nygård, and R. Feidenhans'l, “Stages in molecular beam epitaxy growth of GaAs nanowires studied by x-ray diffraction,” *Nanotechnology*, vol. 21, no. 11, p. 115603, 2010.
- [130] D. Kriegner, C. Panse, B. Mandl, K. A. Dick, M. Keplinger, J. M. Persson, P. Caroff, D. Ercolani, L. Sorba, F. Bechstedt, J. Stangl, and G. Bauer, “Unit Cell Structure of Crystal Polytypes in InAs and InSb Nanowires,” *Nano Letters*, vol. 11, no. 4, pp. 1483–1489, 2011.
- [131] A. Biermanns, S. Breuer, A. Trampert, A. Davydok, L. Geelhaar, and U. Pietsch, “Strain accommodation in Ga-assisted GaAs nanowires grown on silicon (111),” *Nanotechnology*, vol. 23, no. 30, p. 305703, 2012.
- [132] K. W. Schwarz and J. Tersoff, “From Droplets to Nanowires: Dynamics of Vapor-Liquid-Solid Growth,” *Phys. Rev. Lett.*, vol. 102, p. 206101, May 2009.
- [133] G. Patriarche, F. Glas, M. Tchernycheva, C. Sartel, L. Largeau, J.-C. Harmand, and G. E. Cirlin, “Wurtzite to Zinc Blende Phase Transition in GaAs Nanowires Induced by Epitaxial Burying,” *Nano Letters*, vol. 8, no. 6, pp. 1638–1643, 2008. PMID: 18471022.
- [134] D. L. Dheeraj, G. Patriarche, H. Zhou, T. B. Hoang, A. F. Moses, S. Grønsberg, A. T. J. van Helvoort, B.-O. Fimland, and H. Weman, “Growth and Characterization of Wurtzite GaAs Nanowires with Defect-Free Zinc Blende GaAsSb Inserts,” *Nano Letters*, vol. 8, no. 12, pp. 4459–4463, 2008.
- [135] P. Caroff, “Private communication,” 2012.
- [136] X. Duan, R. Gao, P. Xie, T. Cohen-Karni, Q. Qing, H. S. Choe, B. Tian, X. Jiang, and C. M. Lieber, “Intracellular recordings of action potentials by an extracellular nanoscale field-effect transistor,” *Nature Nanotechnology*, vol. 7, pp. 174–179, Mar. 2012.
- [137] R. Yan, J.-H. Park, Y. Choi, C.-J. Heo, S.-M. Yang, L. P. Lee, and P. Yang, “Nanowire-based single-cell endoscopy,” *Nature Nanotechnology*, vol. 7, pp. 191–196, Mar. 2012.
- [138] F. J. Rawson, C. L. Yeung, S. K. Jackson, and P. M. Mendes, “Tailoring 3D Single-Walled Carbon Nanotubes Anchored to Indium Tin Oxide for Natural Cellular Uptake and Intracellular Sensing,” *Nano Letters*, vol. 0, no. 0, p. null, 2012.

## BIBLIOGRAPHY

---

- [139] J. J. VanDersarl, A. M. Xu, and N. A. Melosh, “Nanostraws for Direct Fluidic Intracellular Access,” *Nano Letters*, vol. 12, no. 8, pp. 3881–3886, 2012.
- [140] W. Hällström, T. Mårtensson, C. Prinz, P. Gustavsson, L. Montelius, L. Samuelson, and M. Kanje, “Gallium Phosphide Nanowires as a Substrate for Cultured Neurons,” *Nano Letters*, vol. 7, no. 10, pp. 2960–2965, 2007.
- [141] T. Nagai, K. Ibata, E. S. Park, M. Kubota, K. Mikoshiba, and A. Miyawaki, “A variant of yellow fluorescent protein with fast and efficient maturation for cell-biological applications,” *Nature Biotechnology*, vol. 20, pp. 87–90, 2002.
- [142] N. Friedman, L. Cai, and X. S. Xie, “Linking Stochastic Dynamics to Population Distribution: An Analytical Framework of Gene Expression,” *Phys. Rev. Lett.*, vol. 97, p. 168302, Oct 2006.
- [143] S. Roddaro, P. Caroff, G. Biasiol, F. Rossi, C. Bocchi, K. Nilsson, L. Frøberg, J. B. Wagner, L. Samuelson, L.-E. Wernersson, and L. Sorba, “Growth of vertical InAs nanowires on heterostructured substrates,” *Nanotechnology*, vol. 20, no. 28, p. 285303, 2009.
- [144] M. A. Guillorn, T. E. McKnight, A. Melechko, V. I. Merkulov, P. F. Britt, D. W. Austin, D. H. Lowndes, and M. L. Simpson, “Individually addressable vertically aligned carbon nanofiber-based electrochemical probes,” *Journal of Applied Physics*, vol. 91, no. 6, pp. 3824–3828, 2002.
- [145] S. G. Ghalamestani, S. Johansson, B. M. Borg, E. Lind, K. A. Dick, and L.-E. Wernersson, “Uniform and position-controlled InAs nanowires on  $2 \times 2$  Si substrates for transistor applications,” *Nanotechnology*, vol. 23, no. 1, p. 015302, 2012.
- [146] M. Yu, S. Stott, M. Toner, S. Maheswaran, and D. A. Haber, “Circulating tumor cells: approaches to isolation and characterization,” *The Journal of Cell Biology*, vol. 192, no. 3, pp. 373–382, 2011.
- [147] “<http://www.veridex.com/cellsearch/CellSearchHCP.aspx>,” 2012.
- [148] S. Nagrath, L. V. Sequist, S. Maheswaran, D. W. Bell, D. Irimia, L. Ulkus, M. R. Smith, E. L. Kwak, S. Digumarthy, A. Muzikansky, P. Ryan, U. J. Balis, R. G. Tompkins, D. A. Haber, and M. Toner, “Isolation of rare circulating tumour cells in cancer patients by microchip technology,” *Nature*, vol. 450, pp. 1235–1239, Dec. 2007.
- [149] H. Mohamed, M. Murray, J. N. Turner, and M. Caggana, “Isolation of tumor cells using size and deformation,” *Journal of Chromatography A*, vol. 1216, no. 47, pp. 8289 – 8295, 2009. 23rd International Symposium on Microscale Bioseparations.

- [150] S. L. Stott, R. J. Lee, S. Nagrath, M. Yu, D. T. Miyamoto, L. Ulkus, E. J. Inerra, M. Ulman, S. Springer, Z. Nakamura, A. L. Moore, D. I. Tsukrov, M. E. Kempner, D. M. Dahl, C.-L. Wu, A. J. Iafrate, M. R. Smith, R. G. Tompkins, L. V. Sequist, M. Toner, D. A. Haber, and S. Maheswaran, "Isolation and Characterization of Circulating Tumor Cells from Patients with Localized and Metastatic Prostate Cancer," *Science Translational Medicine*, vol. 2, no. 25, p. 25ra23, 2010.
- [151] S. L. Stott, C.-H. Hsu, D. I. Tsukrov, M. Yu, D. T. Miyamoto, B. A. Waltman, S. M. Rothenberg, A. M. Shah, M. E. Smas, G. K. Korir, F. P. Floyd, A. J. Gilman, J. B. Lord, D. Winokur, S. Springer, D. Irimia, S. Nagrath, L. V. Sequist, R. J. Lee, K. J. Isselbacher, S. Maheswaran, D. A. Haber, and M. Toner, "Isolation of circulating tumor cells using a microvortex-generating herringbone-chip," *Proceedings of the National Academy of Science*, vol. 107, pp. 18392–18397, Oct. 2010.
- [152] S. Tan, L. Yobas, G. Lee, C. Ong, and C. Lim, "Microdevice for the isolation and enumeration of cancer cells from blood," *Biomedical Microdevices*, vol. 11, pp. 883–892, 2009. 10.1007/s10544-009-9305-9.
- [153] G. Velve-Casquillas, M. L. Berre, M. Piel, and P. T. Tran, "Microfluidic tools for cell biological research," *Nano Today*, vol. 5, no. 1, pp. 28 – 47, 2010.
- [154] G. M. Whitesides, "The origins and the future of microfluidics," *Nature*, vol. 442, pp. 368–373, July 2006.
- [155] S. Nadkarni, *Protocols for fabrication of microfluidic devices*. Cornell University, June 2004.
- [156] A. D. Stroock, S. K. W. Dertinger, A. Ajdari, I. Mezić, H. A. Stone, and G. M. Whitesides, "Chaotic Mixer for Microchannels," *Science*, vol. 295, pp. 647–651, Jan. 2002.
- [157] M. A. Eddings, M. A. Johnson, and B. K. Gale, "NOTE: Determining the optimal PDMS-PDMS bonding technique for microfluidic devices," *Journal of Micromechanics and Microengineering*, vol. 18, p. 067001, June 2008.

